

THE STUDY OF INTERDIFFUSION AND DEFECT MECHANISMS IN
 $\text{Si}_{1-x}\text{Ge}_x$ SINGLE QUANTUM WELL AND SUPERLATTICE MATERIALS

By

MICHELLE DENISE GRIGLIONE

A DISSERTATION PRESENTED TO THE GRADUATE SCHOOL
OF THE UNIVERSITY OF FLORIDA IN PARTIAL FULFILLMENT
OF THE REQUIREMENTS FOR THE DEGREE OF
DOCTOR OF PHILOSOPHY

UNIVERSITY OF FLORIDA

1999

Copyright 1999

by

Michelle Denise Griglione

For Rob, Dad and Mom

ACKNOWLEDGMENTS

The completion of this research work and my graduate career would not have been possible without help from many people. The contributions of my committee members Dr. Cammy Abernathy and Dr. Rich Dickinson are greatly appreciated. I am indebted to Dr. Mark Law for his patience as I either waltzed into or paced outside of his open door with my latest triumphs or traumas. Dr. Kevin Jones has allowed generous access to his labs, TEM equipment and post-docs. I am most indebted to Dr. Tim Anderson, my project advisor, for his scientific guidance as well as personal support for my unorthodox graduate career.

Dr. Yaser Haddara receives my greatest appreciation for the knowledge that he imparted to me regarding solid state diffusion and process simulation. Our weekly discussions were invaluable. I am also grateful to Dr. Wish Krishnamoorthy for TEM analysis and for sharing his wisdom regarding HRXRD and basic physical science. I owe unending gratitude to Erik Kuryliw for his persistent partnership in discovering the surprising versatility of the rapid thermal processor.

I thank Pete Axson for generously lending his technical expertise in such tricky areas as welding gas lines and his patient troubleshooting. Many thanks to Courtney Hazelton, Steve Schein and the rest of the cleanroom

crew for their friendly service with a smile, as well as Dennis Vince in the ChemE shop. I am grateful to Dr. Margarida Puga-Lambers for her dedicated and timely SIMS characterization. Doug Meyers of ASM Epitaxy, Alex Van de Bogaard of Delft University, and Bruce Gnade of Texas Instruments are credited with growth of the materials used in this study. Dr. Olga Kryliok is appreciated for her support and interest. Lance Robertson of SWAMP Center has contributed to the overall morale of this research project.

Acknowledgment is also due to my secondary school science teachers, Ms. Betty Johnson and Dr. John Lieberman, who made my first brushes with science fun and fascinating. My parents taught me the value of knowledge, personal achievement and striving to make a contribution. They have supported me wholeheartedly throughout this endeavor, as they have through every other, and I thank them. Last, but certainly not least, I thank Rob Baker for his help with the manuscript, and more significantly, the personal encouragement and understanding that he provided on a daily basis ... especially on the days when more than the usual amount of understanding and encouragement was needed.

TABLE OF CONTENTS

	page
ACKNOWLEDGMENTS.....	iv
LIST OF TABLES.....	ix
LIST OF FIGURES.....	xi
ABSTRACT.....	xv
1 INTRODUCTION.....	1
1.1 Selected Material Properties and Device Applications	3
1.1.1 Material Properties.....	3
1.1.2 Device Applications.....	8
1.2 Strain and Strain Relaxation in SiGe Heterostructures.....	11
1.3 Diffusion in Elemental Semiconductors	15
1.3.1 Continuum Theory	16
1.3.2 Point Defects and Diffusion Mechanisms.....	18
1.4 Non-equilibrium Point Defect Injection.....	24
1.4.1 Interstitial Injection (Oxide Growth).....	25
1.4.2 Vacancy Injection (Nitride Growth)	27
1.5 Literature Review	28
1.5.1 Self-Diffusion and Intrinsic Interdiffusion	28
1.5.1.1 Self-diffusion.....	28
1.5.1.2 Tracer studies of Ge in Si.....	29
1.5.1.3 Diffusion studies of Si _{1-x} Ge _x /Si heterostructures	30
1.5.2 Oxidation and Nitridation Enhanced Diffusion	32
2 SAMPLE PREPARATION AND CHARACTERIZATION.....	34
2.1 Growth Parameters and Structure.....	34
2.2 Transmission Electron Microscopy.....	37
2.2.1 Overview	37
2.2.2 TEM Sample Preparation	40
2.2.2.1 Plan view	40
2.2.2.2 Cross-sectional	41
2.2.3 Images of Structures	42
2.2.3.1 XTEM	42
2.2.3.2 PTEM.....	44

2.3 Secondary Ion Mass Spectroscopy.....	45
2.3.1 Determination of the Ge Depth Profile in SiGe Structures.....	50
2.3.2 Determination of the Error in D.....	54
2.4 X-ray Diffraction.....	56
2.4.1 Overview.....	56
2.4.2 Optimization Procedures.....	61
2.4.3 Determination of Interdiffusivity of Superlattice Layers.....	62
2.4.4 Determination of Strain Relaxation.....	64
3 BEHAVIOR OF ANNEALED $\text{Si}_{1-x}\text{Ge}_x$ SINGLE QUANTUM WELLS.....	67
3.1 Growth Parameters and Structure.....	68
3.2 Processing.....	69
3.2.1 Rapid Thermal Processing.....	69
3.2.2 Furnace Processing.....	72
3.3 Simulation of Diffusion.....	73
3.4 Results.....	79
3.4.1 Diffusivities and Activation Energies from SIMS/FLOOPS.....	79
3.4.2 Diffusion Behavior of Partially Relaxed Structures.....	84
3.4.3 $\text{Si}_{1-x}\text{Ge}_x$ Single Quantum Well with Boron Marker Layer.....	85
3.4.4 Estimation of Fractional Interstitial Components of Diffusion.....	89
3.4.5 TEM.....	95
3.5 Discussion.....	98
3.5.1 Diffusivities of Fully-Strained Structures.....	98
3.5.2 Diffusivities of Partially-relaxed Structures.....	114
3.5.3 Misfit Dislocation Effects.....	116
3.5.4 Fractional Interstitial Components from Marker Layer Experiments.....	121
3.6 Conclusions.....	123
4 BEHAVIOR OF ANNEALED ASYMMETRICALLY STRAINED $\text{Si}/\text{Si}_{1-x}\text{Ge}_x$ SUPERLATTICES WITH $\text{Si}_{1-x}\text{Ge}_x$ BUFFER.....	126
4.1 Growth Parameters and Structure.....	127
4.2 Strain State.....	129
4.3 Processing.....	131
4.4 Simulation of Diffusion.....	132
4.5 Results.....	132
4.5.1 SIMS/FLOOPS.....	132
4.5.2 High Resolution Xray Diffraction.....	135
4.5.2.1 Diffusivities.....	135
4.5.2.2 Strain relaxation.....	139
4.5.3 TEM.....	141
4.6 Discussion.....	147
4.6.1 Diffusivities Determined from SIMS and FLOOPS.....	147

4.6.2 Diffusivities Determined from HRXRD.....	156
4.6.3 Strain Relaxation Determined from HRXRD.....	159
4.7 Conclusions.....	161
5 BEHAVIOR OF ANNEALED ASYMMETRICALLY STRAINED Si/Si _{1-x} Ge _x SUPERLATTICES WITH Si BUFFER.....	164
5.1 Growth Parameters and Structure.....	165
5.2 Strain State.....	166
5.3 Processing.....	168
5.4 Simulation of Diffusion.....	168
5.5 Results.....	169
5.5.1 SIMS/FLOOPS.....	169
5.5.2 High Resolution Xray Diffraction.....	171
5.5.2.1 Diffusivities.....	172
5.5.2.2 Strain relaxation.....	175
5.5.3 TEM.....	176
5.6 Discussion.....	179
5.6.1 Diffusivities Determined from SIMS and FLOOPS.....	179
5.6.2 Diffusivities Determined from HRXRD.....	187
5.6.3 Strain Relaxation from HRXRD.....	189
5.6.4 Effect of Strain State on Diffusivity Values.....	191
5.7 Conclusions.....	194
6 CONCLUSIONS AND FUTURE WORK.....	197
6.1 Conclusions.....	197
6.1.1 Single Quantum Well Structures.....	197
6.1.2 Superlattice Structures.....	199
6.1.3 Strain Effects.....	201
6.2 Contributions.....	201
6.2.1 Modeling.....	201
6.2.2 Experimental.....	202
6.3 Future Work.....	203
6.3.1 Single Quantum Well Investigations.....	203
6.3.2 Superlattice Investigations.....	204
6.3.3 Simulations and Modeling.....	205
APPENDIX A EXAMPLES OF FLOOPS PROGRAMS.....	206
APPENDIX B GLOSSARY.....	211
REFERENCES.....	215
BIOGRAPHICAL SKETCH.....	222

LIST OF TABLES

<u>Table</u>	<u>page</u>
1-1. Advantages and disadvantages of SiGe used in device applications.	8
3-1. Extracted diffusivity and enhancement values for SQW/MBE.	82
3-2. Extracted diffusivity and enhancement values for SQW/VPE.	82
3-3. Extracted diffusivities for initially partially relaxed SQW/MBE.	85
3-4. Anneal times needed in FLOOPS to achieve actual B diffusion profiles.	88
3-5. Fractional interstitial components and modified diffusivities and point defect supersaturations determined for diffusion in inert ambient.	93
3-6. Fractional interstitial components and modified diffusivities and point defect supersaturations determined for diffusion in oxidizing ambient.	94
3-7. Comparison of diffusivities of SQW/MBE and SQW/VPE in inert and oxidizing ambients.	107
4-1. Extracted diffusivity and enhancement values for SL/SiGe.	133
4-2. Extracted diffusivities for SL/SiGe using HRXRD.	136
4-3. Parallel and perpendicular lattice constants of SL/SiGe.	142
4-4. Comparison of parameters of interdiffusion of SQW/MBE and SL/SiGe.	155
4-5. Diffusivities of SL/SiGe extracted from FLOOPS and HRXRD.	159
5-1. Extracted diffusivity and enhancement values for SL/Si.	169
5-2. Extracted diffusivity values for SL/Si using HRXRD.	174
5-3. Parallel and perpendicular lattice constants of SL/Si.	177

5-4. Diffusivities of SL/Si extracted from FLOOPS and HRXRD.....	189
5-5. Comparison of diffusivities of SL/SiGe and SL/Si in inert, oxidizing and nitriding ambients.....	193
5-6. Comparison of activation energies of SL/SiGe and SL/Si in inert, oxidizing and nitriding ambients.....	194

LIST OF FIGURES

<u>Figure</u>	<u>page</u>
1-1. Phase diagram of the Si-Ge system [Kas95].....	4
1-2. The diamond cubic structure of $\text{Si}_{1-x}\text{Ge}_x$ alloy [Kas95].....	4
1-3. Lattice constant of $\text{Si}_{1-x}\text{Ge}_x$ versus Ge composition.	5
1-4. Critical thickness versus germanium fraction for $\text{Si}_{1-x}\text{Ge}_x$ films on a Si substrate.....	6
1-5. Energy gap versus germanium fraction for unstrained and coherently strained $\text{Si}_{1-x}\text{Ge}_x$ [Peo86].	7
1-6. Cross-section of a $\text{Si}_{1-x}\text{Ge}_x$ HBT [Tem88].....	9
1-7. Possible waveguide-photodetector structure using $\text{Si}_{1-x}\text{Ge}_x$ alloy [Pre95].....	10
1-8. Evolution of a misfit dislocation at the Si and Ge interface.....	13
1-9. Termination of a misfit dislocation.....	14
1-10. The direct interstitial mechanism.....	19
1-11. The vacancy mechanism.....	20
1-12. The Frank-Turnbull (dissociative) mechanism.....	21
1-13. The kick-out mechanism.....	22
2-1. $\text{Si}_{1-x}\text{Ge}_x$ sample structures used in these investigations.....	35
2-2. Sample structure SQW/MBE, a single quantum well grown by MBE.....	36
2-3. Schematic of ray paths originating from the object which create a TEM image [Wil96].....	38
2-4. Schematic of TEM views.....	39

2-5. Front and rear views of the XTEM assembly after preparation [Wil96].....	41
2-6. Cross sectional view TEM (XTEM) micrographs of as-grown (a) structure SL/SiGe and (b) structure SL/Si.	46
2-7. XTEM micrographs of as-grown (a) structure SQW/MBE and (b) structure SQW/VPE	47
2-8. Plan view TEM micrographs of as-grown (a) structure SL/SiGe and (b) structure SL/Si.2-9.....	48
2-9. Figure 2-9. Plan view TEM micrographs of as-grown (a) structure SQW/MBE and (b) structure SQW/VPE.....	49
2-10. Ge concentration profile determined from SIMS for sample structure SL/SiGe.....	52
2-11. Ge concentration profile determined from SIMS for sample structure SL/Si.....	52
2-12. Ge concentration profile determined from SIMS for sample structure SQW/VPE.....	53
2-13. Ge concentration profile determined from SIMS for sample structure SQW/MBE.....	53
2-14. SIMS profile of structure SQW/MBE.....	54
2-15. Schematic of symmetric x-ray Bragg reflection [Cul78].....	56
2-16. Schematic of the monochromator/collimator.....	57
2-17. Schematic of the x-ray path used in triple axis mode.....	59
2-18. X-ray rocking curve of structure SL/SiGe before anneal.....	60
2-19. X-ray rocking curve of structure SL/Si before anneal.....	60
2-20. Miscut of substrate and mistilt of epilayer.....	62
2-21. Example of positive and negative x-ray diffraction from an asymmetric plane.....	66
3-1. Schematic of sample structures SQW/MBE and SQW/VPE.....	69
3-2. Effective Ge diffusivity of structure SQW/MBE as a function of annealing temperature in inert, oxidizing, and nitriding ambients.....	81

3-3. Effective Ge diffusivity of structure SQW/VPE as a function of annealing temperature in inert, oxidizing, and nitriding ambients.....	83
3-4. Schematic of test structure SQW/B.....	86
3-5. Diffusion of as-grown B marker layer in all ambients.....	88
3-6. Cross sectional view TEM micrographs of structure SQW/MBE after annealing in inert ambient at (a) 1000 °C for 43 min and (b) 1200 °C for 1 min.....	99
3-7. Plan view TEM micrographs of structure SQW/MBE after annealing in inert ambient at (a) 900 °C for 330 min and (b) 1200 °C for 1 min.....	100
3-8. Plan view TEM micrographs of structure SQW/VPE after annealing at (a) 900 °C for 330 min in oxidizing ambient and (b) 1200 °C for 1 min in inert ambient.....	101
3-9. Comparison of experimentally determined SIMS profile and FLOOPS profile.....	103
3-10. Illustration of non-Gaussian shape of SQW diffused profiles.....	104
3-11. Comparison of diffusivities of structures SQW/MBE and SQW/VPE in (a) inert ambient and (b) oxidizing ambient.....	106
3-12. Diffusivities of Ge in Si/Si _{1-x} Ge _x /Si SQWs from previous studies and this work.....	108
3-13. Plot of diffusivities of all anneal times in inert ambient for each temperature for SQW/MBE.....	111
3-14. Comparison of Ge SIMS profiles in inert, oxidizing and nitriding ambients for SQW/MBE.....	112
3-15. Comparison of Ge diffusivities of partially relaxed structures in inert ambient.....	115
4-1. Schematic of sample structure SL/SiGe.....	128
4-2. Effective Ge diffusivity of structure SL/SiGe as a function of annealing temperature in inert, oxidizing, and nitriding ambients.....	134
4-3. X-ray diffractometer scans of the SL/SiGe superlattice peaks about Si(004) with increasing anneal times in inert ambient.....	137

4-4. Decay of the integrated intensity of the first order superlattice peak about Si(004) as a function of annealing time, temperature and ambient of SL/SiGe.....	138
4-5. Cross sectional view TEM micrograph of structure SL/SiGe after annealing in oxidizing ambient at 850 °C for 8 min.....	145
4-6. Plan view TEM micrographs of structure SL/SiGe after annealing in inert ambient at (a) 850 °C for 8 min and (b) 1000 °C for 2 min.....	146
4-7. Comparison of experimentally determined SIMS profile and FLOOPS profile using the Fermi model for samples annealed at 950 °C and 3 min in (a) inert (b) oxidizing and (c) nitriding ambient.....	148
4-8. Diffusivities of Ge in $\text{Si}_{1-x}\text{Ge}_x/\text{Si}$ SLs with a $\text{Si}_{1-x}\text{Ge}_x$ buffer layer from (+) Holländer <i>et al.</i> and (•) this work.....	150
4-9. Comparison of Ge SIMS profiles in inert, oxidizing, and nitriding ambients for SL/SiGe.	154
5-1. Schematic of sample structure SL/Si.....	166
5-2. Effective Ge diffusivity of structure SL/Si as a function of annealing temperature in inert, oxidizing, and nitriding ambient.....	170
5-3. X-ray diffractometer scans of the SL/SiGe superlattice peaks about Si(004) with increasing anneal times in inert ambient.....	173
5-4. Decay of the integrated intensity of the first order superlattice peak about Si(004) as a function of annealing time, temperature and ambient of SL/Si.....	174
5-5. Plan view TEM micrograph of structure SL/Si after annealing in inert ambient at 850 °C for 8 min.....	178
5-6. Comparison of experimentally determined SIMS profile and FLOOPS profile for 950 °C and 3 min in (a) inert (b) oxidizing and (c) nitriding ambient.....	180
5-7. Diffusivities of Ge in $\text{Si}_{1-x}\text{Ge}_x/\text{Si}$ SLs with a Si(100) buffer layer from previous studies and this work.	184
5-8. Comparison of Ge SIMS profiles in inert, oxidizing and nitriding ambients for SL/Si.	185

Abstract of Dissertation Presented to the Graduate School
of the University of Florida in Partial Fulfillment of the
Requirements for the Degree of Doctor of Philosophy

THE STUDY OF INTERDIFFUSION AND DEFECT MECHANISMS IN
 $\text{Si}_{1-x}\text{Ge}_x$ SINGLE QUANTUM WELL AND SUPERLATTICE MATERIALS

By

Michelle Denise Griglione

May 1999

Chairman: Dr. Tim Anderson
Major Department: Chemical Engineering

Dimensions of Si microelectronic devices continue to shrink in pursuit of higher speed operation. Soon, these dimensions will reach a minimum and an alternative material must be found. The alloy Si-Ge has been suggested as a replacement due to its ability to be band-gap engineered, as well as its compatibility with current Si-only processing, low cost, and environmental friendliness. The fabrication of Si-Ge devices includes several high temperature processing steps which can degrade device performance if interdiffusion occurs within the material. This dissertation investigated the interdiffusion of Si-Ge structures as a function of processing temperature (850 to 1200 °C), layer structure, and anneal time. In particular, the roles of vacancy and interstitial point defects in the diffusion process were

investigated and a model presented which simulated diffusion under a variety of material and processing conditions.

Activation energies of diffusion in inert, oxidizing, and nitriding ambients for single quantum well (SQW) material were found to be 5.8, 5.0, and 3.0 eV, respectively. Diffusion in inert and oxidizing ambients was similar, while significant retardation of diffusion was seen in nitriding ambient.

Activation energies of diffusion in inert, oxidizing and nitriding ambients for a superlattice (SL) with a $\text{Si}_{1-x}\text{Ge}_x$ buffer layer were found to be 3.1, 2.4, and 4.0 eV, respectively. Activation energies of diffusion in inert, oxidizing, and nitriding ambients for a SL with a Si buffer layer were found to be 3.63, 2.81, and 4.1 eV, respectively. Slight enhancement of diffusion was observed in oxidizing ambient at lower temperatures, while retardation of diffusion was observed in nitriding ambient at all temperatures. No difference in diffusion behavior was observed between the two SL structures.

Transmission electron microscopy confirmed that dislocations were present and grew with increased anneal time and were believed to have a significant effect on diffusivity values. Experiments using SQWs with buried boron marker layers determined that a portion of interstitials injected in an oxidizing ambient were captured by dislocations, however, enough remained available to aid in the diffusion process.

CHAPTER 1 INTRODUCTION

Recently there has been increased interest in alloys of silicon and germanium ($\text{Si}_{1-x}\text{Ge}_x$) for applications in electronics and photonics. Devices incorporating Si-Ge solid solutions show increased speeds as well as other desirable features over the equivalent pure Si devices. The manufacture of these devices includes several high-temperature and oxidation steps, and it is necessary that $\text{Si}_{1-x}\text{Ge}_x$ heterostructures be able to withstand these processing steps without device degradation such as interface broadening and intermixing of the device layer structure. Therefore, it is important to understand the diffusion processes that cause degradation.

Common $\text{Si}_{1-x}\text{Ge}_x$ device designs include single quantum well (SQW), monolayer superlattice, and multiple quantum well (MQW) structures. The single quantum well material normally consists of a buffer layer grown on a Si substrate, followed by a $\text{Si}_{1-x}\text{Ge}_x$ layer and a Si cap layer, $\text{Si}/\text{Si}_{1-x}\text{Ge}_x/\text{Si}$. In the monolayer superlattice material, m atomic layers of pure Si are deposited followed by n atomic layers of pure Ge (m and n are usually <10), with this pattern repeated p times, $(\text{Si}_m\text{Ge}_n)_p$. For the MQW material a layer of pure Si is grown, followed by a layer of $\text{Si}_{1-x}\text{Ge}_x$ alloy of particular composition, x , with this pattern repeated for a determined number of periods, p , $(\text{Si}/\text{Si}_{1-x}\text{Ge}_x)_p$. Each structure has diffusion characteristics which are influenced by such

parameters as anneal time and temperature, alloy composition, strain state, as well as quantum well (layer) thickness and periodicity.

A review of the literature reveals that work done thus far in thermally activated interdiffusion of Si-Ge material can be divided into two categories: (1) interdiffusion of SQW and SL materials in an inert environment [Van90, Sun94, Hol92, Zau94] and (2) impurity diffusion in inert and reactive environments [Kuo95, Pai95, Fan96, Kuz98]. There has been discussion about identification of which atoms (Si, Ge, or both) are diffusing in the undoped case as well as the fractional contribution of interstitials and vacancies towards diffusion in both cases. A detailed model for either, however, has not been proposed.

This work has investigated intrinsic interdiffusion of undoped SQW and SL material in inert, oxidizing, and nitriding environments over the temperature range 800 to 1200 °C. Experiments were conducted to measure the extent of interface intermixing and the corresponding diffusion coefficient. The effects of surface oxidation and nitridation have been examined to determine the extent of diffusion enhancement or retardation as a result of processing under point defect supersaturation conditions. Estimates of the fractional contributions of interstitials and vacancies to Si/Si_{1-x}Ge_x diffusion have been ascertained. Finally, the effect of dislocations on the concentration of injected point defects available to aid in interdiffusion has been studied.

1.1 Selected Material Properties and Device Applications

1.1.1 Material Properties

In microelectronics, interest in a semiconductor material evolves if the material has basic properties suitable for device applications. Device fabrication and operation requirements then dictate what specific material properties need to be investigated and adapted further. It is therefore important to introduce the device applications and material properties of $\text{Si}_{1-x}\text{Ge}_x$ that make it an increasingly appealing material in the semiconductor industry. The crystal structure, lattice constant, critical thickness, phase diagram, and band gap of $\text{Si}_{1-x}\text{Ge}_x$ are all properties that determine performance in several different device applications. These material properties are also of particular importance in this investigation because they either have a primary or secondary effect on interface diffusion, and they must be known to effectively analyze the data obtained from the characterization methods described in Chapter 2.

The Si-Ge system exhibits an isomorphous phase diagram with nearly ideal-solution behavior in both the liquid and solid solutions [Kas95]. The solid and liquid phases are separated by a region of coexistence, which gives rise to segregation upon crystallization from the melt (Figure 1-1).

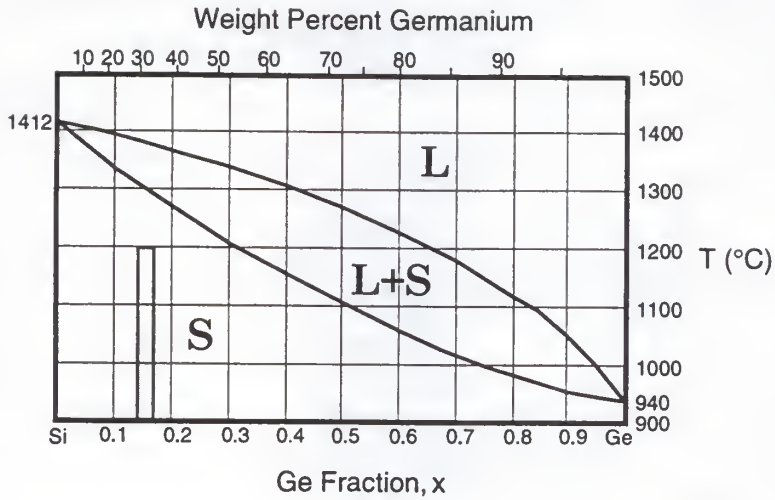


Figure 1-1. Phase diagram of the Si-Ge system [Kas95]. The gray section indicates the area of composition and temperature studied in this thesis.

The alloy silicon-germanium, $\text{Si}_{1-x}\text{Ge}_x$, is a semiconductor which crystallizes in a diamond cubic-type substitutional structure. This structure can be considered as two face-centered cubic sublattices shifted by one quarter of the body-diagonal, $R=1/4\langle 111 \rangle$, as shown in Figure 1-2.

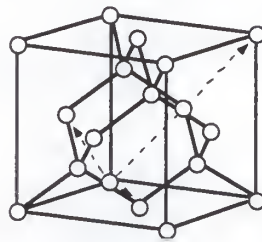


Figure 1-2. The diamond cubic structure of $\text{Si}_{1-x}\text{Ge}_x$ alloy [Kas95].

The lattice parameter, a , is a function of Ge composition, x , and has been found to follow [Kas95]:

$$a(x) = 0.002733x^2 + 0.01992x + 0.5431(\text{nm}) \quad (1-1)$$

showing a slight deviation from Vegard's rule, which predicts the lattice constant of the alloy based on linearity between the endpoint lattice parameters of pure Si and Ge:

$$a(x) = (a_{\text{Ge}} - a_{\text{Si}})x + a_{\text{Si}} = 0.0227x + 0.5431 \text{ (nm)} \quad (\text{Vegard's Rule}) \quad (1-2)$$

Figure 1-3 shows the composition dependence of the lattice constant predicted using Vegard's rule, as well as the curve predicted by Equation 1-1.

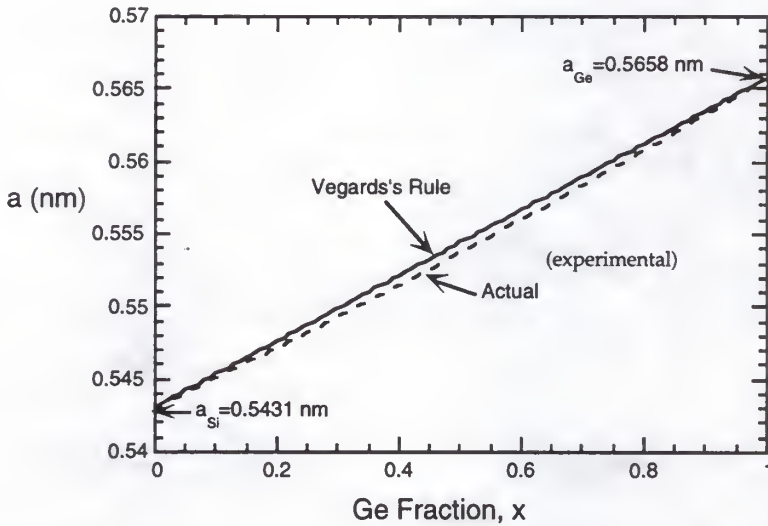


Figure 1-3. Lattice constant of $\text{Si}_{1-x}\text{Ge}_x$ versus Ge composition. Curves predicted by Vegard's rule and experimental [Kas95].

For epitaxially grown, pseudomorphic (the lattice planes of the epilayer and substrate are in perfect registry) $\text{Si}_{1-x}\text{Ge}_x$ films, there is built-in strain which is fixed by the lattice constant of the substrate on which the film is

grown. The lattice mismatch between Si and Ge is $\approx 4.2\%$ with Ge having the larger lattice parameter. Strain energy plays a critical role in band alignment and energy gap values. The critical thickness for pseudomorphic growth decreases rapidly with increasing Ge content. For example, a capped layer with Ge composition of $x=0.1$ has a critical thickness of $\sim 650 \text{ \AA}$, while at Ge composition $x=0.5$ the critical layer thickness reduces to $\sim 30 \text{ \AA}$ (Figure 1-4).

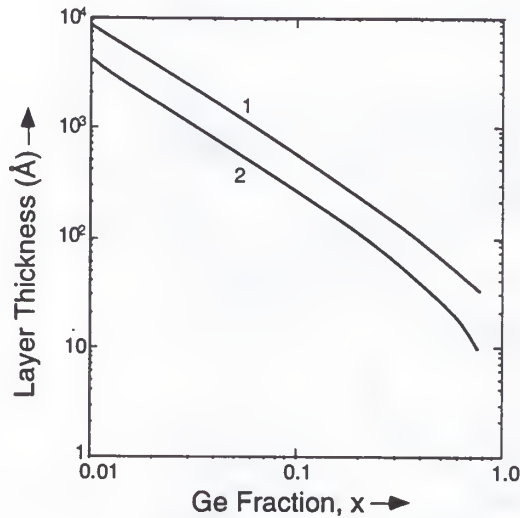


Figure 1-4. Critical thickness versus germanium fraction for $\text{Si}_{1-x}\text{Ge}_x$ films on a Si substrate. Curve 1 is for Si-capped material, while curve 2 is for uncapped material [Jai94].

$\text{Si}_{1-x}\text{Ge}_x$ has an indirect band gap which spans the 0.85 to 1.35 μm range. The energy gap is different for the unstrained bulk alloy and coherently strained alloy. The energy gap is dependent upon both the Ge content and the

temperature. Figure 1-5 shows the composition dependence of the unstrained bulk alloy. The alloy has a Si-like Δ -conduction-band minimum from $x=0$ to $x \approx 0.85$. At this composition there is a crossover to the Ge-like L-conduction-band minimum [Lan85]. Compressive strain in the alloy produced by the underlying Si substrate reduces the $\text{Si}_{1-x}\text{Ge}_x$ bandgap energy. In $\text{Si}/\text{Si}_{1-x}\text{Ge}_x$ superlattices the bandgap is strongly influenced by not only the strain state, but also the layer thickness and period.

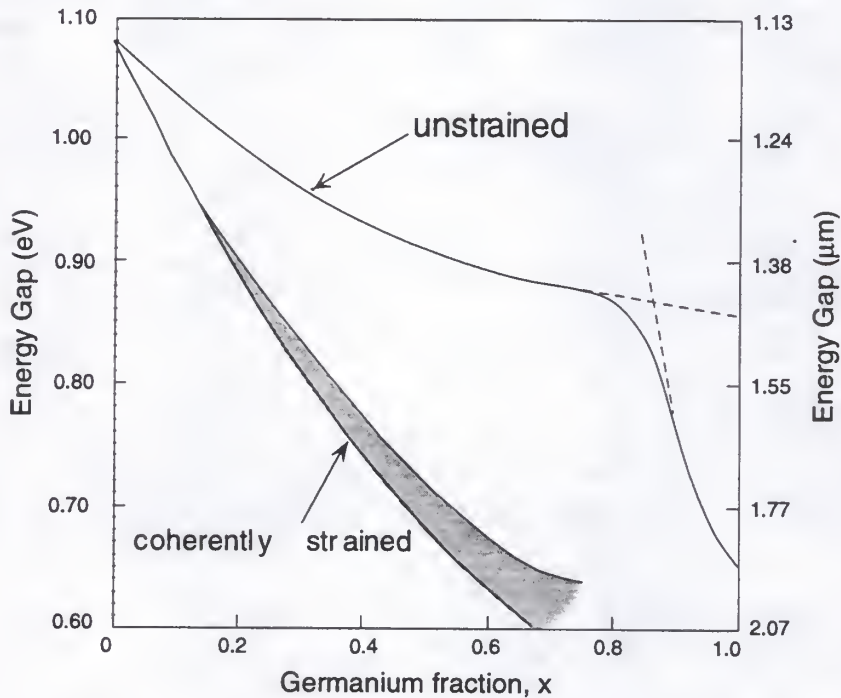


Figure 1-5. Energy gap versus germanium fraction for unstrained and coherently strained $\text{Si}_{1-x}\text{Ge}_x$ [Peo86].

1.1.2 Device Applications

The semiconductor industry has long been based on Si, yet Si technology is fast approaching its physical limits. Compound semiconductors made of elements in the III and V columns in the periodic table have been used in specific applications that require a tunable direct bandgap energy and high carrier mobilities. These III-V semiconductors, however, are more complex to process. Incorporating Ge into Si to create $\text{Si}_{1-x}\text{Ge}_x$ devices provides a good compromise between Si and compound semiconductor technology. $\text{Si}_{1-x}\text{Ge}_x$ technology allows bandgap engineering similar to that of compound semiconductors while retaining the economical and advanced aspects of Si technology. While $\text{Si}_{1-x}\text{Ge}_x$ technology is progressing rapidly, there are still drawbacks in device manufacturing. Of major concern is the lattice mismatch between Si and Ge (4.2%) which can cause growth and performance challenges for certain device applications. Table 1 summarizes the advantages and disadvantages of $\text{Si}_{1-x}\text{Ge}_x$ for device applications.

Table 1-1. Advantages and disadvantages of SiGe used in device applications.

Advantages	Disadvantages
<ul style="list-style-type: none"> • Able to bandgap tailor • Able to deposit atomically sharp SiGe interface • Economical • Can be incorporated into standard Si processing • Environmentally harmless 	<ul style="list-style-type: none"> • Large lattice mismatch Si-Ge • Large dopant out-diffusion • Indirect bandgap

Because Si and Ge form a continuous solid solution with a wide range of energy gaps, the alloy has a wide range of optical and electronical applications. The most common applications are in Heterojunction Bipolar Transistors (HBTs), Modulation Doped Field Effect Transistors (MODFETs) and quantum well light emitters and detectors. The incorporation of a narrow band-gap $\text{Si}_{1-x}\text{Ge}_x$ strained superlattice structure [Tem88] or bulk alloy in a Si bipolar junction transistor (BJT) has many advantages relative to a standard Si homojunction bipolar transistor. It offers increased emitter injection efficiency and current gain, lower base resistance, shorter base transit times, and better low temperature operation. Cut off frequencies, f_T , as high as 130 GHz for a $\text{Si}_{1-x}\text{Ge}_x$ HBT have been reported [Oda97], while f_T for Si BJTs are commonly ~ 75 GHz.

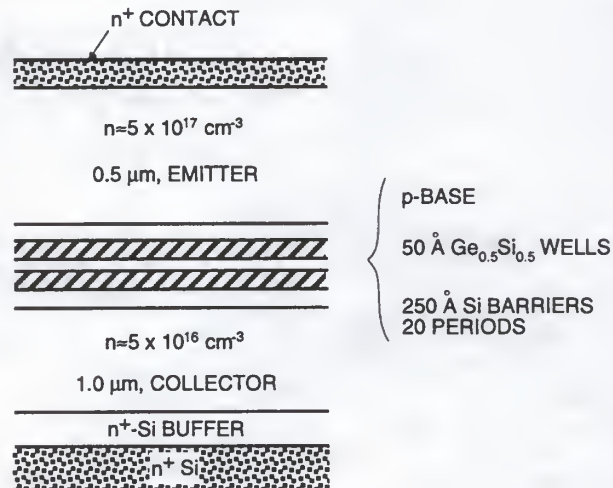


Figure 1-6. Cross-section of a $\text{Si}_{1-x}\text{Ge}_x$ HBT [Tem88].

In optoelectronic applications, both light detectors and emitters operating in the near ($1.3\mu\text{m}$) and mid-infrared ($\approx 10\mu\text{m}$) ranges can be fabricated using the Si-Ge system, particularly the $(\text{Si}_m\text{Ge}_n)_p$ superlattice system. The best of these photodetector devices use a waveguide rib where the light enters sideways through the rib and is absorbed in the active layer (Figure 1-7), making the absorption region and overall absorption larger than in vertical mesa-type structures, while having a geometry better suited for optical communication links.

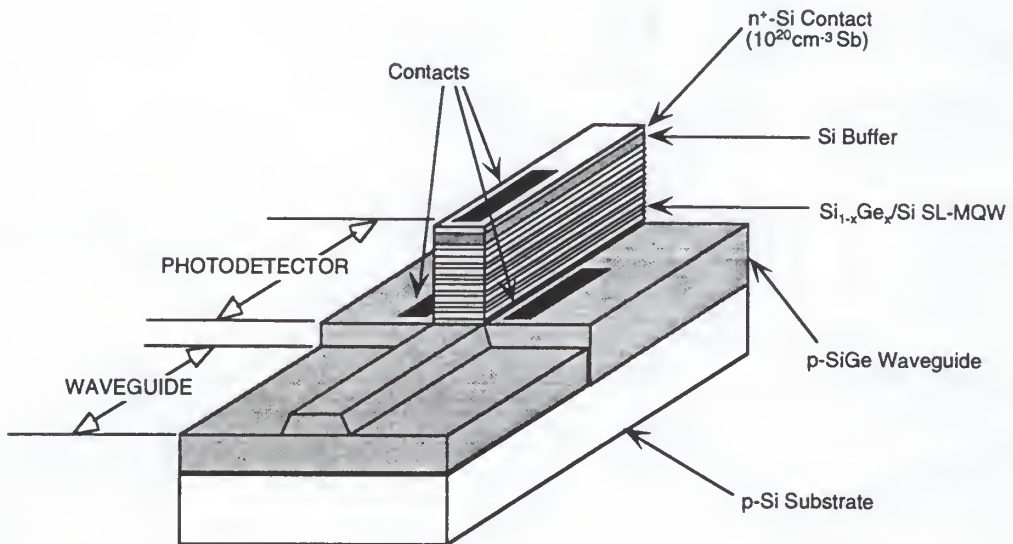


Figure 1-7. Possible waveguide-photodetector structure using $\text{Si}_{1-x}\text{Ge}_x$ alloy [Pre95].

$\text{Si}_{1-x}\text{Ge}_x$ heterostructures can be grown on either a Si or $\text{Si}_{1-x}\text{Ge}_x$ buffer creating band alignments which lead to spatial separation of ionized dopant atoms and mobile carriers which can be used in a MODFET. Electron

mobilities in these $\text{Si}_{1-x}\text{Ge}_x$ structures are almost five times higher than in the corresponding Si structures.

1.2 Strain and Strain Relaxation in SiGe Heterostructures

Strain develops when an epitaxial layer of a certain lattice parameter, a_e , is grown on a substrate of a differing lattice parameter, a_s . When $a_e < a_s$, the epitaxial layer is said to be under tensile strain. When $a_e > a_s$, the layer is under compressive strain. Regardless of the Ge composition, x , $\text{Si}_{1-x}\text{Ge}_x$ epitaxial layers grown on a Si buffer are always under compressive strain. As schematically depicted in Figure 1-8b, the cubic $\text{Si}_{1-x}\text{Ge}_x$ lattice theoretically is compressed so that the parallel lattice parameter, $a_{||}$, matches that of the cubic Si lattice. Because the total volume of the $\text{Si}_{1-x}\text{Ge}_x$ unit cell is considered constant, the perpendicular lattice parameter, a_{\perp} , increases, rendering the $\text{Si}_{1-x}\text{Ge}_x$ unit cell no longer cubic but tetragonal (termed tetragonal distortion). The $\text{Si}_{1-x}\text{Ge}_x$ monolayers are grown on top of each other this way and the strain energy stored in the dislocation-free film, E_{strain} , is described by:

$$E_{\text{strain}} = Mh\varepsilon^2 \quad (1-3)$$

where M is the biaxial elastic modulus of the epilayer, ε is the strain and h is the thickness of the epilayer. The energy necessary to generate a dislocation, $E_{\text{dislocation}}$, is described by:

$$E_{\text{dislocation}} = \frac{Gb^2}{4\pi(1-\sigma)} \frac{2}{\lambda} \ln\left(\frac{h}{b}\right) \quad (1-4)$$

where G is the shear modulus, assumed to be the same in the film and substrate, b is the Burger's vector of the dislocation, σ is Poisson's ratio, and $2/\lambda$ is the dislocation length per unit area of the epitaxial layer. When $E_{\text{strain}} > E_{\text{dislocation}}$, the epitaxial layer is fully strained and dislocation free, otherwise known as pseudomorphic. When $E_{\text{strain}} = E_{\text{dislocation}}$, the layer thickness is at a critical thickness, termed h_c (Section 1.1). Above this critical thickness, $E_{\text{dislocation}} > E_{\text{strain}}$ and it is energetically favorable to relieve strain through dislocation formation.

Epilayer strain is most often relieved through the growth and propagation of misfit dislocations. Misfit dislocations can be nucleated homogeneously, through dislocation loops or half loops present at the surface or an interface, or heterogeneously, through impurities or inclusions incorporated during the growth process. A misfit dislocation is commonly viewed as the creation of extra planes of atoms in the lattice structure (Figure 1-8c).

Geometrically, a misfit dislocation cannot terminate within the bulk of a crystal; it must either form a closed loop (terminate upon itself), join with another line defect, or end at the nearest free surface. Misfit dislocations rarely have sufficient propagation velocity to span across the entire lateral dimension of the crystal, thus they generally terminate by intersecting with a threading dislocation (Figure 1-9). Threading dislocations extend from the surface of the epitaxial material to the substrate, traversing through any intervening strained layers. They exist due to imperfections in the growth

process and can glide through a double/single kink motion. This movement allows propagation of misfit dislocations [Kas95, Jain94].

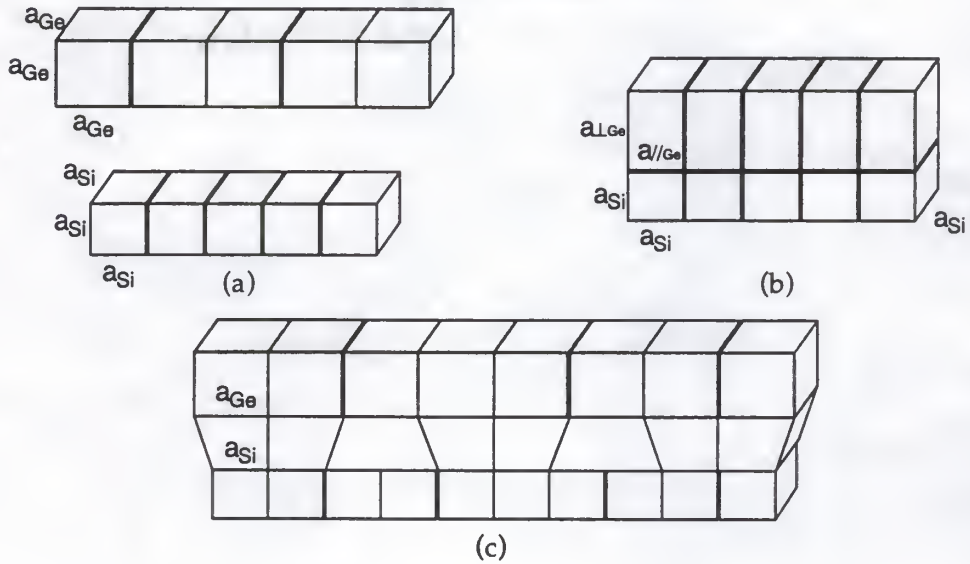


Figure 1-8. Evolution of a misfit dislocation at the Si and Ge interface. (a) an isolated Ge layer (gray), and an isolated Si layer (white) of smaller lattice constant, a_{Si} ; (b) the Ge layer is compressively strained in the parallel direction to match the Si substrate lattice constant to produce tetragonal distortion; (c) extra lattice planes are inserted as misfit dislocations as the Ge layer relaxes towards its original lattice constant.

Heterostructures used in device applications mentioned in Section 1.1 contain $Si_{1-x}Ge_x$ layers that are generally metastable with regard to misfit dislocation formation, due to either layer thickness or growth temperature. These heterostructures tend to relax through the injection and propagation of misfit dislocations at the $Si_{1-x}Ge_x/Si$ interfaces when subjected to high

temperature thermal treatment. Misfit dislocation propagation can lead to the simultaneous propagation of threading dislocations that can penetrate

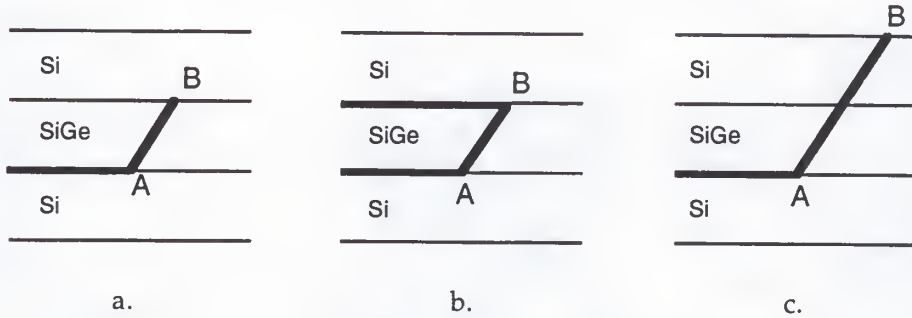


Figure 1-9. Termination of a misfit dislocation. (a) Misfit dislocation along a Si/ Si_{1-x}Ge_x interface meets a threading dislocation, AB; misfit terminates by (b) forming new misfit terminating at lateral surface or (c) termination of threading dislocation AB at free surface.

heterojunctions and increase current leakage. Heterostructures with dislocation densities greater than $\sim 10^3 \text{ cm}^{-2}$ are unsuitable for device applications [Hou91]. Thus, the characterization and quantification of dislocations in Si_{1-x}Ge_x/Si is vital in developing the material for device applications. Parts of this dissertation address whether dislocations alter the diffusion that occurs during high temperature thermal treatment (Sections 3.4.2 and 3.5.2) and whether dislocations capture the excess point defects injected during oxidation and nitridation (Sections 3.4.3 and 3.5.3), thus limiting or prohibiting their interaction in the diffusion process.

1.3 Diffusion in Elemental Semiconductors

Diffusion is the process in which random atomic motions result in the transport of matter from one part of a system to another. When an inhomogeneous single-phase alloy is annealed, matter will flow in a direction which will decrease the chemical potential gradient. If annealed sufficiently at constant temperature and pressure, the alloy will reach equilibrium: there will be no net flow of matter and the alloy will be homogeneous.

Diffusion in semiconductors can be examined through three different modeling approaches: (1) *empirical*, in which the diffusion is studied and described entirely through experimental analysis, (2) *semi-empirical*, in which mathematical models and experimental data are used conjunctively to indicate the diffusion process, and (3) *atomistic*, in which mathematical modeling is used almost exclusively to indicate how individual atoms are diffusing. The empirical approach has been used extensively to study self and dopant diffusion in silicon, most notably by Fair *et al.* [Fai75a, Fai75b, Fai77]. Examples of the semi-empirical approach include the FLorida Object Oriented Process Simulator (FLOOPS) [Law96] and the Stanford University Process and Engineering Models (SUPREM) [Han93]. In the semi-empirical approach, expressions for species diffusivities are developed from detailed atomistic mechanisms and these expressions are incorporated into a continuum description of the diffusion process. The parameters in the expressions for the species diffusion coefficients are estimated by a comparison with

experimental results. Monte Carlo (MC) and Molecular Dynamics (MD) simulations are examples of methods used in the atomistic approach. These are not common in complete modeling of diffusion because the small time scale limits their use to the study of unit steps of diffusion only.

1.3.1 Continuum Theory

Diffusivity values as well as fractional contributions to diffusion of interstitials and vacancies have been estimated in this work using the semi-empirical approach. Experimental results obtained through Secondary Ion Mass Spectrometry (SIMS) (Section 2.3) have been used to estimate parameters used in the continuum and atomistic mechanism models incorporated in FLOOPS. It is therefore important to describe the fundamentals of continuum theory in order to understand the models and results presented throughout this work.

The semi-empirical approach to describing diffusive transport in a diffusion couple is based on Fick's first law, which describes mathematically the flux in one dimension as:

$$F = -D \frac{\partial c}{\partial x} \quad (1-5)$$

where F is the flux of atoms, c is the concentration of the diffusing component, x is the space coordinate measured normal to the section, and D is the diffusion coefficient. The minus sign in Equation 1-5 indicates that the diffusion occurs in the direction of decreasing concentration. Fick's first law

is most useful in experimental situations with steady state diffusion, where $dc/dt=0$.

Fick's second law is normally used in systems with non-steady-state concentration. Combining Fick's law with the continuity equation for the diffusing species yields the diffusion equation:

$$\frac{\partial c}{\partial t} = \frac{\partial}{\partial x} \left[D \frac{\partial c}{\partial x} \right] \quad (1-6)$$

The solution to Equation 1-6 will be the concentration as a function of position and time, $c(x,t)$, for specified initial and boundary conditions. When the diffusion distance is short with respect to the dimensions of the structure, $c(x,t)$ is mostly expressed by error functions. For example, isothermal diffusion of a constant concentration source into a thick (infinite) substrate with a constant diffusion coefficient can be described by :

$$C = C_0 \operatorname{erfc} \frac{x}{2(Dt)^{1/2}} \quad (1-7)$$

where x is the depth into the semiconductor, C_0 is the concentration of the source at $x=0$, D is the diffusivity, and t is time. Solutions to the diffusion equations for many different boundary conditions can be found in several classic references [Cra75, Tuc74].

In the systems studied here, complexities in using Fick's law arise from two different sources: (1) the dependence of D on the properties of the system can be complex and (2) multiple equations must be written to describe multiple species. The value of D can vary with time (e.g., imposed

temperature variation and transient phenomena) and composition. The temperature dependence of the diffusion coefficient in solids is generally well described by an Arrhenius relation:

$$D = D_0 \exp(-E_a/kT) \quad (1-8)$$

where D_0 is the weakly temperature-dependent pre-exponential factor, E_a is the activation energy of transitions of the solute between adjacent lattice sites, k is the Boltzmann constant, and T is temperature. The magnitude of E_a can help to identify the diffusion mechanism. Both D_0 and E_a can depend on the strain state, composition, and gas ambient (e.g., inert, oxidizing, or nitriding).

1.3.2 Point Defects and Diffusion Mechanisms

Derivation of a form for D used in continuum equations necessitates an understanding of the atomistic mechanism by which the diffusing species migrates through the crystal lattice. Hence, the coupling of a continuum approach to describe the spatial and temporal concentration dependency and an atomistic approach to describe the functional form of the mass diffusivity is the basis of the semi-empirical approach. There are several atomic pathways available for diffusion, of which the ring, interstitial, and vacancy mechanisms are the most elementary.

The ring mechanism is simply the exchange of two neighboring lattice atoms, without the involvement of point defects. This mechanism has not been seen experimentally, and would be theoretically improbable due the

large activation energy required for the exchange [Had95]. It will be ignored as a possible diffusion pathway for the rest of this dissertation.

The direct interstitial mechanism is movement of either a self or impurity atom from interstitial site to interstitial site through the lattice, as schematically shown in Figure 1-10. This mechanism is energetically possible for self interstitials or impurities which are small compared to the host lattice atoms; it is energetically unfavorable for atoms which are large compared to the lattice atoms, due to the lattice distortions involved [She89, Bor88].

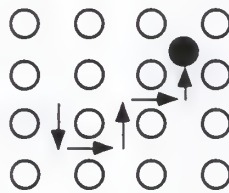


Figure 1-10. The direct interstitial mechanism.

Lattice sites that are unoccupied are known as vacancies. The vacancy mechanism is movement of a self or impurity atom sitting on a lattice site into a neighboring vacancy, occupying that site substitutionally (Figure 1-11). There will be a net flux of vacancies equal and opposite to the flux of the diffusing species. The amount of diffusion that occurs via the vacancy mechanism depends on the probability that an atom rests next to a vacancy, which in turn, depends on the total mole fraction of vacancies in the crystal [She89, Bor88].

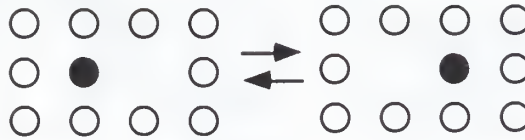


Figure 1-11. The vacancy mechanism.

The simple mechanisms just discussed are generally insufficient individually to predict the diffusion of self or impurity atoms in a semiconductor crystal. Self and impurity diffusion in both Si and GaAs have shown to be some combination of the vacancy and interstitial mechanisms discussed above, involving both interstitial *and* vacancy point defects [Fra91, Had95]. The approach used in this dissertation to model Si-Ge diffusion has assumed a similar cooperative contribution of interstitials and vacancies, therefore it is important to consider both substitutional and interstitial mechanisms while examining $\text{Si}_{1-x}\text{Ge}_x$ interdiffusion. It is important, however, to note that the mechanism of Ge diffusion in $\text{Si}_{1-x}\text{Ge}_x$ is slightly different than the usual impurity diffusion in either Si or GaAs, as the Ge “impurity” is neutral within the $\text{Si}_{1-x}\text{Ge}_x$ lattice. Due to the neutrality of the Ge in $\text{Si}_{1-x}\text{Ge}_x$ this thesis ignores the possibility of pair model diffusion [Had95], which normally occurs when the point defect and impurity are both charged.

The substitutional-interstitial diffusion model (SID) offers two plausible mechanisms which couple the impurity atoms and native point defects. In each mechanism, the mobile species is the impurity interstitial. The first mechanism, known as the Frank-Turnbull or dissociative

mechanism, describes the movement of an impurity atom from a substitutional site to an interstitial site, leaving behind a vacancy (reverse reaction in Figure 1-12). The mechanism is both interstitial- and vacancy-dependent. The diffusion equation for the impurity, in this case Ge, is given as [Had95]:

$$\frac{\partial C_{\text{Ge(S)}}}{\partial t} = \nabla \left\{ D_{\text{Ge}} C_{\text{Ge(S)}} \frac{C_v^*}{C_v} \nabla \ln \left(C_{\text{Ge}} \frac{C_v^*}{C_v} \frac{p}{n_i} \right) \right\} \quad (1-9)$$

where $C_{\text{Ge(S)}}$ is the concentration of impurities occupying substitutional sites, C_v and C_v^* are the actual and equilibrium concentrations of vacancies, respectively, p is the hole density, and n_i is the intrinsic carrier concentration. D_{Ge} is described by:

$$D_{\text{Ge}} = f_i \sum_j D_i^j \left(\frac{p}{n_i} \right)^{j+1} \quad (1-10)$$

where f_i is the fraction of diffusion that occurs via interstitials, and D_i^j is the diffusivity of the interstitial impurity in charge state j .

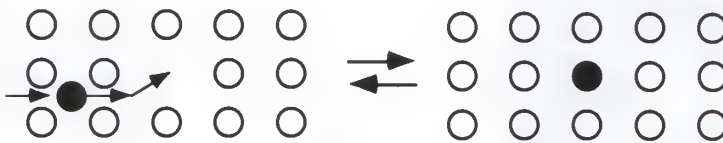


Figure 1-12. The Frank-Turnbull (dissociative) mechanism. The black atom represents the impurity atom.

The second mechanism, known as the kick-out mechanism, describes the movement of an impurity interstitial into a substitutional site, causing a lattice atom to be bumped into an interstitial position (Figure 1-13).

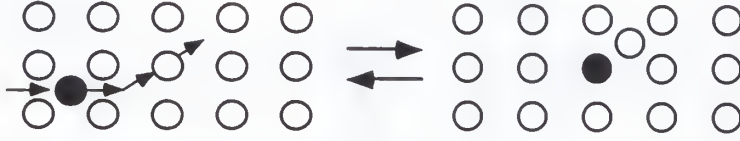


Figure 1-13. The kick-out mechanism.

Unlike the Frank-Turnbull mechanism, the kick-out mechanism is dependent on the interstitial concentration only, and the diffusion equation for the impurity (Ge) can be described by [Had95]:

$$\frac{\partial C_{\text{Ge(S)}}}{\partial t} = \nabla \left\{ D_{\text{Ge}} C_{\text{Ge(S)}} \frac{C_I^*}{C_I} \nabla \ln \left(C_{\text{Ge}} \frac{C_I^*}{C_I} \frac{p}{n_i} \right) \right\} \quad (1-11)$$

where C_I and C_I^* are the non-equilibrium and equilibrium concentrations of interstitials, respectively. The continuity equations for the interstitials and vacancies in either the Frank-Turnbull or kick-out mechanism are:

$$\frac{\partial C_I}{\partial t} = \nabla \left(D_I C_I^* \nabla \frac{C_I}{C_I^*} \right) + \nabla (-J_{\text{mech}}) - k_r (C_I C_V - C_I^* C_V^*) + \phi_I^s \quad (1-12)$$

$$\frac{\partial C_V}{\partial t} = \nabla \left(D_V C_V^* \nabla \frac{C_V}{C_V^*} \right) + \nabla (-J_{\text{mech}}) - k_r (C_I C_V - C_I^* C_V^*) - \phi_V^s \quad (1-13)$$

where D_I and D_V are the interstitial and vacancy diffusivities, respectively, J_{mech} is the flux of the impurity diffusing by the mechanism in consideration, k_r is

the interstitial-vacancy first-order recombination rate, and ϕ_I^s and ϕ_V^s are any independent sources or sinks for interstitials and vacancies, respectively. By solving the continuity equations for all species involved for a specific diffusion mechanism (e.g., Equations 1-11 through 1-13 for a kickout mechanism), an expression for D can be reached.

At thermal equilibrium, the concentration of point defects is the single most important influence on diffusion within the atomic lattice. The neutral point defects can accept or donate an electron to become a charged defect, which in turn can accept or donate another electron to become doubly charged and so forth. The thermal equilibrium concentrations of charged point defects depends on the Fermi level of the crystal as well as the electronic level position in the bandgap corresponding to the defect. Hence, the total concentration of point defects at thermal equilibrium are known functions of the Fermi level and temperature. These quantities are denoted C_I^* and C_V^* , as mentioned above and are given by [Had95]:

$$C_X^* = \sum_j \phi_j \left(\frac{p}{n_i} \right)^j \quad j=0, \pm 1, \pm 2, \dots \pm n \quad (1-14)$$

where X represents either I or V and ϕ_j is a constant which represents the contribution from the bandgap position, and j is the charge state of the defect.

1.4 Non-equilibrium Point Defect Injection

The generation and annihilation of non-equilibrium point defects is a topic which is crucial for the understanding of semiconductor diffusion phenomena. It has been generally accepted that thermal oxidation of silicon injects interstitials, while thermal nitridation injects vacancies [Fah89a, Hu92]. The proportional dependence of a material's self-diffusion mechanism or dopant's diffusion mechanism on these defects can be determined by monitoring any enhancement or retardation of the diffusion with the addition of these defects. The total diffusivity of the self or dopant atom being studied can be described as the sum of the vacancy and interstitial diffusivities:

$$D = D_i + D_v \quad (1-15)$$

where, in the case of Ge diffusion in Si, D is equivalent to D_{Ge} in Equation 1-11, and D_i and D_v are equivalent to the variables by the same name in Equations 1-12 and 1-13. The fractional interstitial component of diffusivity, f_i , is defined as:

$$f_i \equiv \frac{D_i^*}{D_i^* + D_v^*} = \frac{D_i^*}{D^*} \quad (1-16)$$

where D^* denotes the value of the diffusivity when the actual interstitial and vacancy concentrations are their equilibrium values, which occurs when diffusing in a high temperature, inert ambient. The fractional vacancy component, f_v , is simply $(1-f_i)$. Under nonequilibrium conditions, as during

oxidation or nitridation, there will be an enhancement of the effective diffusivity given by:

$$\text{enh} = \frac{D}{D^*} = f_I \frac{C_I}{C_I^*} + (1 - f_I) \frac{C_V}{C_V^*} \quad (1-17)$$

where C_I and C_V are the actual concentrations and C_I^* and C_V^* are the equilibrium concentrations of vacancies and interstitials. Note that if $\text{enh} < 1$ diffusion is retarded rather than enhanced. If D^* is known, f_I may be estimated from measuring enh during oxidation or nitridation and comparing with dopants for which f_I is known (e.g., phosphorous, $f_I=1$). This is explained in detail in Section 3.3.

1.4.1 Interstitial Injection (Oxide Growth)

As stated in Section 1.4, oxidation of the silicon surface results in the injection of interstitial point defects into the Si bulk. During oxidation, oxygen gas reacts with the Si surface and the rate is controlled by the overall chemical reaction:



The silicon dioxide layer continues to grow by the transport of oxygen species through the oxide layer to the Si-SiO₂ interface where it reacts with the Si [Dea65]. The formation of the oxide causes the Si to be consumed so that for every angstrom of oxide grown, approximately a half angstrom of the Si surface is consumed [May90].

The supersaturation of interstitials produced by oxidation in the range of temperatures used in this dissertation is well documented [Pac91] and will be used to model the dependence of interdiffusion on interstitials. For example, Packan and Plummer [Pac90] estimated $C_i/C_i^* \sim 13$ resulting from dry oxidation for 1 hour at 900 °C. They also found that interstitial supersaturation was dependent on oxide growth velocity.

While there are a substantial number of theories, there has yet to be a proven mechanism for injection of interstitials through the formation of SiO_2 thin films. Several theories are briefly reviewed here: (1) Dunham and Plummer [Dun86] proposed that interstitials created by the oxidation process accumulate in the SiO_2 layer near the interface. The difference between the rate of interstitial creation and the flux of the interstitials into the oxide causes the interstitials to diffuse into the bulk. (2) Tan and Gösele [Tan81] proposed that the free volume difference between the Si and SiO_2 at the interface causes viscoelastic flow of the SiO_2 resulting in a supersaturation of interstitials. (3) Hu [Hu74] proposed that a fraction of silicon available is not oxidized and Si atoms are displaced from their lattice sites by the advancing SiO_2/Si interface, becoming interstitials. Unfortunately, none of these theories has been supported by experimental evidence and an accurate model must still be established. It is sufficient for the purposes of these investigations, however, to know that interstitials are indeed injected.

1.4.2 Vacancy Injection (Nitride Growth)

As described in Section 1.4, it has been well-established that the nitridation of the Si surface results in the injection of vacancies into the bulk.

The overall nitridation reaction that occurs is:



In a variety of growth conditions, there is an initial fast-growth regime, followed by a very slow growth regime in which the total thermal nitride layer grows no thicker than approximately 4 nm [Hay82, Mos85a] regardless of processing time. It is also important to note here that direct thermal nitridation of a bare silicon surface results in nitride films with a substantial amount of oxygen (the ratio of the concentration of nitrogen to the total concentration of nitrogen and oxygen is approximately 50 %: $[\text{N}]/([\text{N}]+[\text{O}]) \approx 0.50$) [Mog96, Mur79, Hay82]. Technically these films are oxynitrides, yet in this dissertation they will be termed simply 'nitrides'.

Quantitatively, the supersaturation of vacancies produced by nitridation of silicon in the range of temperatures used in this dissertation is not as well documented as in the oxidation/interstitial injection case. Mogi [Mog96] performed one of the most extensive investigations to date, and found $C_v/C_v^* \sim 4$ resulting from thermal nitridation in NH_3 for 1 hour at 910 °C. His results will be used to model the dependence of interdiffusion on vacancies.

Like the oxidation process, the process of vacancy injection is not well understood. The injection of vacancies is thought to be the result of stress at the nitride/silicon interface, causing interstitials at the interface to move into the nitride layer and vacancies to move into the Si bulk [Hay82, Osa95]. No mechanism has been substantiated and better studies are needed.

1.5 Literature Review

1.5.1 Self-Diffusion and Intrinsic Interdiffusion

1.5.1.1 Self-diffusion

Vacancies and self-interstitials in Si coexist under thermal equilibrium at all temperatures above the athermal regime. Based on the results of early studies, Si self-diffusion was thought to be due entirely to a vacancy mechanism. Through Ge tracer studies, Seeger and Chik [See68] found a break in the Arrhenius curve and subsequently proposed self-diffusion dominated by vacancies at temperatures below ~ 1000 °C, and interstitials at temperatures above. In 1974 Hu [Hu74] was the first to suggest a dual mechanism which included both vacancies and interstitials at all temperatures in the range 700 to 1200 °C. This was the mechanism that most researchers agreed upon until experiments involving oxidation enhanced diffusion established that Si predominantly diffuses by an interstitial mechanism at temperatures above 800 °C. The reported activation energies for Si self-diffusion range from 4 to 5 eV.

Si and Ge are very similar in their elemental properties, thus it is surprising that they differ so significantly in their self-diffusion mechanisms and the defects present in thermal equilibrium. Unlike Si, there is very little debate over the mechanism of Ge self-diffusion. Effects of hydrostatic pressure [Wer85], dopant studies [Sto85] and calculations of interstitial migration energies [Kho90] all conclude that diffusion occurs exclusively via monovacancies. The work of Mitha *et al.* [Mit96] is the only investigation to disagree, claiming that the smaller-than-expected activation volume opens the door for possible interstitialcy and direct exchange contributions. They imply, however, that these contributions would be relatively small. The activation energy for Ge self-diffusion is ~ 3 eV, with a pre-exponential value on the order of $\sim 10^{-3} \text{ m}^2/\text{s}$ [Wer85, Sto85]. The large difference of 1 to 2 eV between the activation energies for Si self-diffusion and Ge self-diffusion as well as the interstitial dominated as compared to the vacancy dominated mechanism above 800 °C suggest that there must be a strong concentration dependence of Si-Ge interdiffusion in $\text{Si}_{1-x}\text{Ge}_x$ structures.

1.5.1.2 Tracer studies of Ge in Si

Thermally activated interdiffusion studies of Si-Ge systems have shown that interdiffusion occurs most likely through Ge atoms which diffuse into the Si lattice; therefore, it is imperative to discuss the diffusion of Ge in Si. While the values of the tracer diffusivity and activation energy of diffusion (5.39 eV over a temperature range of 850 to 1400 °C) of Ge in Si agree well from study to study [Bou86, Dor84], the dispute that arises is the same as

for Si self-diffusion. Is there a break in the Arrhenius line where the mechanism changes from interstitial to vacancy at lower temperature? Seeger and Chik [See68] were the first to propose that the diffusion takes place via a dual interstitial and vacancy mechanism. They claimed that diffusion is dominated by interstitials at high temperatures and vacancies at low temperatures with cross-over at ~ 1050 °C. Dorner *et al.* [Dor84] observed a break in the curve at about 1050 °C but Bouchetout *et al.* [Bou86], Hettich *et al.* [Het79], and McVay and Ducharme [McV74] observed none. Fahey *et al.* [Fah89b] were the only researchers to actually report the fraction of diffusion proceeding via an interstitial or vacancy mechanism. Their study, however, was only for the single temperature 1050 °C, the temperature of the disputed break. At this temperature they proposed a mechanism with 30 to 40% interstitial assisted diffusion and 70 to 80% vacancy assisted diffusion. There are several issues associated with this conclusion: (1) they assume a kickout mechanism as opposed to a dissociative mechanism for interstitial movement (2) they do not address the question of the Arrhenius break and (3) the samples underwent oxidation anneal before having the oxynitride layer deposited and then annealed. It is obvious that more studies are needed to verify the relative contributions as well as exact mechanism of vacancy and interstitial movement of Ge atoms in Si.

1.5.1.3 Diffusion studies of $\text{Si}_{1-x}\text{Ge}_x/\text{Si}$ heterostructures

There have been many studies of the interdiffusion in $\text{Si}/\text{Si}_{1-x}\text{Ge}_x/\text{Si}$ single quantum well (SQW) structures, $(\text{Si}_m\text{Ge}_n)_p$ superlattices and $\text{Si}/\text{Si}_{1-x}\text{Ge}_x$

superlattices. The interdiffusion is found to be dependent upon such primary variables as Ge content, x , the amount and type of strain, ϵ , and anneal temperature, T , as well as secondary variables such as thickness of the layers, d , and time of anneal, t . The wide range of parameters makes it difficult to compile a comparison between the data. For example, small differences in strain create large differences in diffusion coefficients. Compositionally, it has been found that the interdiffusivity increases by an order of magnitude with each approximately 0.10 step increase in x . From $x=1$ to $x=0$, the diffusivity can change by as much as six orders of magnitude [Hol92, Van90].

Diffusion in strained $\text{Si}_{1-x}\text{Ge}_x/\text{Si}$ single quantum wells has been found to have an activation energy of ~ 3 eV [Hol92, Van90, Sun94]. While the extent of diffusion can be estimated using the tracer Ge diffusion coefficient in bulk Si, all studies see an increasing deviation with decreasing anneal temperature. Some studies contend that strain relaxation leads to a change in diffusivity with temperature, while others believe that change in local Ge concentration, not strain relaxation, is the reason for the difference in diffusivity. None of the studies proposes a possible diffusion mechanism.

Interdiffusion of $\text{Si}_{1-x}\text{Ge}_x/\text{Si}$ superlattice layers is different than in SQW structures due to the ability to engineer the strain state of the material by the layer structure. $\text{Si}_{1-x}\text{Ge}_x/\text{Si}$ superlattices can be grown with two different types of coherent strain, asymmetric or symmetric. In an asymmetrically-strained superlattice (ASL), most commonly the Si layers are almost stress-free while the $\text{Si}_{1-x}\text{Ge}_x$ layers are under biaxial compressive stress and annealing causes

relaxation of the inherent strain. In a symmetrically-strained superlattice (SSL), a $\text{Si}_{1-y}\text{Ge}_y$ buffer layer is first grown on the substrate causing the Si and $\text{Si}_{1-x}\text{Ge}_x$ layers to be alternately under tensile and compressive strain ($y < x$). These alternating strains of equal magnitude lead to a structure which is theoretically strain-free.

In the case of $\text{Si}_{1-x}\text{Ge}_x/\text{Si}$ SLs there is no agreement among the various reported values of diffusivities and activation energies. Some investigations have reported energies as high as 5.0 eV [Bea85] while others have reported energies as low as 2.1 eV [Lui96]. The high activation energies support the theory that diffusion is controlled by the migration of Ge, first through the $\text{Si}_{1-x}\text{Ge}_x$ layers and then into the Si layers since Ge diffusion in Si has an activation energy of ~5 eV. The studies reporting low activation energies do not suggest any possible mechanism, nor do they reach a conclusion regarding the discrepancy with the high activation energy studies. The only explanation given is that the deviation may arise due to differences in sample structures, annealing temperatures and times, or data analysis method.

1.5.2 Oxidation and Nitridation Enhanced Diffusion

A review of the literature reveals that there has been only one investigation of Ge diffusion in strained $\text{Si}_{1-x}\text{Ge}_x$ under an oxidizing ambient. Cowern *et al.* [Cow96] investigated Ge diffusion throughout a structure with a coherent $\text{Si}_{0.70}\text{Ge}_{0.30}$ layer. For a single anneal temperature of 875 °C, they determined that diffusion is predominately vacancy-mediated, and estimated a f_i of 0.22 ± 0.04 . They also calculated an enhancement under oxidizing

ambient compared to inert ambient of $D/D^*=3.6$. No diffusivity values were reported and no activation energy was calculated. There are no known investigations of Ge diffusion in $\text{Si}_{1-x}\text{Ge}_x$ under nitriding ambient.

There has been limited investigation of oxidation and nitridation enhanced diffusion of impurities in $\text{Si}/\text{Si}_{1-x}\text{Ge}_x/\text{Si}$ SQW structures. An excellent summary of research to date can be found in Nylandsted Larsen *et al.* [Nyl97]. Kuo *et al.* [Kuo95] measured the diffusivity of boron in $\text{Si}/\text{Si}_{1-x}\text{Ge}_x/\text{Si}$ SQWs and found that the oxidation enhanced diffusion (OED) enhancement factor was comparable to that in Si, $f_{\text{enh}} \approx 10$. The diffusivity of B in $\text{Si}_{1-x}\text{Ge}_x$, however, was less than that in Si by almost half. While there is no explanation for the difference in B diffusivity between the materials, the similarity of enhancement indicates that the interstitial contribution of B diffusion in $\text{Si}_{1-x}\text{Ge}_x$ is comparable to that in Si. Kuo *et al.*'s investigation was limited to data for only one anneal temperature, 800 °C. Fang [Fan96] measured nitridation retarded diffusion (NRD) of B in $\text{Si}_{1-x}\text{Ge}_x$ SQWs at one temperature, 850 °C. She found that the retardation factor in $\text{Si}_{1-x}\text{Ge}_x$ was comparable to that in Si, $f_{\text{ret}} \approx 0.8$, and she also found a smaller intrinsic B diffusion in $\text{Si}_{1-x}\text{Ge}_x$ than Si.

CHAPTER 2 SAMPLE PREPARATION AND CHARACTERIZATION

2.1 Growth Parameters and Structure

Four sample structures were used in this investigation to determine the interdiffusion behavior of $\text{Si}/\text{Si}_{1-x}\text{Ge}_x$. Three structures were grown using an ASM Epsilon 1 vapor phase epitaxial instrument. Figure 2-1(a) shows a strained SL structure grown on a $\text{Si}_{0.85}\text{Ge}_{0.15}$ buffer layer, hereafter referred to as sample structure SL/SiGe. This structure consists of a (100) Si substrate followed by a 100 nm ungraded $\text{Si}_{0.85}\text{Ge}_{0.15}$ buffer and 15 periods of 6 nm $\text{Si}_{0.85}\text{Ge}_{0.15}$ and 12 nm Si. Figure 2-1(b) shows another strained SL structure but grown on a Si buffer layer, hereafter referred to as sample structure SL/Si. This structure consists of a (100) Si substrate followed by a 100 nm Si buffer, 16 periods of 6 nm $\text{Si}_{0.86}\text{Ge}_{0.15}$ and 12 nm Si, and capped with 50 nm of Si. Figure 2-1(c) shows the structure of a SQW, hereafter referred to as sample structure SQW/VPE, which consists of a (100) Si substrate followed by a 100 nm Si buffer layer, a 50 nm layer of $\text{Si}_{0.85}\text{Ge}_{0.15}$, and a 50 nm Si cap.

The final structure was grown by Molecular Beam Epitaxy (MBE). Figure 2-2 shows a strained single quantum well (SQW) structure, hereafter referred to as sample structure SQW/MBE, which consists of a Si (100) substrate with a 100 nm Si buffer layer, a 50 nm $\text{Si}_{0.85}\text{Ge}_{0.15}$ with a 50 nm Si cap.

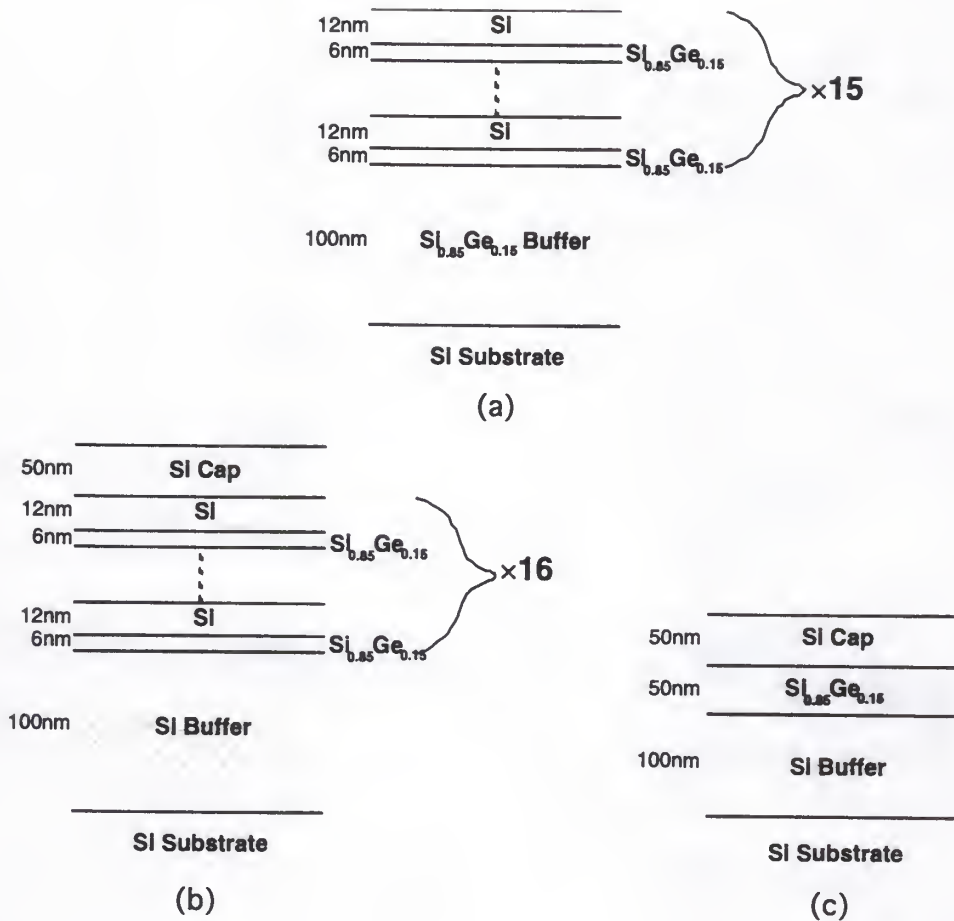


Figure 2-1. $\text{Si}_{1-x}\text{Ge}_x$ sample structures used in these investigations. (a) Sample structure SL/SiGe, a strained superlattice on a $\text{Si}_{1-x}\text{Ge}_x$ buffer (b) sample structure SL/Si, a strained superlattice on a Si buffer (c) sample structure SQW/VPE, a single quantum well.

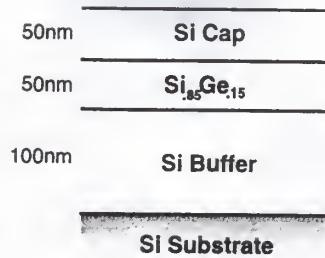


Figure 2-2. Sample structure SQW/MBE, a single quantum well grown by MBE.

Secondary ion mass spectrometry (SIMS) and cross-sectional transmission electron microscopy (XTEM) were performed on each sample structure to verify the thickness of the layers as well as the number of periods. Rutherford Backscattering Spectrometry (RBS) verified the Ge content using He^{2+} ions with a beam current of 10nA and a collector charge of 4 mC. Each sample was rotated 10° and tilted 10° to prevent channeling. The $\text{Si}_{1-x}\text{Ge}_x$ layers in all structures were shown to have the same Ge content (≈ 0.15) within experimental error (5%) [Sch90].

From Figure 1-3, the critical thicknesses of a capped $\text{Si}_{1-x}\text{Ge}_x$ layer with a Ge composition of 0.15 is $h_c \sim 30\text{nm}$. The 50 nm thicknesses of the $\text{Si}_{1-x}\text{Ge}_x$ layers of both sample structure SQW/VPE and SQW/MBE exceeded this critical thickness, therefore misfit dislocations were expected to be present in the materials. The structures were consequently examined by plan view TEM to determine qualitatively their dislocation densities (Section 2.2.3.2).

To determine the critical thickness for a multilayer structure, the conventional method is to reduce the multilayer to an equivalent single

strained layer. Kasper [Kas95] cites a model in which the average Ge content, x_{av} , is determined by:

$$x_{av} = \frac{xd_{SiGe}}{d_{SiGe} + d_{Si}} \quad (2-1)$$

where x is the Ge composition in the $Si_{1-x}Ge_x$ layer, d_{SiGe} is the thickness of the $Si_{1-x}Ge_x$ layers and d_{Si} is the thickness of the Si layers. Using this equation, the Ge concentration averaged over all multilayers of SL structures SL/SiGe and SL/Si was $x=0.05$. The critical thickness of a capped layer of $Si_{1-x}Ge_x$ grown on a Si buffer is $h_c \sim 100$ nm (Figure 1-4). The total multilayer thickness of structure SL/Si, 288 nm, greatly exceeded this value, therefore misfit dislocations were expected to be present. For structure SL/SiGe an average Ge composition of $x=0.05$ created a 'bulk' lattice constant of 0.5441 nm, leading to a lattice mismatch with the $Si_{0.85}Ge_{0.15}$ buffer of 0.18%. The critical layer thickness, h_c , of an uncapped $Si_{1-x}Ge_x$ layer with a lattice mismatch, f_m , of 0.0018, was approximately 80 nm [Jai93]. The total thickness of the 'pseudo-epilayer' of structure SL/SiGe was 270 nm which was more than three times the critical layer thickness; therefore, like the SL/Si structure, dislocations were expected to exist in structure SL/SiGe.

2.2 Transmission Electron Microscopy

2.2.1 Overview

In transmission electron microscopy (TEM) electrons from an electron gun are accelerated to high voltages (100 to 400 kV) and focused onto a sample

of interest using a condenser lens. The sample is sufficiently thin that the majority of impinging electrons are transmitted or forward scattered through the sample, rather than backscattered or absorbed. These transmitted and forward scattered electrons pass through an objective lens to form a back focal plane and an image plane (Figure 2-3). A diffraction pattern is formed on the back focal plane and a magnified image is formed on the image plane. Both the diffraction pattern and the magnified image can be projected onto a screen for either viewing or photographic recording [Wil96, Run98, Sch90].

There are two basic views of the sample that can be achieved through TEM, depending on the original sample preparation. Plan-view TEM (PTM) provides an image of the sample from a direction parallel to layer growth

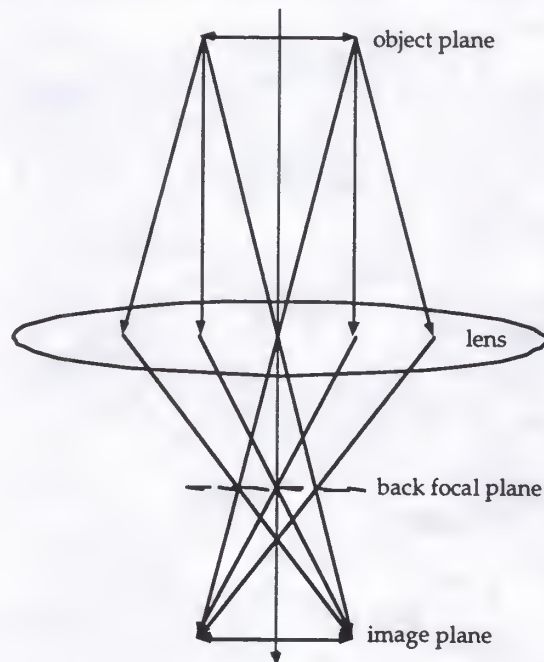


Figure 2-3. Schematic of ray paths originating from the object which create a TEM image [Wil96].

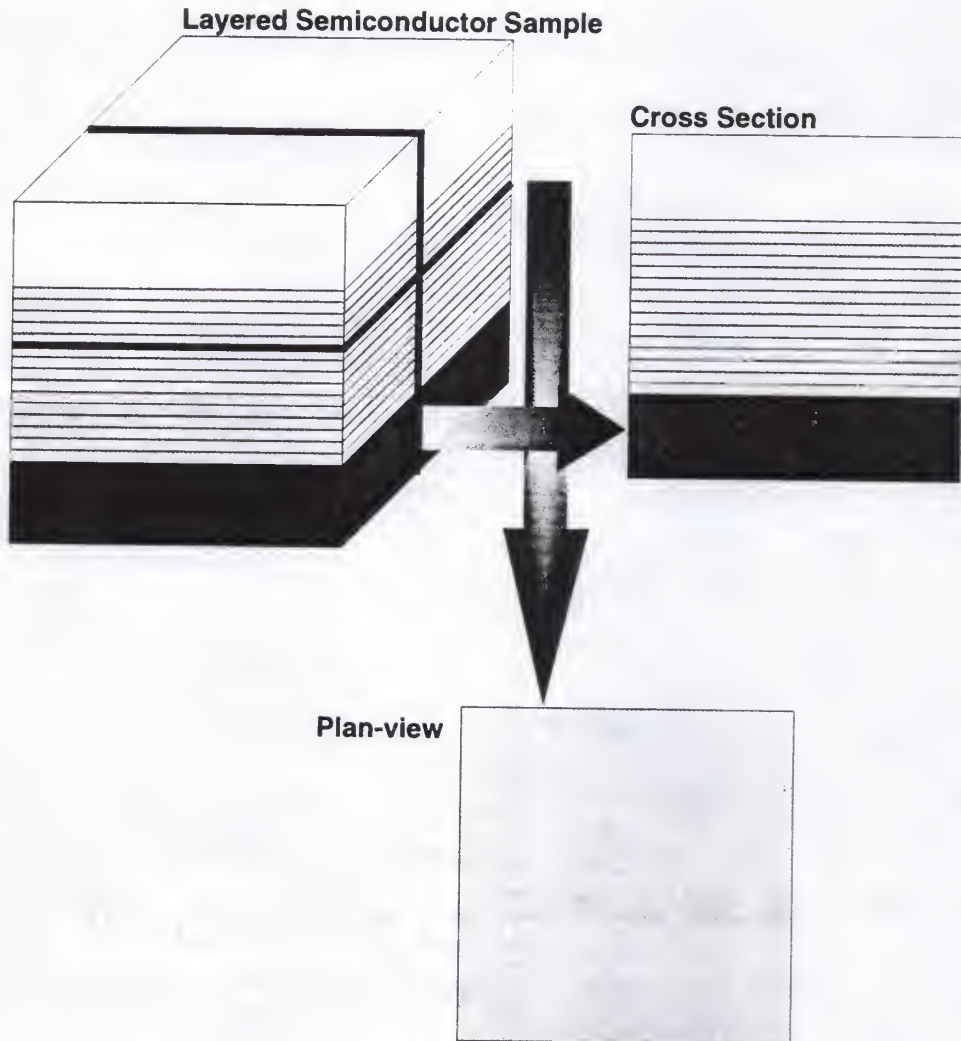


Figure 2-4. Schematic of TEM views. Both cross-sectional and plan view of the semiconductor sample can be obtained.

direction (Figure 2-4), essentially providing a view looking down at the top of the sample. Cross-sectional TEM (XTEM) provides an image of the sample (Figure 2-4) perpendicular to layer growth direction, as if one were looking at a slice of the sample from a side direction.

PTEM was used specifically in this work to determine qualitatively the density of misfit and threading dislocations and their lengths. PTEM was also used to observe their evolution with increasing time and temperature, as well as how they differed in inert, oxidizing and nitriding environments. XTEM is used in this work to determine the quality of the layer interfaces (sharpness, flatness), as well as the thickness of the layers. The grayscale contrast of the Si and $\text{Si}_{1-x}\text{Ge}_x$ layers allowed the observation of smearing of the interface due to diffusion after annealing. XTEM was also used to observe any threading dislocation evolution from the substrate/buffer interface to the surface.

2.2.2 TEM Sample Preparation

Procedures for sample preparation for PTEM and XTEM applications are quite different. Also, individual techniques used in both cases vary from researcher to researcher. The following sections describe the preparation methods used to create TEM images shown in this work.

2.2.2.1 Plan view

To provide a top surface view, preparation was begun by coring a circular piece out of the sample and mechanically thinning the backside of this core using a 15 μm powder. The top surface of the thinned piece was

then coated with wax to prevent etching, while the backside was etched using a solution of 25% HF: 75% HNO_3 . The sample was etched until a small hole with a slightly frayed edge developed at the center. This provided a region of the sample that was sufficiently thin for the electrons to be transmitted in the microscope and an image of the sample to be obtained.

2.2.2.2 Cross-sectional

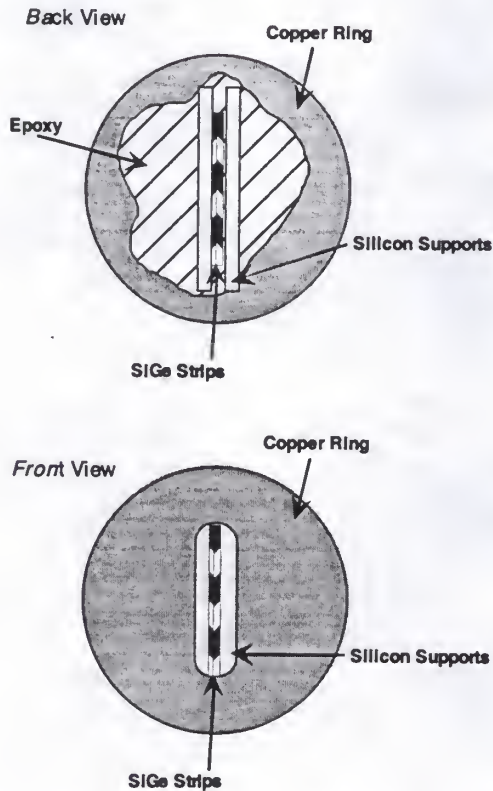


Figure 2-5. Front and rear views of the XTEM assembly after preparation [Wil96].

XTEM preparation was begun by slicing the sample into thin sections approximately 25 milli-inches wide. Two of these sections were glued together, surface to surface, with M600 Bond epoxy. This structure was sandwiched between two thin sections of Si, which acted as structural support (Figure 2-5).

The entire stack was mechanically thinned to $\sim 15 \mu\text{m}$ and polished. A 3mm copper ring was attached via G Bond epoxy to one side of the sample. This composite structure was thinned in a two stage Gatan 600 dual ion mill using Ar^+ ions at a gun voltage of 5kV and a current of 0.5 mA. Ion milling is a process in which low energy Ar^+ ions bombard both exposed sides of the sample at low angles, slowly knocking off surface atoms, eventually thinning the sample to a bowl-shaped cavity just breaking a hole into the back surface. This minimum thickness allows electrons to be transmitted through the sample and an image of the cross section to be formed in the microscope.

2.2.3 Images of Structures

As-grown and annealed samples were analyzed by cross-sectional and plan-view TEM using a JEOL 4000FX for high resolution images and a JEOL 200CX for low resolution images.

2.2.3.1 XTEM

XTEM photos were taken of the as-grown structures to verify the layer thicknesses, number of periods, as well as quality of the interfaces. The Si and $\text{Si}_{1-x}\text{Ge}_x$ layers were imaged by absorption contrast due to differences in atomic number. Figure 2-6a shows the as-grown structure of SL/SiGe at a

magnification of x100,000 (100k). There are clearly 15 periods with abrupt, sharp interfaces at the top periods. The periods towards the $\text{Si}_{1-x}\text{Ge}_x$ buffer are increasingly smeared. This could be due to the focus of the TEM or could be due to true lack of abruptness of the interfaces. Also, the thicknesses of the dark colored Si layers decrease towards the buffer, while the thicknesses of the light colored $\text{Si}_{1-x}\text{Ge}_x$ layers increase. The periodicity of the SL layers is lost. There are no visible dislocations (see below). Figure 2-6b shows the as-grown structure of SL/Si at a magnification of x50k. There are 16 periods with abrupt interfaces and constant thicknesses. However, Figure 2-6b shows a threading dislocation running from the beginning of the MQW to the surface, across the layers. This is one visible dislocation which is indicative of other threading dislocations throughout the entire structure. It is nearly impossible to get an estimate of the dislocation density from XTEM images. XTEM investigates a very small area of the sample and is therefore statistically unmeaningful for dislocation densities below 10^7 cm^{-2} . Also, in cross-section only half the dislocation is visible due to the direction of the view, so it is impossible to know exactly how many dislocations are present within the thickness of the sample [Iye89]. Therefore, even in cross-section images such as Figures 2-6 and 2-7, where there are no visible dislocations, there can indeed be dislocations present in the structure.

Figure 2-7a shows the cross sectional TEM micrograph of SQW/MBE at a magnification of x100k. The surface is somewhat rough as is the interface

between the substrate and buffer layer. The layers are not particularly straight but are fairly abrupt.

Figure 2-7b shows the micrograph of SQW/VPE at a magnification of $\times 100k$. The interfaces are extremely abrupt and uniform, with no apparent roughness. The thicknesses of the $Si_{1-x}Ge_x$ well layer and Si cap layer are equal to the intended growth thickness, within resolution of TEM (~ 0.2 nm) [Sch90]. No dislocations are visible in this image (see above paragraph).

2.2.3.2 PTEM

The micrograph of SL/SiGe in plan-view is shown in Figure 2-8a. The as-grown SL/SiGe exhibits strain relief through an array of misfit dislocations spaced an average of approximately $0.5\ \mu m$ apart. The micrograph of SL/Si in plan-view is shown in Figure 2-8b. The as-grown SL/Si exhibits strain relief through an array of misfit dislocations spaced an average of approximately $0.35\ \mu m$ apart. In the micrograph shown, there are sample preparation artifacts which represent back-etched dislocations that are wider and less resolved than the unetched dislocations visible as well.

The micrograph of SQW/MBE in plan-view is shown in Figure 2-9a. The as-grown SQW/MBE exhibits strain relief through an array of misfit dislocations spaced an average of approximately $1\ \mu m$ apart. The micrograph of SQW/VPE in plan-view is shown in Figure 2-8b. The as-grown SQW/VPE exhibits strain relief through an array of misfit dislocations spaced from 0.25 to $1.50\ \mu m$ apart. Sample preparation artifacts such as etch pits and back-etched dislocations are present in both micrographs.

2.3 Secondary Ion Mass Spectroscopy

Secondary ion mass spectroscopy (SIMS) is a powerful technique for characterization of concentration profiles in semiconductors. In this technique, a primary ion beam is incident upon the sample and sputters atoms from the surface. Incident ions lose energy through momentum transfer during collisions with atoms in the crystal. The incident ions eventually lose enough energy to come to rest several hundreds of angstroms from the surface of the crystal. These collisions also cause the atoms in the solid to be displaced, some of which escape from the crystal. Most of the ejected atoms are neutral and cannot be detected by normal SIMS, however, a small amount of atoms are ionized above the surface (secondary ions). A plot of the secondary ion yield versus the sputtering time allows quantitative depth profiling. The crater depth after completed analysis is measured and divided by the total sputter time. This gives a sputter rate which can be used to estimate the depth axis. Details of SIMS theory, instrumentation and analysis can be found in several references [Ben87]. The conversion of the secondary ion yield into an impurity concentration is more difficult than depth conversion from sputter rates and is discussed further in section 2.3.1.

Unless otherwise noted all SIMS analysis in this study was done at the University of Florida's Microfabritech Facility using a Perkin Elmer PHI 6600 quadrapole analyzer. Most profiles obtained in this study used O^+ primary

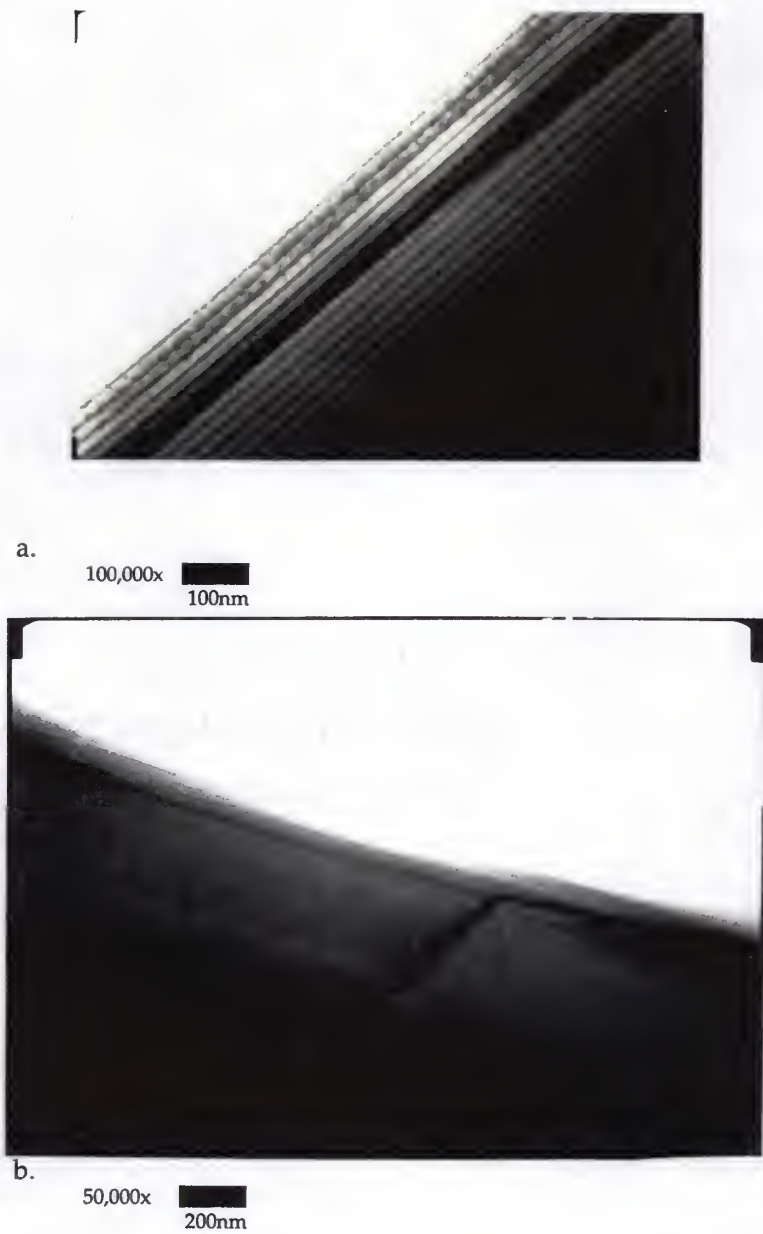
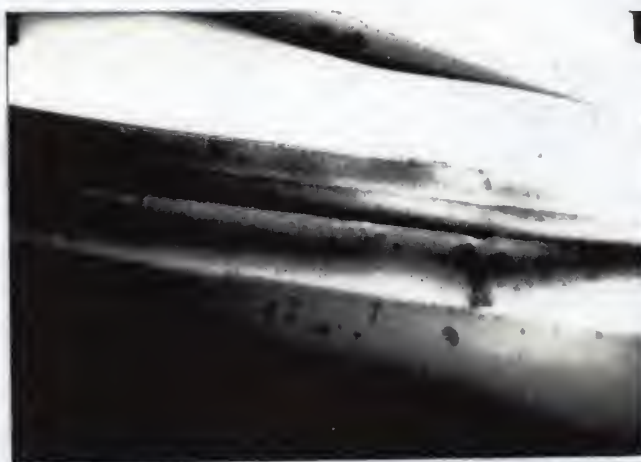



Figure 2-6. Cross sectional view TEM (XTEM) micrographs of as-grown (a) structure SL/SiGe and (b) structure SL/Si.



a.

100,000x  100nm

b.


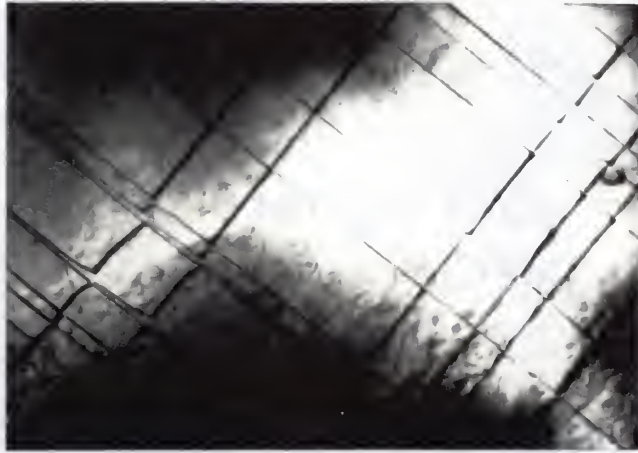
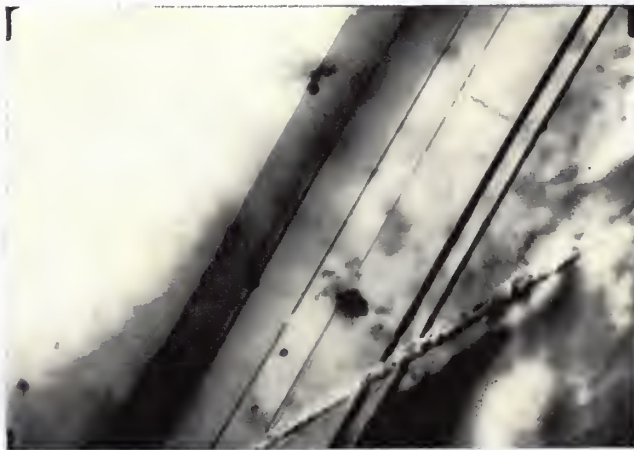
100,000x  100nm

Figure 2-7. XTEM micrographs of as-grown (a) structure SQW/MBE and (b) structure SQW/VPE.



a. 20,000x  500nm




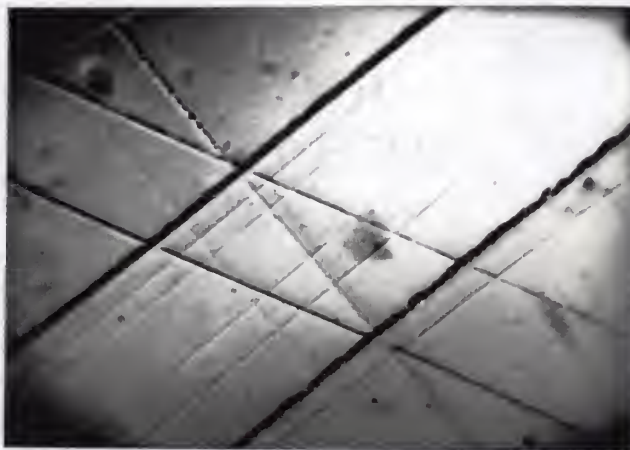
b. 20,000x  500nm

Figure 2-8. Plan view TEM micrograph of as-grown (a) structure SL/SiGe and (b) structure SL/Si.



a. 20,000x 500nm



b. 20,000x 500nm

Figure 2-9. Plan view TEM micrograph of as-grown (a) structure SQW/MBE and (b) structure SQW/VPE.

ions supplied by a dual plasmatron gun. A few profiles used Cs^+ ions generated by a separate cesium gun to detect oxygen and nitrogen content. The crater depths were measured with a Tencor Alpha-Step 500 surface profiler to determine the sputter rate.

2.3.1 Determination of the Ge Depth Profile in SiGe Structures

Determination of the Ge concentration from a count of secondary ions is complex [Pru97a, New97, Kru97]. The overall concentration of Ge in the alloy of the as-grown structures was too high for SIMS calibration with an implanted standard, which is the usual method. The maximum concentration allowable for this method is approximately one percent. A $\text{Si}_{1-x}\text{Ge}_x$ standard cannot be used at high concentrations because of the contradiction of the matrix signals from the Ge in the $\text{Si}_{1-x}\text{Ge}_x$ alloy and the signals from the Ge atoms that have diffused in small quantities into the Si layers. This is commonly known as a matrix effect, in which the secondary ion yield of a particular element varies in different crystal lattices. A linearization technique has been proposed which relates the secondary ion signal of the Ge to the secondary ion signal of the Si [Pru97a, New97]. The linearization is based on the counts from a sample of known Ge concentration using Rutherford Backscattering Spectrometry (RBS). The method applied to the samples used in this work involves the assumption that the amount of Ge present each sample (as grown and annealed) remains constant and then standardizing the Ge dose of the annealed samples to the dose of the structure as grown. Specifically, the Ge concentrations of the

annealed profiles were standardized by (1) assuming a Ge concentration of 15% for the as-grown samples determined from RBS (2) assuming that Ge concentration remains constant within the sample regardless of processing history (3) integrating the area under the as-grown profile curve (4) calculating the ratio of this area to the integrated area under the annealed profile curve and (5) multiplying the concentration of the annealed profile by this ratio. In all cases this proved to be a highly successful concentration standardization technique.

SIMS concentration versus depth analysis of the as-grown structures are shown in Figures 2-10 through 2-13. For the SQW materials it can be seen that the layer thicknesses are close to the requested thicknesses. For structure SQW/VPE (Figure 2-12), the Si cap/ $\text{Si}_{1-x}\text{Ge}_x$ well interface was very abrupt, while the $\text{Si}_{1-x}\text{Ge}_x$ well/Si buffer interface was much less abrupt, almost graded. For structure SQW/MBE (Figure 2-13) neither the cap/well nor the well/buffer interface were abrupt. Both interfaces were graded over approximately $0.03\text{ }\mu\text{m}$. For the SLs, the SIMS profiles verify the layer thicknesses as well as the total number of periods. For both SLs (Figures 2-10 and 2-11), the interfaces were very abrupt. All structures were also analyzed for C and O content, since these impurities can act as traps and greatly alter the diffusion properties of the material. Structures SL/SiGe, SL/Si and SQW/VPE showed very low concentrations of C and O throughout the materials. Structure SQW/MBE, however, showed a high C pileup at the substrate/buffer interface (Figure 2-14).

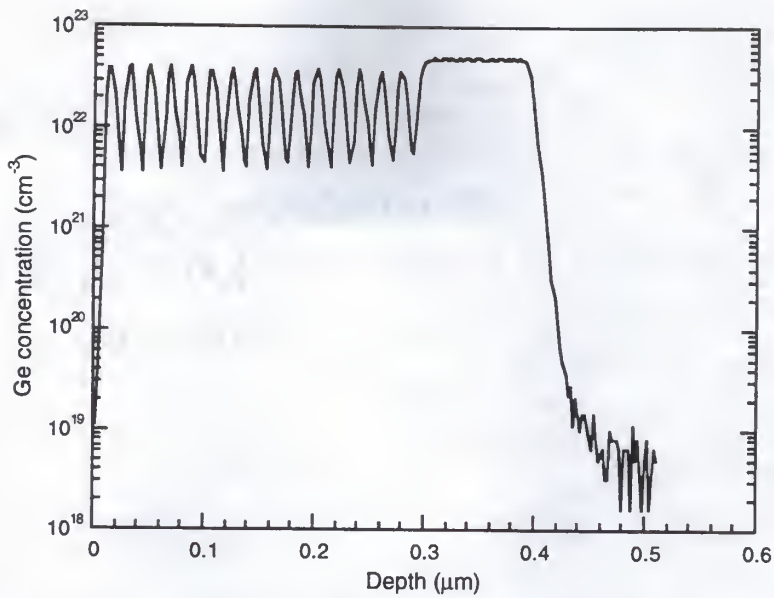


Figure 2-10. Ge concentration profile determined from SIMS for sample structure SL/SiGe.

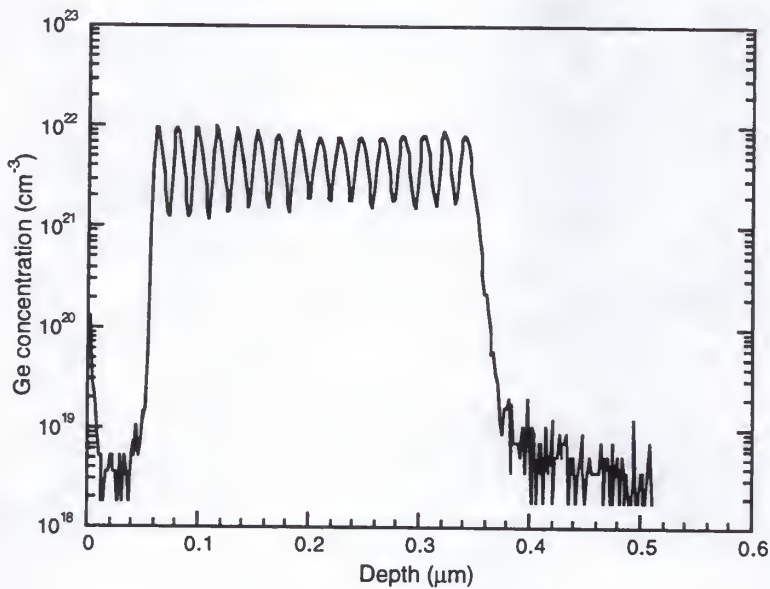


Figure 2-11. Ge concentration profile determined from SIMS for sample structure SL/Si.

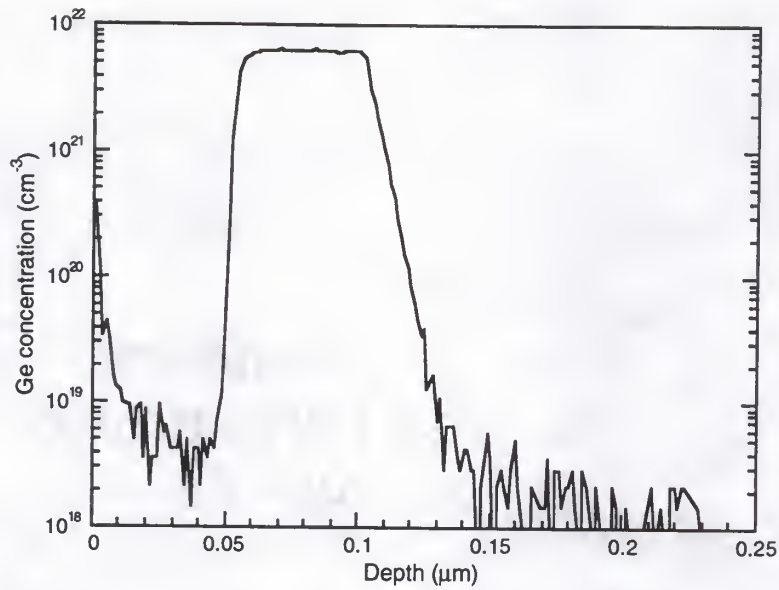


Figure 2-12. Ge concentration profile determined from SIMS for sample structure SQW/VPE.

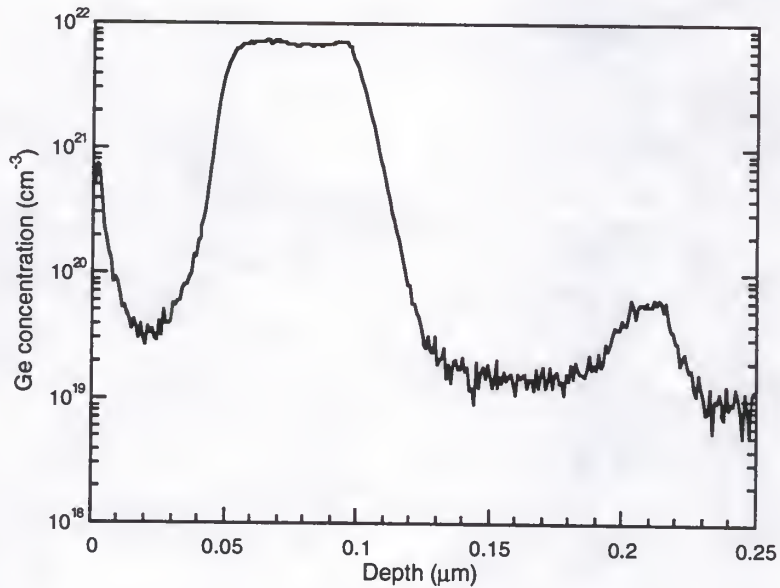


Figure 2-13. Ge concentration profile determined from SIMS for sample structure SQW/MBE.

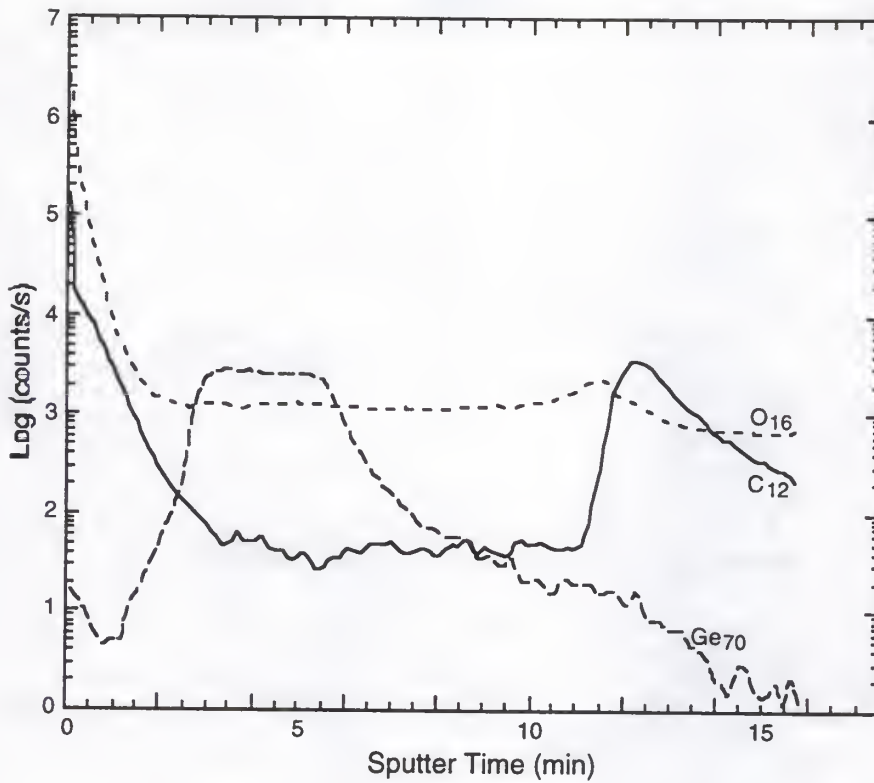


Figure 2-14. SIMS profile of structure SQW/MBE. The concentrations of oxygen and carbon impurities with depth are shown. Both O and C are piled up at the buffer/substrate interface at sputter time ~12 min.

2.3.2 Determination of the Error in D

Throughout this study, SIMS was the primary method used (in conjunction with FLOOPS) to determine interdiffusivity values. It was therefore important to quantify the error involved in SIMS analysis to determine the error incorporated in the extracted D values. There were two sources of error in SIMS profiles: statistical fluctuations from (1) the determined concentrations and (2) the depth scale. The error bars on the extracted diffusivity values were determined from analysis of these errors

using a Monte Carlo simulation approach. The error in the fluctuation of the concentration was determined by examining the fluctuation of the signal in the pure silicon regions of the sample. The error in depth scale was estimated to be 5% [Gos93] and the method of error analysis was taken from H.-J. Gossman *et al.* [Gos93] and is based upon the equations:

$$\tilde{c}_i = c_i + G\sqrt{c_i\gamma} \quad (2-2a)$$

$$\tilde{z}_i = z(1 + G\chi) \quad (2.2b)$$

where c_i is the experimentally determined concentration, z is the experimentally determined depth into the sample, G is a Gaussian distributed random variable with mean $E(G)=0$ and variance $E(G^2)=1$ and γ is the concentration corresponding to a count of 1 in the experimental instrument. The numerically generated concentration and depth into the sample are represented by \tilde{c}_i and \tilde{z}_i , respectively. χ represents one standard deviation in the relative depth scale error and, as stated above, was estimated as 5% for the purposes of this analysis. A new $\tilde{c}_i(\tilde{z}_i, t)$ set was generated using Equations 2-2, creating a profile that was fitted using FLOOPS to determine a new D_i . This was done 11 times and the mean of these values as well as the experimentally determined value was taken as the diffusivity, D , and the standard deviation, $\pm\sigma$, as the error.

2.4 X-ray Diffraction

2.4.1 Overview

X-ray diffraction (XRD) is one of the most powerful and widely used tools in semiconductor characterization [Bau96]. The applications vary from crystal identification to measuring the quality of crystal growth. XRD is based on Bragg's Law:

$$2d \sin \theta_B = n\lambda \quad (2-3)$$

An x-ray beam of wavelength λ is incident upon a crystal at an angle θ_B , the Bragg angle. A diffracted beam composed of a large number of scattered rays mutually reinforcing one another is reflected from the atom planes. By using x-rays of known wavelength and measuring the Bragg angle one can determine the spacing, d , of the planes of the crystal.

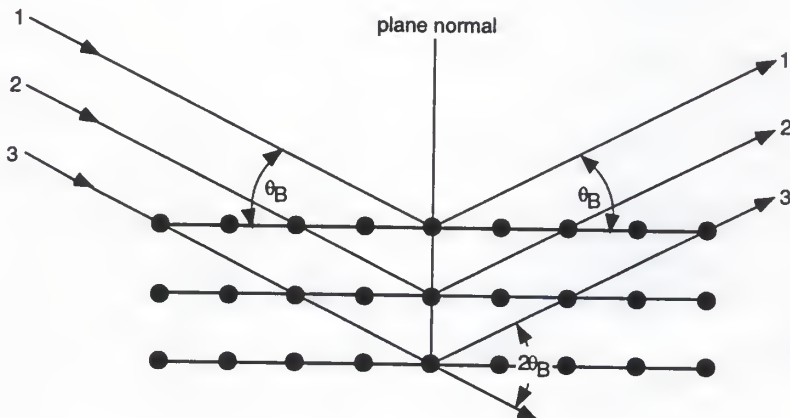


Figure 2-15. Schematic of symmetric x-ray Bragg reflection [Cul78].

All scans were taken using a Phillips high resolution XRG 3100 five crystal diffractometer. This instrument consists of four main parts: an x-ray source, a monochromator, a goniometer and a detector. This system setup has been previously described in detail by Krishnamoorthy [Kri95] and will be summarized here.

A generator operating at 40kV and 40mA creates electrons at a cathode. These electrons are accelerated through a field and bombard a Cu target anode emitting $\text{CuK}_{\alpha 1}$ x-ray radiation with broad angular and wavelength ranges. The x-ray beam is monochromatized and collimated prior to impingement upon the sample using a four crystal Bartels monochromator/collimator setup shown in Figure 2-16. The x-ray beam, upon leaving the monochromator/collimator, impinges on the sample crystal which is mounted on the stage of the goniometer. The goniometer controls the x, y, z, tilt (ψ) and rotation (ϕ) positions of the sample.

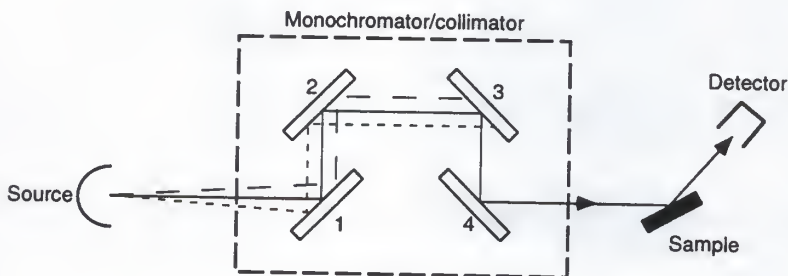


Figure 2-16. Schematic of the monochromator/collimator. X-rays impinge the first crystal and are subsequently collimated and monochromated by crystals 2 through 4, after which they impinge on the sample.

The angle between the incident beam and the projected diffracted beam which reaches the detector is defined as 2θ , and is controlled by the goniometer. The angle between the incident beam and the sample surface is defined as ω , which is also controlled by the goniometer. Rocking curve scans occur through the independent movement of both the 2θ and ω angles. The two scans utilized in this work are the ω scan and the $\omega/2\theta$ scan. In the ω scan, the detector (2θ) is stationary while the sample is rocked over a specified ω range. The 2θ value is fixed to satisfy Bragg's law so that at a certain value of ω an x-ray peak is observed. In the $\omega/2\theta$ scan both a 2θ range and an ω range are designated. The detector is rotated through the 2θ range twice as fast (but in the same direction) as the sample is rotated through the ω range; the angle between the incident beam and the sample surface changes. This scan is most useful when the sample crystal is composed of more than one material (i.e. Si and $\text{Si}_{1-x}\text{Ge}_x$) and the Bragg conditions of only one material are known (Si).

When the x-ray beam reflected from the sample crystal is directed immediately into a detector, as shown in Figure 2-16, it is considered to be a double axis spectrometer. This double axis mode was employed in both ω and $\omega/2\theta$ scans in this study. In a triple axis spectrometer (Figure 2-17), the x-ray beam reflected from the sample is directed towards a two-crystal analyzer before entering a detector. This offers improved angular resolution and

intensity, which allows observation of weak diffraction satellite peaks from thin superlattice layers. Triple axis mode was employed in 2θ scans in this study to identify the Bragg angle in weak reflections from the $\text{Si}/\text{Si}_{1-x}\text{Ge}_x$ superlattice layers.

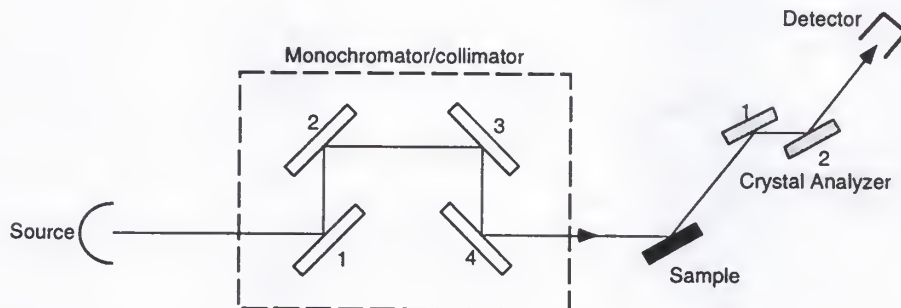


Figure 2-17. Schematic of the x-ray path used in triple axis mode. The x-rays are directed to a double crystal analyzer after impinging on the sample and before heading to the detector.

X-ray rocking curves were taken of the superlattice structures SL/SiGe and SL/Si as grown using the methods just described (Figure 2-18 and 2-19). Distinct satellite peaks, of both positive and negative order, can be seen for each structure, surrounding the high intensity Si substrate peak at $\omega \approx 34.5^\circ$. The first satellite peak to the left of the substrate peak is considered the 0th order peak and denotes the average composition of the $\text{Si}_{1-x}\text{Ge}_x/\text{Si}$ layers. The 1st order peak to the left of the 0th order peak is the first peak that represents the periodicity of the $\text{Si}/\text{Si}_{1-x}\text{Ge}_x$ SL layers. This is the peak used in this work to extract diffusivities from HRXRD scans (Section 2.4.3). In each scan,

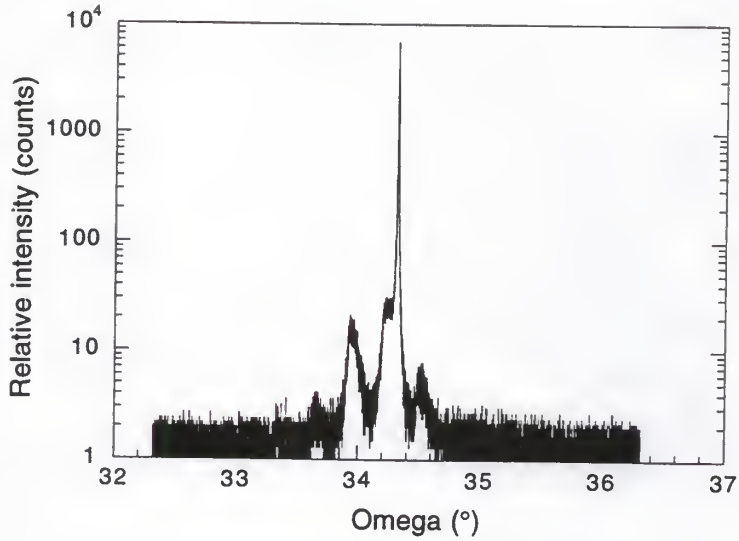


Figure 2-18. X-ray rocking curve of structure SL/SiGe before anneal.

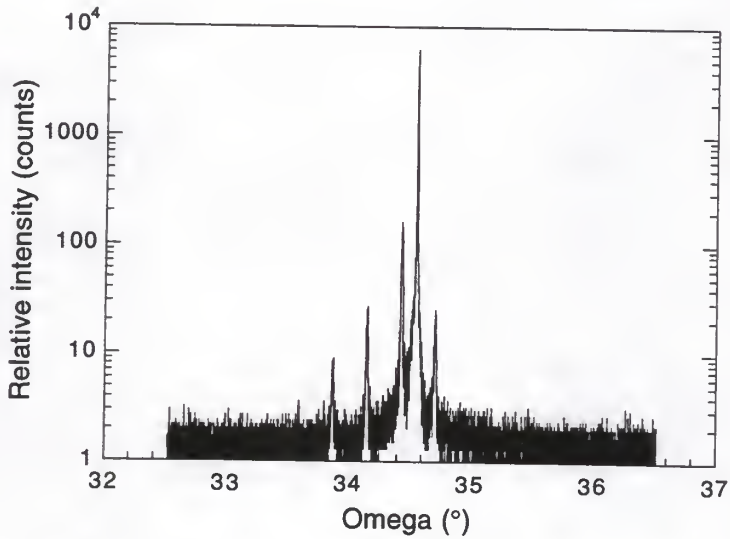


Figure 2-19. X-ray rocking curve of structure SL/Si before anneal.

satellite peaks up to the +3rd order can be seen, while only the -1st order peak can be observed to the left of the Si substrate peak.

The x-ray rocking curve of structure SL/SiGe shows broad satellite peaks, indicating that the periodicity of the SL layers is imprecise. XTEM images of the layers indeed show that the layer widths slightly decrease nearer to the $\text{Si}_{1-x}\text{Ge}_x$ buffer layer. The x-ray rocking curve of structure SL/Si shows very sharp satellite peaks confirming that the periodicity of the SL layers is consistent throughout the structure.

2.4.2 Optimization Procedures

Typically, substrates used for growth are intentionally miscut; a silicon (100) substrate can be miscut 1 to 5° off the (100) plane towards the nearest (110) plane (Figure 2-20). This causes the characteristic substrate x-ray peak position to differ from its real value ($\omega=\theta$). A epitaxial layer can also be misoriented with respect to both the intended substrate growth direction as well as the miscut substrate surface normal direction (Figure 2-20).

To obtain the true ω values for both the substrate and epilayer, optimization procedures involving ω , the sample crystal rotation angle, ϕ , and crystal tilt, ϕ , were performed [Kri95]. These procedures are extremely important when trying to identify and measure satellite peaks for thin superlattice layers, as the satellite peaks tend to decay very rapidly with increasing $\Delta\omega$ (Figure 4-4 and 5-4). Even more intensity decay of the satellite peaks is observed after annealing the sample crystal at high temperature.

Optimizing intensity of the silicon substrate Bragg signal allows the smaller decayed satellite peaks to be more easily observed and measured.

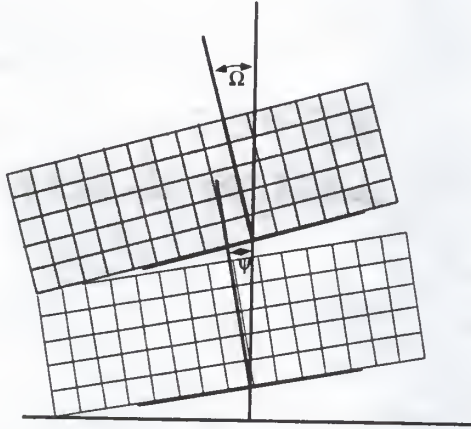


Figure 2-20. Miscut of substrate and mistilt of epilayer. The lower unshaded region shows the possible miscut of the substrate, ψ . The top shaded region shows the additional possible mistilt of epilayer grown on substrate, Ω .

X-ray diffraction peak positions discussed hereafter are assumed to represent optimized values unless otherwise stated.

2.4.3 Determination of Interdiffusivity of Superlattice Layers

The periodicity of a superlattice structure causes a similar effect in XRD as the periodicity of the planes of lattice atoms. The diffraction of the superlattice is modulated and results in well-defined satellite peaks. The superlattice period can be obtained from [Pel91]:

$$\frac{2 \sin \theta_n - 2 \sin \theta_{SL}}{\lambda} = \pm \frac{n}{\Lambda} \quad (2-4)$$

where n is the order of the satellite peak of interest, θ_n is Bragg angle of the n th order satellite peak, θ_{SL} is the Bragg angle of the satellite peak of interest, λ is the wavelength of x-ray used, and Λ is superlattice period.

Through HRXRD the value of D will be calculated from the measured decay of the intensity of the first satellite peak about the substrate as a function of annealing time and resulting interdiffusion. The substrate peak from the (004) reflection remains the same regardless of processing history. The 0th order satellite peak represents the spacing of the lattice of the *average* composition of the total of the deposited layers. The 1st order satellite peak represents the periodicity of the SL layers, which changes significantly and quickly upon annealing, therefore it is the satellite peak of interest. The decay in the intensity, I , of the first order satellite x-ray peak after a long time anneal, is directly related to the interdiffusion coefficient by:

$$\frac{d}{dt} \ln \left(\frac{I}{I_0} \right) = \frac{-8\pi^2}{\lambda^2} D \quad (2-5)$$

where λ is the SL period (cm) and I_0 is the initial satellite x-ray peak intensity before annealing [Bar90, Pro90]. By plotting $\ln(I/I_0)$ versus time, one can determine D for different temperatures. Then, by plotting $\ln(D)$ versus $1/T$, for multiple temperatures, an Arrhenius expression for diffusion can be obtained.

2.4.4 Determination of Strain Relaxation

X-ray double crystal diffractometry allows the accurate determination of the orientation, size and shape of the deformed unit cell of the layer compared to the cubic unit cell of the Si or $\text{Si}_{1-x}\text{Ge}_x$ substrate or buffer. The amount of strain between layer and substrate can be determined through analysis of their respective ω peak positions. When the $\text{Si}_{1-x}\text{Ge}_x$ layer of larger lattice parameter, a_l , is deposited on the Si substrate of smaller lattice parameter, a_s , the cubic cell of the $\text{Si}_{1-x}\text{Ge}_x$ lattice must be compressed in the parallel direction so that the lattice parameter matches that of the Si lattice, $a_{//}$. The volume of the $\text{Si}_{1-x}\text{Ge}_x$ cubic cell, however, is constant to a good approximation, so the compression in the parallel direction is accommodated by an increase in the perpendicular lattice parameter, a_{\perp} . The $\text{Si}_{1-x}\text{Ge}_x$ cell is no longer cubic, but tetragonal and the strain introduced is known as tetragonal strain (Section 1.2).

The angular separation between the substrate and epilayer peaks for the symmetric reflection (the angle of incidence equals the angle of reflection, i.e., the sample surface is oriented in the same direction as the reflection plane) can be used to determine the perpendicular lattice mismatch between the epilayer and substrate [Kri95]:

$$\left(\frac{a_l - a_s}{a_s} \right)_{\perp} = -(\theta_l - \theta_s) \cot \theta_s \quad (2-6)$$

To *completely* define the epilayer strain state, however, both the perpendicular and parallel lattice mismatch must be determined. This can be done through HRXRD rocking curves from asymmetric lattice planes making an angle ϕ with the surface (Figure 2-21). This method is described in detail in [Bar78, Kri95] and has been used in this investigation to determine the strain relaxation of sample structures SL/SiGe and SL/Si after thermal treatment (Sections 4.5.3 and 5.5.3). Briefly, the Bragg condition for an asymmetric plane is satisfied at two different ω angles:

$$\omega_1 = \theta + \phi \quad (2-7a)$$

$$\omega_2 = \theta - \phi \quad (2-7b)$$

The values of ω_1 and ω_2 for both the epilayer and substrate are obtained through asymmetric rocking curve scans, and Equations 2-7 are solved simultaneously for the values of θ and ϕ for both the epilayer and substrate.

These values are used in:

$$\left(\frac{a_l - a_s}{a_s} \right)_{\perp} = (\phi_l - \phi_s) \tan \phi_s - (\theta_l - \theta_s) \cot \theta_s \quad (2-8a)$$

$$\left(\frac{a_l - a_s}{a_s} \right)_{//} = -(\phi_l - \phi_s) \cot \phi_s - (\theta_l - \theta_s) \cot \theta_s \quad (2-8b)$$

to determine the perpendicular and parallel lattice mismatches.

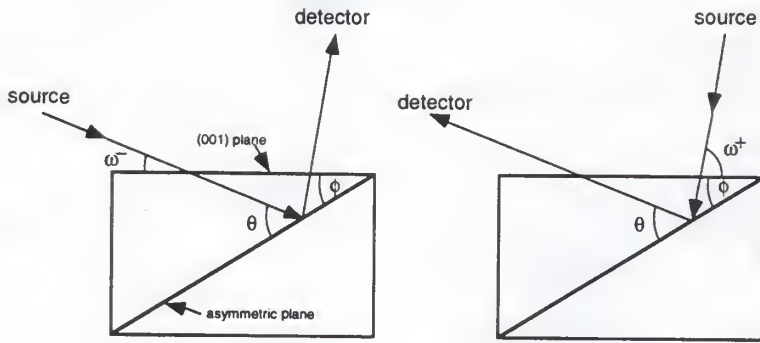


Figure 2-21. Example of positive and negative x-ray diffraction from an asymmetric plane. ω , θ and ϕ are identified. For a symmetric reflection, the diffraction plane would be parallel to the sample surface, $\omega=\theta$.

CHAPTER 3

BEHAVIOR OF ANNEALED $\text{Si}_{1-x}\text{Ge}_x$ SINGLE QUANTUM WELLS

One of the fastest growing applications for $\text{Si}_{1-x}\text{Ge}_x$ material is heterojunction bipolar transistor (HBT) technology (Section 1.1.2). HBTs use doped $\text{Si}_{1-x}\text{Ge}_x$ as the base and surrounding Si layers as the emitter and collector regions. A $\text{Si}_{1-x}\text{Ge}_x$ base region allows greater doping than Si without reducing emitter injection efficiency [Gha95]. Out-diffusion, however, from the base of both the Ge and dopant during growth and processing forms parasitic barriers at the heterojunctions, which severely degrades device performance. Also, base widths are currently slightly greater than the critical layer thickness [Gru97, Heu96, deB97], which introduces possible $\text{Si}_{1-x}\text{Ge}_x$ layer relaxation through formation of dislocations. It is therefore important to $\text{Si}_{1-x}\text{Ge}_x$ HBT technology to be able to predict the interdiffusion behavior and dislocation effects of $\text{Si}/\text{Si}_{1-x}\text{Ge}_x/\text{Si}$ single quantum well (SQW) structures.

Interdiffusion of $\text{Si}/\text{Si}_{0.85}\text{Ge}_{0.15}/\text{Si}$ SQW material in inert, oxidizing, and nitriding ambients over a temperature range 900 to 1200 °C has been investigated. Thermal processing in all three ambients over the same temperature range allowed estimation of the enhancement factor of interdiffusion of $\text{Si}/\text{Si}_{0.85}\text{Ge}_{0.15}/\text{Si}$ material under interstitial and vacancy supersaturation as well as under inert (equilibrium defect concentration) conditions. An estimate of the fractional contribution of interstitial and

vacancy mechanisms to interdiffusion in $\text{Si}_{0.85}\text{Ge}_{0.15}/\text{Si}$ SQWs was been made by comparing SIMS profiles of annealed samples to profiles calculated by FLOOPS diffusion simulations. Investigation of a $\text{Si}/\text{Si}_{1-x}\text{Ge}_x/\text{Si}$ structure with a buried boron (B) marker layer in the Si buffer region has addressed the impact of dislocated $\text{Si}_{1-x}\text{Ge}_x$ layers on interdiffusion (Section 3.4.2).

3.1 Growth Parameters and Structure

A SQW test structure (SQW/MBE) was grown by Molecular Beam Epitaxy (MBE) at a temperature of 520 °C. As shown in Figure 3-1, the structure consisted of a lightly p-doped (100) Si substrate with an undoped 100 nm Si buffer layer, followed by an undoped 50 nm $\text{Si}_{0.85}\text{Ge}_{0.15}$ layer and an undoped 50 nm Si cap.

Another SQW test structure (SQW/VPE) was grown using an ASM Epsilon 1 vapor phase epitaxy reactor at a temperature of 700 °C. The structure consisted of a lightly p-doped (100) Si substrate with an undoped 100 nm Si buffer, followed by an undoped 50 nm $\text{Si}_{0.85}\text{Ge}_{0.15}$ layer and an undoped 50 nm Si cap. Structures SQW/MBE and SQW/VPE nominally differ only by their growth method. The $\text{Si}_{0.85}\text{Ge}_{0.15}$ layer in SQW/VPE was grown using SiCl_2H_2 (dichlorosilane), GeH_4 (germane), and hydrogen (H_2) as the carrier gas. The silicon layers were grown at a rate of 5.0 nm/min while the $\text{Si}_{0.85}\text{Ge}_{0.15}$ layer was grown at a rate of 18.8 nm/min. The Ge concentrations of the $\text{Si}_{1-x}\text{Ge}_x$ layers for both structures were verified by Rutherford Backscattering Spectroscopy (RBS) and the layer thicknesses were verified by cross-sectional Transmission Electron Microscopy (XTEM).

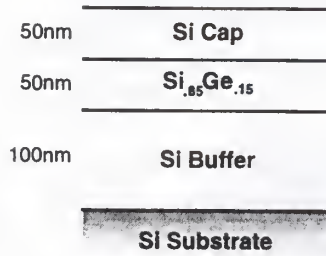


Figure 3-1. Schematic of sample structures SQW/MBE and SQW/VPE.

The Ge depth versus concentration profiles for as-grown and annealed samples were determined by Secondary Ion Mass Spectroscopy (SIMS) using a Perkin Elmer PHI 6600 quadrupole analyzer with a 6 kV oxygen beam. The profile depth scales were determined from Tencor Alpha-Step 500 surface profiler measurements of the SIMS sputtered craters. All concentrations and depths profiles were standardized using the method described in Section 2.3.1.

3.2 Processing

3.2.1 Rapid Thermal Processing

Samples annealed at high temperatures and short times (less than approximately five minutes) in Ar, O₂ or NH₃ were processed in a rapid thermal processor (RTP). The traditional furnace anneal is inappropriate for short time, high temperature anneals because of increased impurity concentrations in the ambient as well as larger temperature nonuniformities due to the nonequilibrium state of the sample. Also, the high diffusivities of some species require short anneal times for controlled, measurable diffusion lengths. During high temperature heating the radiative heat transfer

component exceeds those of convection and conduction. RTP uses this energy transfer between the radiant heat source and an object to process sample material [Sin88]. Because of the optical nature of the radiative energy transfer, the reactor wall is not in thermal equilibrium with the sample [Tim97].

An AG Associates Heatpulse 2101 was used for all RTP anneals. The Heatpulse 2101 uses an array of line source tungsten-halogen lamps to achieve isothermal heating, with banks of twelve lamps both above and below the heating chamber. The chamber and wafer holder are both made of quartz, which transmits the entire spectrum emitted by the lamps (middle infrared, 3 to 6 μm). This causes the chamber and holder to remain at a temperature far below the sample temperature. The chamber is considered to be a warm wall chamber, surrounded by a reflective water- and air-cooled metal housing, and can reach temperatures of $\sim 400^\circ\text{C}$ [Roo93].

The Heatpulse 2101 controls the temperature of the wafer through the use of an IRCON optical pyrometer and closed loop feedback software. The pyrometer measures the emissivity from the sample and converts the emissivity value to a temperature value. Based on this temperature feedback, the RTP then adjusts the lamp power to maintain the desired temperature. Optical pyrometry is noninvasive and fast, yet is sensitive to emissivity changes during processing (from wafer warping, film growth, backside roughness, etc.). The pyrometer must be carefully calibrated. The most robust method of calibration involves concurrent thermocouple use. At high

temperature (1000 to 1200 °C), however, the measurement of oxide thickness is a very reliable approach to calibrating surface temperature. At lower temperatures (600 to 1000 °C) activation of dopant implants is often used [Roo93].

The RTP temperature for these investigations was initially calibrated through oxide measurements [Mos85, Gon94]. Temperature uniformity across the wafer is a main concern during RTP. The edge temperature can often be lower than the center temperature, with an overall wafer temperature non-uniformity of as much as $\pm 20^\circ\text{C}$ [Pet91]. To determine the extent of temperature uniformity across the silicon wafer, the wafer was processed in the RTP in flowing dry O_2 ambient at processing times and temperatures similar to those used to process the $\text{Si}_{1-x}\text{Ge}_x/\text{Si}$ structures. The resulting oxide film was characterized using an ellipsometer to measure thickness at five points across the wafer. Film thickness was found to be the same across the wafer, within the error of ellipsometer measurement ($\pm 1 \text{ nm}$ [Sch90]). This indicates that the uniformity across a four inch wafer is within the error of temperature measurement, $\pm 10^\circ\text{C}$.

To more accurately determine the RTP calibration, a thermocouple wafer was also used to calibrate the pyrometer. A W5%Re/W26%Re (Type C) thermocouple was embedded in a Si wafer using e-beam welding [Hoy88]. The reading of this thermocouple was compared to the pyrometer output at temperatures from 800 to 1200 °C at 50 degree intervals. At each temperature,

the emissivity dial was adjusted so that the pyrometer reading equaled the thermocouple reading.

The Heatpulse 2101 has a quartz wafer tray inside the chamber which holds 4" wafers only, therefore the small 1×1 cm samples had to be placed on top of a 4" silicon "dummy" wafer. This raised questions regarding the heat transfer between the wafer and the sample, as well as the heat transfer between the sample and the lamps. To determine experimentally the impact this had on the temperature of the sample compared to the underlying wafer, a stack of three rectangular samples of decreasing area was oxidized on a dummy wafer and the oxide thickness on the exposed area of each was measured. Within the error of the ellipsometer (± 1 nm) [Sch90], there was no difference in the oxide thickness on any of the three samples or the wafer and therefore the heat transfer can be considered to be thorough (± 10 °C [Gon94]).

Before annealing, the test wafer was cut into 1×1 cm pieces which were cleaned using a regimen of deionized water, $\text{H}_2\text{SO}_4\text{:H}_2\text{O}_2$ (1:2) and $\text{H}_2\text{O:HF}$ (10:1), and then dried with N_2 . Samples were rapid thermal processed with all ambient gases (Ar , O_2 , NH_3) flowing at 1.5 slm.

3.2.2 Furnace Processing

Samples annealed for longer than five minutes in either N_2 or O_2 were processed in a Thermco furnace. Furnace anneal at times longer than approximately 5 minutes allows greater temperature control. During furnace anneal the compartment is heated to anneal temperature before the sample is

placed in the oven. When the sample is placed in the oven, it heats rapidly to be in thermal equilibrium with the entire furnace environment. The furnace was not equipped with NH_3 gas, therefore samples were not furnace annealed in nitriding ambient.

$\text{Si}_{1-x}\text{Ge}_x$ test pieces underwent preparations identical to those for RTP (Section 3.2.1). Since Ar and N_2 have similar thermal conductivities the thermal profiles of samples processed in these gases are expected to be similar. The diffusion profiles of the samples processed in the RTP using Ar and the samples processed in the furnace using N_2 can therefore be accurately compared.

3.3 Simulation of Diffusion

The diffused Ge profiles were analyzed using the FLorida Object Oriented Process Simulator (FLOOPS) [Law96]. This is a computer simulation program which predicts the diffusion profile of a semiconductor material after preprocessing and processing steps such as ion implantation, oxide growth, annealing, and etching. A grid is defined for a region of interest and modified versions of Fick's law are numerically solved within this grid. The fineness of the grid determines the resolution of the profile as well as the computation time of the simulation. After processing, the dopant, defect or interface diffusion profiles can be plotted as concentration versus depth.

Three different diffusion models are available in FLOOPS: the Neutral, Fermi, and Pair models. In the Neutral model, Fick's law is solved in the form:

$$\frac{\partial C}{\partial t} = \nabla D \nabla C + \sum E_{\text{field}} \quad (3-1)$$

with the diffusivity of the dopant, D , given as:

$$D = D_N = D_o \exp\left(\frac{-E_a}{kT}\right) \quad (3-2)$$

where C is the concentration of dopant atoms (cm^{-3}), t is time (min), and E_{field} is the electric field (V/cm). D_N denotes the diffusivity of the neutral (uncharged) dopant atom (cm^2/s), D_o is a pre-exponential constant (cm^2/s), E_a is the activation energy (eV) and k is the Boltzmann constant (8.62×10^{-5} eV/K).

In the Fermi model, Fick's law is solved in the same form as equation 3-1, but the diffusivity is given as:

$$D = D_o + D_+ \left(\frac{p}{n_i}\right) + D_- \left(\frac{n}{n_i}\right) + D_{++} \left(\frac{p}{n_i}\right)^2 + D_{--} \left(\frac{n}{n_i}\right)^2 + \dots \quad (3-3)$$

where D_o is the diffusivity of the dopant in its neutral state, D_+ and D_- are the diffusivities of the dopant in its singly positively and negatively charged states respectively, D_{++} and D_{--} are the diffusivities of the dopant in its doubly positively and negatively charged states, respectively, p and n are the hole and electron densities, respectively, and n_i is the intrinsic carrier concentration. The ionized dopant diffusivities are expressed in an Arrhenius form after equation 3-2.

The Pair model uses Fick's law in the form:

$$\frac{\partial C}{\partial t} = \sum \nabla D_{AX} C_{A^+} \frac{C_X}{C_X^*} \nabla \log \left(C_{A^+} \frac{C_X}{C_X^*} \frac{n}{n_i} \right) \quad (3-4)$$

where X designates either interstitial or vacancy point defects, D_{AX} denotes the diffusivity of the dopant occurring through either vacancies or interstitials, C_{A^+} is the concentration of dopant in its ionized state, C_X is the actual point defect concentration of either interstitials or vacancies, and C_X^* is the equilibrium point defect concentration. The $\log(n/n_i)$ term accounts for the contribution of the electric field to any concentration change. Equations 3-3 and 3-4 would be written for acceptors by inverting the n/n_i term. The total diffusivity of the dopant is defined as:

$$\frac{D}{D^*} = f_I \frac{C_I}{C_I^*} + f_V \frac{C_V}{C_V^*} \quad (3-5)$$

where f_I and f_V are the fraction of diffusion which occurs via interstitials and vacancies, respectively, and D^* is the diffusivity under inert ambient.

The Neutral model assumes that the dopant diffuses in its neutral charge state only, and does not include contributions to the diffusivity from point defects. The Fermi model accounts for all possible charge states of the diffusing dopant atom, known as Fermi-level effects, but still does not include contributions to the diffusivity from point defects. The only difference between the Neutral and Fermi models is that the Neutral model uses only the first term of Equation 3-3. The Pair model includes the contributions to the diffusivity of any point defects present. The C_I^* and C_V^* expressions are a function of the Fermi level, which is the electron

electrochemical potential. The Fermi level therefore changes as the electron concentration changes. Fermi level effects due to all charge states of the dopant are still accounted for through the D^* parameter which is described by equation 3-3.

In this study the Fermi model was used to determine the diffusivity under inert conditions as well as the diffusivity occurring during vacancy and interstitial supersaturation. In the case of Ge atoms in a Si lattice, the Ge is neutral (uncharged) within the Si lattice, so there are no dopant Fermi-level effects and therefore the Fermi model and Neutral model are equivalent in this case. Any electric field effects were ignored in the initial attempts to model the system. There were two reasons for this: (1) Fermi level effects of ionized defects were assumed to be orders of magnitude smaller than dopant concentrations-too small to contribute to an electric field and (2) the substitutional dopant atom (Ge) is neutral within the host lattice (Si).

The Pair model was used to determine the fractional interstitial and vacancy components, f_i and f_v . The diffusivity under inert conditions, previously determined from the Fermi model, was used as the value for D^* . The inert diffusivity was proportioned into interstitial and vacancy components such that:

$$D^* = D_i^* + D_v^* \quad (3-6)$$

so that the parameter f_i could be defined such that:

$$f_i = \frac{D_i^*}{D_i^* + D_v^*} \quad \text{with } f_v = 1 - f_i \quad (3-7)$$

At a given temperature f_i remains the same under any ambient and is not dependent upon point defect supersaturation.

Values of C_i/C_i^* and C_v/C_v^* for each temperature under either oxidizing or nitriding ambients were extracted from diffusion data reported in literature. By assuming phosphorous to have an $f_i=1$, phosphorous diffusion data was fit to extract C_i/C_i^* and C_v/C_v^* values under oxidizing conditions. Similarly, by assuming antimony to have an $f_i=0$, Sb diffusion data was fit to extract C_i/C_i^* and C_v/C_v^* values under nitriding conditions. The previous assumptions regarding f_i are broadly accepted in the Si diffusion community [Fah89a, Hu94]. Equation 3-4 was then solved for the concentration of the dopant, using the value of D calculated from Equation 3-5. The resulting profile was compared to the experimental profile, and the ratio of D_i^* and D_v^* , hence f_i , was adjusted until the profiles matched as judged by a Gaussian fit. At this point a good estimate of f_i was made. It is important to note here, as in Section 1.4, that f_i values extracted for Ge diffusion employed the C_i/C_i^* and C_v/C_v^* values from fitting the phosphorous and antimony diffusion data.

The approach used in all FLOOPS simulations in this dissertation was to model the $\text{Si}_{1-x}\text{Ge}_x$ alloy regions as Ge dopant in the Si lattice. In this case, there are five system species: a Si substitutional (Si_s), a Ge substitutional (Ge_s), a Si interstitial (I_{Si}), a Ge interstitial (I_{Ge}), and a lattice vacancy (V). Because there are five species, five equations are needed to completely describe the

system. Ideally, these five equations can be obtained through a continuity equation for each component, in the form of either equation 3-1 or 3-3. There is also an equation for conservation of lattice sites which allows us to eliminate one of the five continuity equations. Because Si_s is the most abundant species, computationally it will be the most difficult for which to account, so Si_s would most logically be chosen to be replaced by the conservation of lattice site equation. Ultimately, the system could be completely described by four continuity equations (Ge_s , I_{Ge} , I_{Si} , and V) and one equation for conservation of Si lattice sites.

The actual FLOOPS model employs several assumptions which simplify the above model. It is first assumed that since Ge is treated as a dopant in the Si lattice, Ge on substitutional sites may be ignored when added to Si substitutionals; the Ge_s concentration is negligible when compared to the Si_s concentration. This assumption also allows the equation for conservation of lattice sites to be ignored. It is further assumed that the concentration of mobile Ge is much lower than the concentration of substitutional (immobile) Ge. Mobile Ge may occur as Ge-V complexes or uncomplexed Ge diffusing substitutionally through adjacent vacancies (accounted for through D_v or D_v^*), or as Ge-I complexes or uncomplexed interstitial Ge atoms (accounted for through D_i or D_i^*). This allows one equation describing mobile and immobile Ge to be written, in which the expression of interest is the ratio of the two. This ratio of mobile to immobile Ge concentrations was calculated by assuming local equilibrium between the

two species. Ultimately, FLOOPS used expressions for interstitial and vacancy concentrations as well as total Ge concentration to solve the diffusion equations and provide a final depth versus concentration profile.

The as grown Ge profiles for each structure, determined from SIMS, were used as the initial profile for the FLOOPS diffusion simulations. The value of the diffusivity was taken to be a function of temperature only, ignoring possible concentration and stress dependencies. Diffusion was simulated for one dimension (1D) only, in the direction perpendicular to the sample surface. As stated previously, electric field effects were ignored. Appendix A gives examples of FLOOPS codes used to simulate 1D diffusion with the Fermi model and Pair model.

3.4 Results

3.4.1 Diffusivities and Activation Energies from SIMS/FLOOPS

The SIMS profiles of the annealed samples were standardized using the method described in Section 2.3.1. The Ge concentrations of the annealed profiles were standardized with respect to the total Ge concentration of the as-grown profile. The depth scale of the SQW/MBE was standardized by aligning the segregation peak of the annealed and as-grown profiles. This SIMS profile peak was unique to the SQW/MBE material. The depth scale of the SQW/VPE profiles was standardized by aligning the bisectors of the full width at half maximum sector of the Ge well. In each case, the depth scale of annealed samples was shifted no more than 20 nm in one direction. This

lateral movement is well within one standard deviation, estimated at 0.05, in relative depth scale error of SIMS [Gos93].

The extracted diffusivity values for structure SQW/MBE annealed in inert, oxidizing, and nitriding ambients are given in Table 3-1. The value of the diffusivity and enhancement in oxidizing ambient for anneal temperature 900 °C and time 2206 min could not be extracted because the 50nm Si cap had been consumed by the oxide and oxidation of the $\text{Si}_{1-x}\text{Ge}_x$ layer had occurred. Diffusivity and enhancement values for diffusion in nitriding ambient at 900 and 1000 °C in a furnace were not investigated; only the RTA was equipped with ammonia gas. It is important to note here that all extracted diffusivities discussed in Chapters 3 through 5 are *effective diffusivities*, $D_{\text{Ge}}^{\text{eff}}$, and are only referred to as *diffusivities* for textual convenience.

The values of the diffusivities for structure SQW/MBE as a function of temperature in inert, oxidizing, and nitriding ambients are shown in Figure 3-2. Error analysis of the diffusion coefficients was performed using the method described in Section 2.3.2. Fitting this data to Arrhenius expressions results in the following equations when the interdiffusion is carried out in inert, oxidizing, and nitriding ambients:

$$D_{\text{Ge}}^{\text{Inert}}(\text{SQW / MBE}) = 1.6 \times 10^8 \exp(-5.87\text{eV} \pm 0.14 / \text{kT}) \text{ cm}^2/\text{s} \quad (3-8)$$

$$D_{\text{Ge}}^{\text{Ox}}(\text{SQW / MBE}) = 6.1 \times 10^5 \exp(-5.27\text{eV} \pm 0.11 / \text{kT}) \text{ cm}^2/\text{s} \quad (3-9)$$

$$D_{\text{Ge}}^{\text{Nit}}(\text{SQW / MBE}) = 1.1 \times 10^2 \exp(-3.27\text{eV} \pm 0.10 / \text{kT}) \text{ cm}^2/\text{s} \quad (3-10)$$

This is the first time that activation energies for interdiffusion of $\text{Si}_{1-x}\text{Ge}_x/\text{Si}$ layers under interstitial injection and vacancy injection have been directly determined from experiment. The activation energy in nitriding ambient is provided for comparison purposes only, and is not statistically reliable because it was extracted from only two data points. This statement also applies to Equation 3-13 for SQW/VPE.

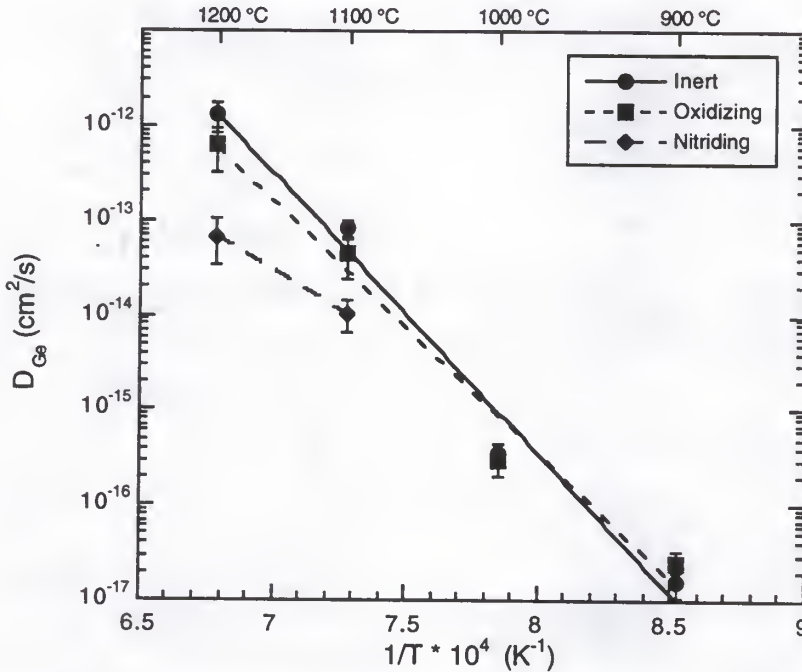


Figure 3-2. Effective Ge diffusivity of structure SQW/MBE as a function of annealing temperature in inert, oxidizing, and nitriding ambients.

Table 3-1. Extracted diffusivity and enhancement values for SQW/MBE.

T (°C)	time (min)	$D_{Ge}^{Inert}(cm^2/s)$	$D_{Ge}^{Ox}(cm^2/s)$	$D_{Ge}^{Nit}(cm^2/s)$	f_{enh}^{Ox}	f_{enh}^{Nit}
900	330	1.70×10^{-17}	2.32×10^{-17}	-	1.49	-
	980	2.29×10^{-17}	1.27×10^{-17}	-	0.555	-
	1532	2.08×10^{-17}	6.34×10^{-18}	-	0.305	-
	2206	2.08×10^{-17}	-	-	-	-
1000	43	3.00×10^{-16}	3.28×10^{-16}	-	1.09	-
	55	3.29×10^{-16}	4.56×10^{-16}	-	1.38	-
	87	3.29×10^{-16}	3.94×10^{-16}	-	1.20	-
	125	3.00×10^{-16}	2.74×10^{-16}	-	0.913	-
1100	1	5.20×10^{-14}	1.14×10^{-14}	1.46×10^{-14}	0.219	0.281
	2	7.93×10^{-14}	5.20×10^{-14}	4.88×10^{-15}	0.656	0.062
	3	6.69×10^{-14}	4.21×10^{-14}	1.59×10^{-14}	0.629	0.238
	4	8.60×10^{-14}	7.93×10^{-14}	1.24×10^{-14}	0.922	0.144
1200	1	2.38×10^{-12}	4.05×10^{-13}	1.10×10^{-13}	0.170	0.046
	1.5	6.00×10^{-13}	4.93×10^{-13}	2.47×10^{-14}	0.822	0.041
	2	1.08×10^{-12}	4.56×10^{-13}	1.02×10^{-13}	0.422	0.094
	3	1.08×10^{-12}	4.56×10^{-13}	5.02×10^{-14}	0.422	0.046

The extracted diffusivity values for structure SQW/VPE annealed in inert, oxidizing, and nitriding ambients are given in Table 3-2.

Table 3-2. Extracted diffusivity and enhancement values for SQW/VPE.

T (°C)	time (min)	$D_{Ge}^{Inert}(cm^2/s)$	$D_{Ge}^{Ox}(cm^2/s)$	$D_{Ge}^{Nit}(cm^2/s)$	f_{enh}^{Ox}	f_{enh}^{Nit}
900	330	2.18×10^{-17}	2.53×10^{-17}	-	1.16	-
1000	43	3.94×10^{-16}	3.29×10^{-16}	-	0.835	-
1100	1	9.00×10^{-14}	4.72×10^{-14}	1.73×10^{-14}	0.524	0.192
1200	1	1.54×10^{-12}	2.73×10^{-13}	1.40×10^{-13}	0.177	0.091

The values of the diffusivities for structure SQW/VPE as a function of temperature in inert, oxidizing, and nitriding ambients are shown in Figure 3-3. Fitting this data to an Arrhenius expression results in the following equations when the interdiffusion is carried out in inert, oxidizing, and nitriding ambients:

$$D_{\text{Ge}}^{\text{Inert}}(\text{SQW} / \text{VPE}) = 4.8 \times 10^7 \exp(-5.71\text{eV} \pm 0.23 / kT) \text{ cm}^2/\text{s} \quad (3-11)$$

$$D_{\text{Ge}}^{\text{Ox}}(\text{SQW} / \text{VPE}) = 1.0 \times 10^4 \exp(-4.81\text{eV} \pm 0.22 / kT) \text{ cm}^2/\text{s} \quad (3-12)$$

$$D_{\text{Ge}}^{\text{Nit}}(\text{SQW} / \text{VPE}) = 2.2 \times 10^{-4} \exp(-2.73\text{eV} \pm 0.10 / kT) \text{ cm}^2/\text{s} \quad (3-13)$$

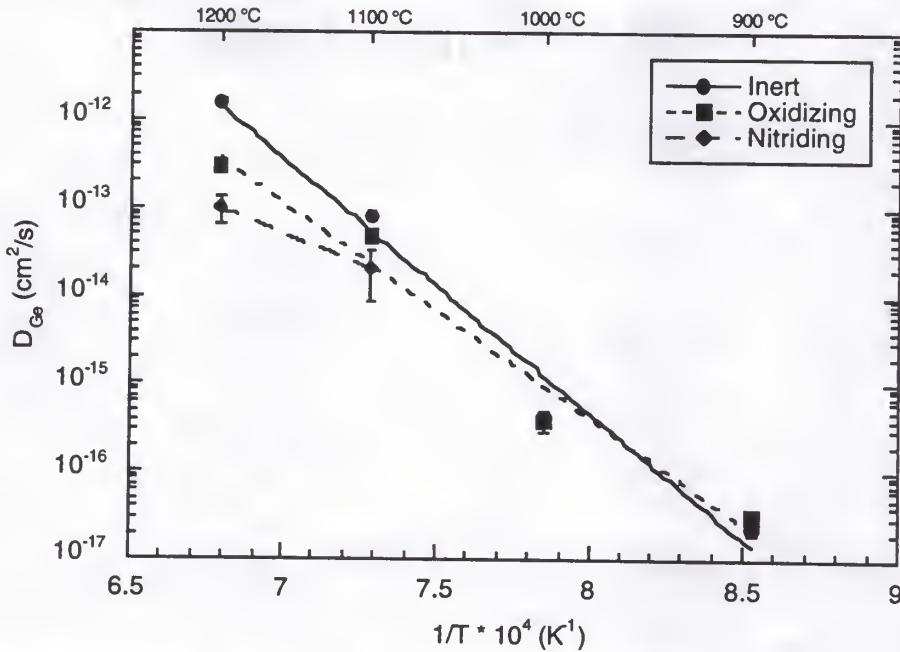


Figure 3-3. Effective Ge diffusivity of structure SQW/VPE as a function of annealing temperature in inert, oxidizing, and nitriding ambients.

3.4.2 Diffusion Behavior of Partially Relaxed Structures

The SQW/MBE and SQW/VPE structures have $\text{Si}_{1-x}\text{Ge}_x$ layers which are greater than critical thickness and TEM analysis confirms that these layers are partially relaxed through the presence of dislocations prior to any high-temperature processing. The initial stage of high-temperature treatment of these structures could cause additional strain relaxation by formation and propagation of misfit dislocations as well as strain-enhanced diffusion, thereby affecting the diffusivity. To address this issue, diffusivities of structures which were initially partially relaxed were compared to the diffusivities reported in Table 3-1 for the as-grown structures (for this analysis, assumed to be fully strained).

The annealed SQW/MBE samples (Table 3-1) were used to represent the partially relaxed structures, and their SIMS profiles were used as the initial profiles in the FLOOPS simulations. For example, the SIMS profile of the SQW/MBE sample annealed at 900 °C for 330 min was used as the initial 'partially relaxed' profile and diffusion was simulated for 650 min. A diffusivity was extracted by fitting the resulting simulated profile to the SIMS profile of the SQW/MBE sample that had been annealed at 900 °C for 980 min. This method was used to extract diffusivities for all SQW/MBE samples annealed in inert, oxidizing, and nitriding ambients. The values extracted for each temperature and time are given in Table 3-3. Values in italics represent the diffusivities of the as-grown structures after their first anneal and are included for purposes of comparison. A value for the sample annealed in

oxidizing ambient from 1532 min to 2206 min could not be extracted because after 2206 min the oxide had consumed the Si cap layer and had oxidized a portion of the $\text{Si}_{1-x}\text{Ge}_x$ layer.

Table 3-3. Extracted diffusivities for initially partially relaxed SQW/MBE.

T (°C)	time (min)	$D_{\text{Ge}}^{\text{Inert}}(\text{cm}^2/\text{s})$	$D_{\text{Ge}}^{\text{Ox}}(\text{cm}^2/\text{s})$	$D_{\text{Ge}}^{\text{Nit}}(\text{cm}^2/\text{s})$
900	0 to 330	1.70×10^{-17}	2.32×10^{-17}	-
	330 to 980	2.53×10^{-17}	1.54×10^{-17}	-
	980 to 1532	2.41×10^{-17}	1.15×10^{-17}	-
	1532 to 2206	2.29×10^{-17}	-	-
1000	0 to 43	3.00×10^{-16}	3.28×10^{-16}	-
	43 to 55	3.00×10^{-16}	6.22×10^{-16}	-
	55 to 87	2.74×10^{-16}	2.50×10^{-16}	-
	87 to 125	2.50×10^{-16}	2.74×10^{-16}	-
1100	0 to 1	5.20×10^{-14}	1.14×10^{-14}	1.46×10^{-14}
	1 to 2	5.90×10^{-14}	1.02×10^{-13}	1.37×10^{-15}
	2 to 3	2.23×10^{-14}	5.20×10^{-14}	2.64×10^{-14}
	3 to 4	7.29×10^{-14}	1.02×10^{-13}	4.88×10^{-15}
1200	0 to 1	2.38×10^{-12}	2.47×10^{-12}	1.10×10^{-13}
	1 to 1.5	4.21×10^{-13}	2.03×10^{-12}	2.11×10^{-14}
	1.5 to 2	4.21×10^{-13}	1.17×10^{-12}	2.24×10^{-13}
	2 to 3	7.91×10^{-13}	8.55×10^{-13}	1.42×10^{-14}

3.4.3 $\text{Si}_{1-x}\text{Ge}_x$ Single Quantum Well with Boron Marker Layer

As stated in section 1.2 and 3.4.1, the thickness of the $\text{Si}_{1-x}\text{Ge}_x$ layer in both SQW sample structures was greater than the critical thickness. Annealing caused strain relaxation through the generation of misfit and threading dislocations. These dislocations (in either the Si or $\text{Si}_{1-x}\text{Ge}_x$ layer) can possibly trap interstitials or vacancies injected during the oxidation or nitridation process, thus severely limiting the role these excess point defects

play in Ge diffusion in the $\text{Si}_{1-x}\text{Ge}_x$ layer. Before interpreting the diffusivity results given above, it had to be determined whether the injected interstitials were indeed trapped by the dislocations or whether they traveled to and throughout the $\text{Si}_{1-x}\text{Ge}_x$ layer to participate in the diffusion process.

A test structure, hereafter referred to as SQW/B, was grown which consisted of a lightly doped p-type Si (100) substrate with a 50nm Si buffer, followed by a 200nm boron-doped Si layer, with a B concentration of $5 \times 10^{18} \text{ cm}^{-3}$. A layer structure identical to that of the original SQW/MBE and SQW/VPE test structures was grown on top of these layers: a 1 μm Si "buffer" layer, followed by a 50 nm undoped $\text{Si}_{0.85}\text{Ge}_{0.15}$ layer and an undoped 50 nm Si cap layer (Figure 3-4).

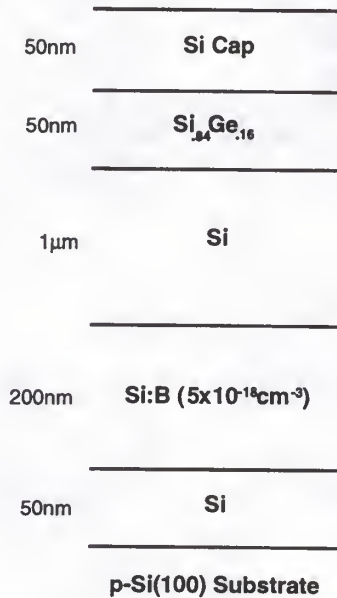


Figure 3-4. Schematic of test structure SQW/B. A buried boron marker layer is positioned below Si/ $\text{Si}_{1-x}\text{Ge}_x$ /Si layers similar to the SQW/MBE and SQW/VPE test structures.

Boron diffuses in Si predominantly through an interstitial mechanism [Fah89a]. If the B in the marker layer underneath the $\text{Si}_{1-x}\text{Ge}_x$ layer shows enhanced diffusion after annealing in interstitial-injecting (O_2) ambient compared to inert (N_2/Ar) ambient, it can be concluded that the interstitials are indeed traveling throughout the $\text{Si}_{1-x}\text{Ge}_x$ layer without a significant amount being captured by any dislocations formed. The interstitials are therefore available to facilitate the diffusion process. Any differences in Ge diffusion seen between inert and oxidizing ambients were indeed due to the injection of point defects.

The SQW/B structure was furnace-annealed at 900 °C for 330 min and at 1000 °C for 43 min in both N_2 and O_2 . The SQW/B structure was also rapid thermally processed at 1100 °C for 2 min and at 1200 °C for 1 min in Ar, O_2 and NH_3 . These are selected anneal conditions identical to four anneal conditions used for structures SQW/MBE and SQW/VPE. The B profiles before and after anneal were determined using SIMS (Figure 3-5). Qualitatively, B diffusion was greater in O_2 ambient than in Ar/ N_2 ambient for all temperatures. B diffusion in NH_3 was equivalent in NH_3 ambient compared to Ar ambient.

FLOOPS was used to determine the quantitative transport of interstitials through the $\text{Si}_{1-x}\text{Ge}_x$ layer to the B marker layer. The SIMS profile of the as grown boron marker layer was used as the initial B profile. The diffusivity of B in Si under both inert [Bar84] and oxidizing [Pac90] conditions is well-established, so the diffusion coefficient was maintained constant while the *time* of anneal was changed in FLOOPS until the simulated profile fit the

SIMS profile after anneal. For diffusion in nitriding ambient, the vacancy supersaturation at the surface was set at the established ratio [Mog96], which then set the non-equilibrium interstitial concentration. Once again, the time of anneal was changed in FLOOPS until the simulated profile fit the SIMS profile after anneal. Table 3-4 gives a summary of the anneal times calculated by FLOOPS compared to the actual anneal times in inert, oxidizing and nitriding ambients. Actual anneal times are given in column 2.

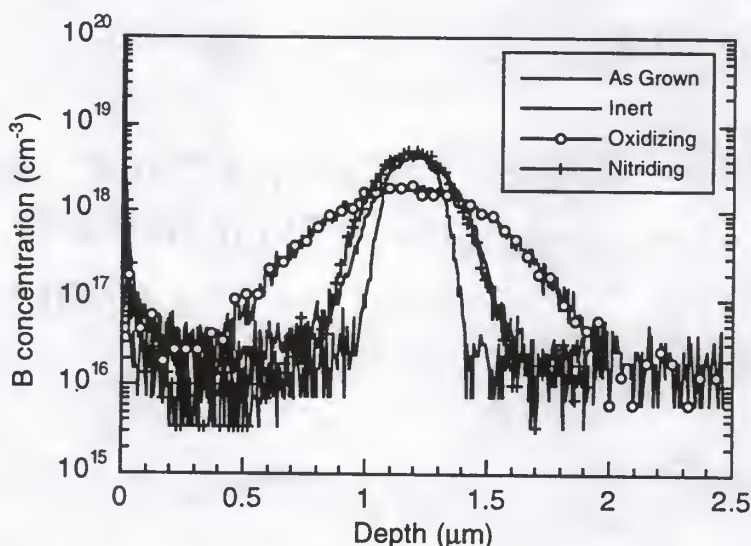


Figure 3-5. Diffusion of as-grown B marker layer in all ambients. Sample was annealed at 1100 °C for 2 minutes. Diffusion of B in oxidizing ambient is noticeably greater than in inert and nitriding ambients.

Table 3-4. Anneal times needed in FLOOPS to achieve actual B diffusion profiles.

T (°C)	actual anneal time (min)	t_{Ar} (min)	t_{Ox} (min)	t_{Nit} (min)
900	330	1100	2200	
1000	43	90	160	
1100	2	6	32	2.6
1200	1	0.7	0.6	0.5

3.4.4 Estimation of Fractional Interstitial Components of Diffusion

Initially, the Pair model was used in FLOOPS to provide simulated concentration versus depth profiles which fit the SIMS profiles of the samples processed in oxidizing ambient. The fractional interstitial components of diffusion, f_i , were estimated within the Pair model by solving Equation 3-5. The values of the inert (intrinsic) diffusivity, D^* , were simply the D_{Ge}^{Inert} values listed in Table 3-1. The values of C_i/C_i^* and C_v/C_v^* under oxidizing conditions for the temperatures studied were the default values used by FLOOPS [Pac90]. The resultant f_i values were ~ 0.10 , which corresponded well with the minimal amount of diffusion enhancement seen during interstitial supersaturation.

This method was repeated to estimate f_i values for the samples processed in nitriding ambient. Once again, the values of the inert (intrinsic) diffusivity, D^* , were the D_{Ge}^{Inert} values listed in Table 3-1. The values of C_i/C_i^* and C_v/C_v^* under nitriding conditions for the temperatures studied were those reported in an extensive study by Mogi [Mog96]. Quantitative f_i values could not be estimated because the D^* values (D_{Ge}^{Inert}) for every processing temperature and time were so large that they greatly overestimated the diffusion. Qualitatively, the Pair model, when applied to the nitriding experiments, indicated an extremely large interstitial component of diffusion. While this result corresponded well with the significant retardation seen during vacancy supersaturation, it contradicted the small interstitial component predicted by the oxidation experiments.

Two possible reasons for the discrepancy between the results of the oxidation and nitridation experiments were (1) the D^* values measured in Section 3.4.1 were not the correct values and had been affected in some manner not accounted for in the Fermi model and (2) the interstitial and vacancy supersaturation values, C_I/C_I^* and C_V/C_V^* , that occurred during these oxidation and nitridation experiments differed from the values reported in previous studies that were employed in the Pair model to estimate the f_i values. If either of these conditions proved to be true, then the D^* values extracted using the Fermi model and the f_i values calculated using the Pair model could be considered unreliable. It was imperative, therefore, to determine as accurately as possible the actual values of D^* and C_I/C_I^* and C_V/C_V^* during processing of SQW/MBE in all three ambients. The best means available to this investigator to determine these values were through the B marker layer results discussed previously in Section 3.4.3 and later in Section 3.5.3. The comparison of the actual processing time and the time predicted by FLOOPS was used indicate the actual C_I/C_I^* value compared to the default value used in FLOOPS. This approach is discussed in greater detail in Section 3.5.3.

The analytical method which was adopted was: (1) a C_I/C_I^* value in inert ambient was determined for each temperature by taking the ratio of the boron diffusion time predicted by FLOOPS and the actual processing time, t_{Ar}/t_{Actual} , as presented in Table 3-4. (2) A corresponding C_V/C_V^* range in inert ambient was then estimated by designating its upper limit as case (i) in which

the vacancies are supplied as fast as they are depleted and thus always remain at their equilibrium concentration, such that $C_v/C_v^*=1$, and its lower limit as case (ii) in which the product of the interstitial and vacancy concentrations remains constant and $C_i C_v = C_i^* C_v^*$ such that $C_v/C_v^* = 1/(C_i/C_i^*)$. (3) A C_i/C_i^* value in oxidizing ambient was determined for each temperature by the ratio of t_{Ox}/t_{Actual} from the values presented in Table 3-4. (4) A constant f_i was assumed for a constant temperature regardless of processing ambient. (5) Equation 3-5 was solved simultaneously for both inert and oxidizing ambients, using the D_{Ge}^{Inert} and D_{Ge}^{Ox} values given in Table 3-1 for D , the C_i/C_i^* values from steps (1) and (3), and the C_v/C_v^* values from step (2) for both the upper and lower limit cases. This fifth step creates two equations with two unknowns, D^* and f_i , such that these two parameters can be computed for the specific processing temperatures and times used for the B marker layer experiments. The upper (i) and lower (ii) bound cases for C_v/C_v^* create upper and lower bounds for the resultant D^* and f_i values.

It is important to note here that these D^* and f_i values apply most rigorously to only the processing temperatures and times at which they were extracted from the B marker layer experiments. The analysis was adapted and extended as follows to address the additional processing times for SQW/MBE in Table 3-1. (6) The D^* and f_i values determined for a constant temperature from step (5) were considered constant with increasing processing time, while the C_i/C_i^* and C_v/C_v^* values were allowed to change with time. It has been widely accepted that non-equilibrium concentrations of interstitials and

vacancies vary with processing time [Fah89]. (7) The D^* and f_i values from step (6) were used in Equation 3-5 for each additional processing time, along with the limiting values of C_v/C_v^* from step (2), to determine upper and lower bounds for C_i/C_i^* . For some processing temperatures and times the upper limit of $C_v/C_v^*=1$ was too high to give sensible values of either f_i or C_i/C_i^* , so the limit was lowered until sensible values could be obtained. These values of D^* , C_i/C_i^* , C_v/C_v^* and f_i determined from steps (1) through (7) for inert and oxidizing experiments for each temperature and processing time are given in Tables 3-5 and Table 3-6 respectively. The first row for each processing time represents the results using the lower bound for C_v/C_v^* , while the second row represents the results using the upper bound. The cells with no data represent conditions in which the particular bound did not provide reasonable results for either f_i or C_i/C_i^* .

The above method was applied to the nitriding ambient experiments conducted at 1100 and 1200 °C to determine f_i and C_v/C_v^* values during vacancy supersaturation. The C_i/C_i^* ratio of SQW/MBE was estimated using the $t_{\text{Nit}}/t_{\text{Actual}}$ ratio from the values listed Table 3-4, but in this case C_v/C_v^* had a lower bound of $1/(C_i/C_i^*)$ and an upper bound of infinity. This was because the B marker layer only measured the enhancement/retardation from the interstitial concentration not the amount of vacancies being injected, thus C_i/C_i^* could be calculated but not C_v/C_v^* . The supersaturation of vacancies can only be reliably estimated by quantifying the movement of a dopant

Table 3-5. Fractional interstitial components and modified diffusivities and point defect supersaturations determined for diffusion in inert ambient.

T (°C)	time (min)	D(cm ² /s)	D*(cm ² /s)	C _i /C _i *	C _v /C _v *	f _i
900	330	1.70×10 ⁻¹⁷	1.28×10 ⁻¹⁷	3.33	1.00	0.140
		1.70×10 ⁻¹⁷	2.38×10 ⁻¹⁷	3.33	0.330	0.127
	980	2.29×10 ⁻¹⁷	1.28×10 ⁻¹⁷	6.64	1.00	0.140
		2.29×10 ⁻¹⁷	2.38×10 ⁻¹⁷	6.52	0.115	0.127
	1532	2.08×10 ⁻¹⁷	1.28×10 ⁻¹⁷	5.46	1.00	0.140
		2.08×10 ⁻¹⁷	2.38×10 ⁻¹⁷	5.67	0.176	0.127
	2206	2.08×10 ⁻¹⁷	1.28×10 ⁻¹⁷	5.46	1.00	0.140
		2.08×10 ⁻¹⁷	2.38×10 ⁻¹⁷	5.67	0.176	0.127
	1000	3.00×10 ⁻¹⁶	2.82×10 ⁻¹⁶	2.09	1.00	0.059
		3.00×10 ⁻¹⁶	4.19×10 ⁻¹⁶	2.09	0.480	0.148
1100	55	3.29×10 ⁻¹⁶	2.82×10 ⁻¹⁶	3.55	1.00	0.059
		3.29×10 ⁻¹⁶	4.19×10 ⁻¹⁶	3.78	0.265	0.148
	87	3.29×10 ⁻¹⁶	2.82×10 ⁻¹⁶	3.55	1.00	0.059
		3.29×10 ⁻¹⁶	4.19×10 ⁻¹⁶	3.78	0.265	0.148
	125	3.00×10 ⁻¹⁶	2.82×10 ⁻¹⁶	2.09	1.00	0.059
		3.00×10 ⁻¹⁶	4.19×10 ⁻¹⁶	2.09	0.480	0.148
	1	5.20×10 ⁻¹⁴	7.77×10 ⁻¹⁴	-	1.00	0.010
		5.20×10 ⁻¹⁴	2.19×10 ⁻¹³	5.69	0.176	0.011
	2	7.93×10 ⁻¹⁴	7.77×10 ⁻¹⁴	3.00	1.00	0.010
		7.93×10 ⁻¹⁴	2.19×10 ⁻¹³	3.00	0.330	0.011
1200	3	6.69×10 ⁻¹⁴	7.77×10 ⁻¹⁴	-	1.00	0.010
		6.69×10 ⁻¹⁴	2.19×10 ⁻¹³	3.72	0.269	0.011
	4	8.60×10 ⁻¹⁴	7.77×10 ⁻¹⁴	11.8	1.00	0.010
		8.60×10 ⁻¹⁴	2.19×10 ⁻¹³	2.74	0.365	0.011
	1	2.38×10 ⁻¹²	-	0.700	1.00	-
		2.38×10 ⁻¹²	1.70×10 ⁻¹²	0.700	1.43	0.045
	1.5	6.00×10 ⁻¹³	-	-	-	-
		6.00×10 ⁻¹³	1.70×10 ⁻¹²	4.80	0.208	0.033
	2	1.08×10 ⁻¹²	-	-	-	-
		1.08×10 ⁻¹²	1.70×10 ⁻¹²	1.71	0.585	0.045
1200	3	1.08×10 ⁻¹²	-	-	-	-
		1.08×10 ⁻¹²	1.70×10 ⁻¹²	1.71	0.585	0.045

Table 3-6. Fractional interstitial components and modified diffusivities and point defect supersaturations determined for diffusion in oxidizing ambient.

T (°C)	time (min)	D(cm ² /s)	D*(cm ² /s)	C _i /C _i *	C _v /C _v *	f _i
900	330	2.32×10 ⁻¹⁷	1.28×10 ⁻¹⁷	6.67	1.00	0.140
		2.32×10 ⁻¹⁷	2.38×10 ⁻¹⁷	6.67	0.150	0.127
	980	1.27×10 ⁻¹⁷	1.28×10 ⁻¹⁷	0.940	1.00	0.140
		1.27×10 ⁻¹⁷	2.38×10 ⁻¹⁷	3.40	0.290	0.077
	1532	6.34×10 ⁻¹⁸	1.28×10 ⁻¹⁷	0.002	1.00	0.506
		6.34×10 ⁻¹⁸	2.38×10 ⁻¹⁷	7.30	0.130	0.018
1000	43	3.28×10 ⁻¹⁶	2.82×10 ⁻¹⁶	3.72	1.00	0.059
		3.28×10 ⁻¹⁶	4.19×10 ⁻¹⁶	3.72	0.480	0.148
	55	4.56×10 ⁻¹⁶	2.82×10 ⁻¹⁶	11.5	1.00	0.059
		4.56×10 ⁻¹⁶	4.19×10 ⁻¹⁶	6.48	0.150	0.148
	87	3.94×10 ⁻¹⁶	2.82×10 ⁻¹⁶	7.78	1.00	0.059
		3.94×10 ⁻¹⁶	4.19×10 ⁻¹⁶	5.26	0.190	0.148
	125	2.74×10 ⁻¹⁶	2.82×10 ⁻¹⁶	0.530	1.00	0.059
		2.74×10 ⁻¹⁶	4.19×10 ⁻¹⁶	2.70	0.360	0.121
	1	1.14×10 ⁻¹⁴	7.77×10 ⁻¹⁴	-	0.501	0.010
		1.14×10 ⁻¹⁴	2.19×10 ⁻¹³	28.9	0.035	0.011
1100	2	5.20×10 ⁻¹⁴	7.77×10 ⁻¹⁴	16.0	0.501	0.010
		5.20×10 ⁻¹⁴	2.19×10 ⁻¹³	16.0	0.063	0.011
	3	4.21×10 ⁻¹⁴	7.77×10 ⁻¹⁴	4.60	0.501	0.010
		4.21×10 ⁻¹⁴	2.19×10 ⁻¹³	8.65	0.116	0.011
	4	7.93×10 ⁻¹⁴	7.77×10 ⁻¹⁴	52.4	0.501	0.010
		7.93×10 ⁻¹⁴	2.19×10 ⁻¹³	5.43	0.184	0.011
	1	4.05×10 ⁻¹³	-	0.600	1.00	-
		4.05×10 ⁻¹³	1.70×10 ⁻¹²	0.600	1.67	0.045
	1.5	4.93×10 ⁻¹³	-	-	-	-
		4.93×10 ⁻¹³	1.70×10 ⁻¹²	7.00	0.143	0.014
1200	2	4.56×10 ⁻¹³	-	-	-	-
		4.56×10 ⁻¹³	1.70×10 ⁻¹²	5.90	0.169	0.021
	3	4.56×10 ⁻¹³	-	-	-	-
		4.56×10 ⁻¹³	1.70×10 ⁻¹²	5.90	0.169	0.021

which diffuses through a predominantly vacancy mechanism, such as antimony. Therefore, the upper bound of C_v/C_v^* was unknown from the B marker layer results and theoretically an infinite number of vacancies might have been injected. For purposes of calculation, however, an upper bound of $C_v/C_v^*=4$ [Mog96] was used initially in step (2) to extract an f_i . Unfortunately, neither the lower bound of $1/(C_i/C_i^*)$ nor the upper bound of 4 for C_v/C_v^*

resulted in sensible values for f_i using the B marker layer results. Even when the lower bound was decreased below $1/(C_l/C_l^*)$ and the upper bound for C_v/C_v^* was raised above 4, f_s could not be estimated because the $D_{\text{Ge}}^{\text{Nit}}/D^*$ ratio from the values in Tables 3-1 and 3-5 were consistently too small. Discussion of this phenomena is presented in Section 3.5.4.

3.4.5 TEM

The amount of initial relaxation of the structures immediately after growth is determined by the growth temperature, layer thickness, Ge content and the initial condition of the substrate [Iye89]. Upon annealing, the structure will relax to reduce the strain energy. The minimum energy can be attained by diffusion of Ge towards a compositional average or by the generation of misfit dislocations. Both of these mechanisms compete and their respective contributions are dictated by kinetic conditions. Because SQW/MBE and SQW/VPE are strained and have been shown to have dislocations after growth and before thermal processing, it is important to know at least qualitatively the dislocation densities after annealing compared to that of the as grown structures. This will give a qualitative idea of the possible contribution of relaxation through dislocation formation to the diffusivity values calculated in the preceding section.

All plan views were taken with the zone axis of (100) so that the sample is exactly perpendicular to the electron beam, and the (220) reflection was used.

Both plan view and cross section can only provide qualitative defect density data instead of quantitative results in the case of multiple deposited epilayers. In plan view, the image is taken from the top of the sample surface, so the interfaces of every multilayer are not visible. There may be dislocations at interfaces that are buried from view using the plan view perspective that make it impossible to precisely state the number of dislocations present in an entire unit volume. Similarly, it is nearly impossible to get a meaningful estimate of the number of dislocations from cross-sectional view. XTEM only investigates a very small area of the entire sample and is therefore not statistically significant. More importantly, the direction of view used in these and most cross sections is the (110) direction, so that half the dislocation is hidden while the other half lies parallel to the interface, making it impossible to observe whether one or more dislocations are contained within the thickness of the sample.

As discussed in Section 2.2.3, the as-grown SQW/MBE and SQW/VPE exhibited strain relief through an array of misfit dislocations spaced an average of approximately 1 μm apart, however, no threading dislocations were present in cross sectional images of the as-deposited structures (Figure 2-7). As stated above, this does not necessarily mean that there *were* no threading dislocations, there was just no conclusive evidence of them. The precise source of the misfit dislocations is unclear at present but could most likely be due to the high growth temperature of 700 °C.

Cross sectional images, shown in Figure 3-6, were taken of SQW/MBE samples annealed at 1000 °C for 43 min and 1200 °C for 1 min in inert ambient and are shown at a magnification of $\times 50k$. In Figure 3-6a the substrate is highly dislocated after processing at 1000 °C for 43 min. Nearer to the surface, where the $Si_{1-x}Ge_x$ well lies, there are unusual artifacts which do not resemble normal threading or misfit dislocations. They might be a result of sample preparation. These obscure the layers so that no information on diffusion can be obtained. In Figure 3-6b there are misfit dislocations along the interface as well as threading dislocations from the substrate/buffer interface to the surface, evidence that relaxation has occurred after processing at 1200 °C for 1 min. Also, the $Si_{1-x}Ge_x$ layer is no longer clearly visible, so significant diffusion has occurred.

Plan view images were taken of SQW/MBE samples annealed at the extremes of the temperatures used in these experiments, 900 and 1200 °C, and are shown at a magnification of $\times 20k$. The misfit dislocation density increased only slightly for SQW/MBE annealed at 900 °C for 330 minutes (Figure 3-7a). The distance between dislocations decreased to 0.5 μm from the as-grown value of 1 μm . For the SQW/MBE sample annealed at 1200 °C for 1 min (Figure 3-7b), the misfit dislocation density was very similar to that at 900 °C, and once again, noticeably greater than that of the as-grown structure. There was also an origination of curved segments not seen in the sample annealed at 900 °C or as-grown material. These were most likely expanded threading dislocations seen from an overhead perspective. Oddly, plan view

images of sample SQW/VPE annealed at the same temperatures and times show opposite results to those of SQW/MBE. The sample annealed at 900 °C for 330 min shows a very large increase in misfit dislocations, as well as large numbers of threading dislocations (Figure 3-8a). After anneal at 1200 °C for 1 min, there was a much lower misfit dislocation density and no evidence of curved segments indicating threading dislocations (Figure 3-8b). The reason for the contradictory behavior of SQW/MBE and SQW/VPE is unknown.

From the experiments done in this study, it is difficult to determine exactly what impact this increase in dislocation density had on interdiffusion. These TEM results suggest that future work needs to be done with structures which are pseudomorphic.

3.5 Discussion

3.5.1 Diffusivities of Fully-Strained Structures

The FLOOPS diffusion models used in this study were the Fermi and Pair models. The diffusion profiles generated by the Fermi model provided very good fits to the experimentally determined SIMS profiles in the case of anneals performed in inert ambient, as demonstrated in Figure 3-9a for 1000 °C and an anneal time of 43 min. This indicates that the assumptions made in the FLOOPS model (Section 3.3), while not necessarily accurate, are good enough to provide diffusivity values that are reasonable.



a.

50,000x

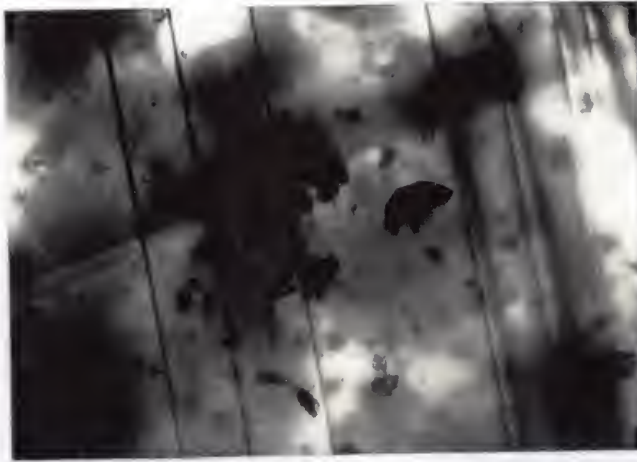

200nm

b.

50,000x


200nm

Figure 3-6. Cross sectional view TEM micrographs of structure SQW/MBE after annealing in inert ambient at (a) 1000°C for 43 min and (b) 1200°C for 1 min.



a.


20,000x
500nm

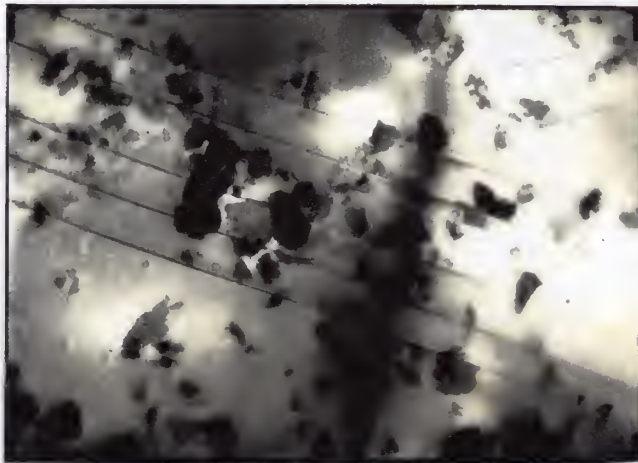
b.

20,000x
500nm

Figure 3-7. Plan-view TEM micrographs of structure SQW/MBE after annealing in inert ambient at (a) 900 °C for 330 min and (b) 1200 °C for 1 min.



a. 20,000x  500nm




b. 20,000x  500nm

Figure 3-8. Plan-view TEM micrographs of SQW/VPE after annealing at (a) 900 °C for 330 min in oxidizing ambient and (b) 1200 °C for 1 min in inert ambient.

The enhancement of diffusion at high concentrations of dopant atoms has been shown to manifest itself in a shape of the depth profile that is flatter at its peak and has steeper shoulders than the Gaussian that is expected for a concentration-independent diffusion coefficient, assuming that the initial profile is Gaussian [Gos93]. In this study, selected SIMS profiles of Ge obtained from anneals performed at 900 °C and 1000 °C show a flatter peak and slightly more rectangular shape than the Gaussian FLOOPS profile generated by a concentration-independent diffusivity (Figure 3-10). The flat peak profiles could indicate a concentration-dependent diffusion coefficient at these temperatures. There is a stronger possibility, however, that the flat profiles at the lower temperatures are just manifestations of the maximum allowable depth and concentration errors in SIMS measurement. This conclusion is supported for two reasons: (1) There is no identifiable trend in the flatness of the profiles with time and (2) profiles of samples with the same thermal processing history obtained during SIMS operation on a different day showed no peak flatness and were perfectly Gaussian. SIMS profiles obtained from anneals performed at 1100 °C and 1200 °C do not show flat-peak, concentration-dependent diffusion behavior at any anneal time. This may only mean that at the longer Ge diffusion lengths resulting from these high temperatures, the $\text{Si}_{1-x}\text{Ge}_x$ well is no longer identifiable, so any concentration dependency is unidentifiable. Cowern *et al.* [Cow96] have previously reported enhanced diffusion at Ge concentrations of 30% and an anneal temperature of

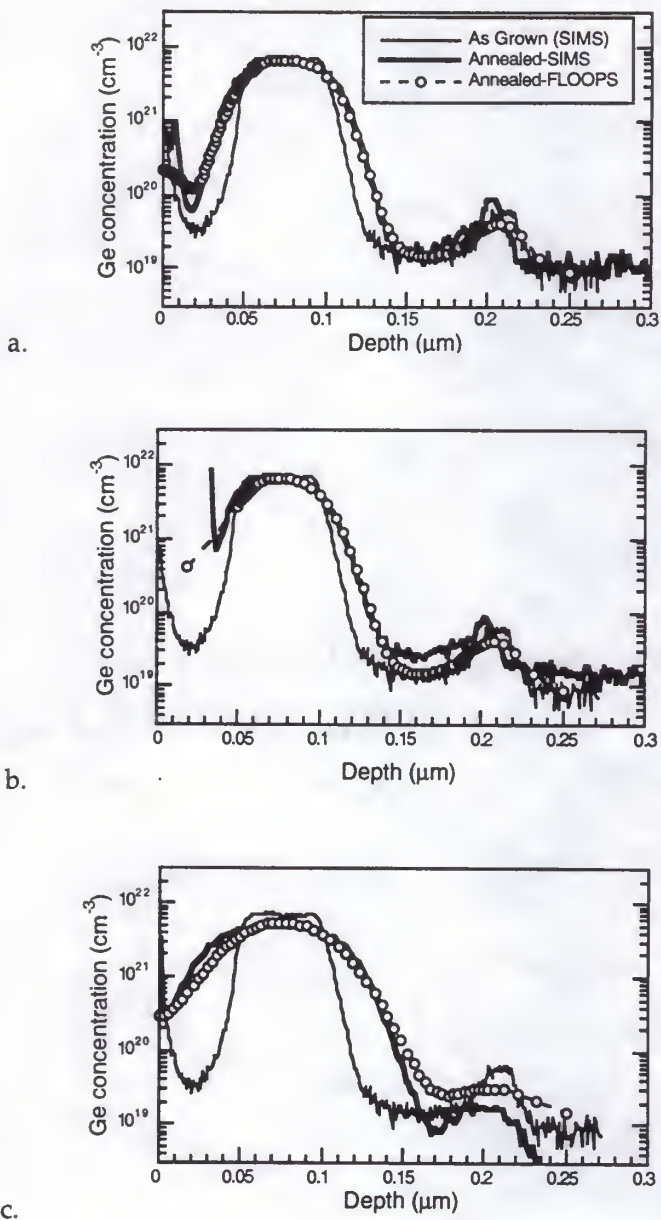
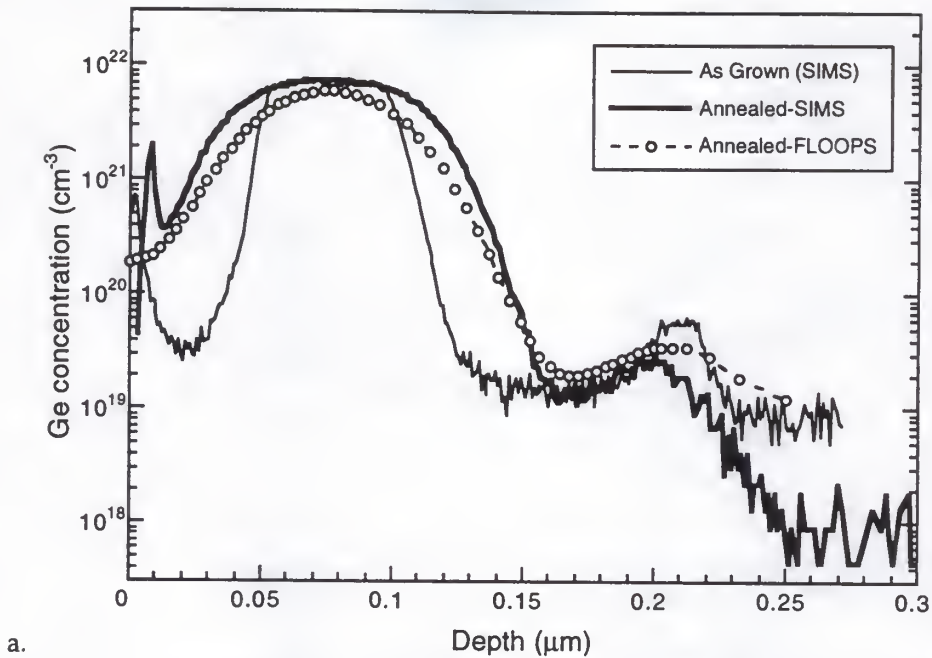
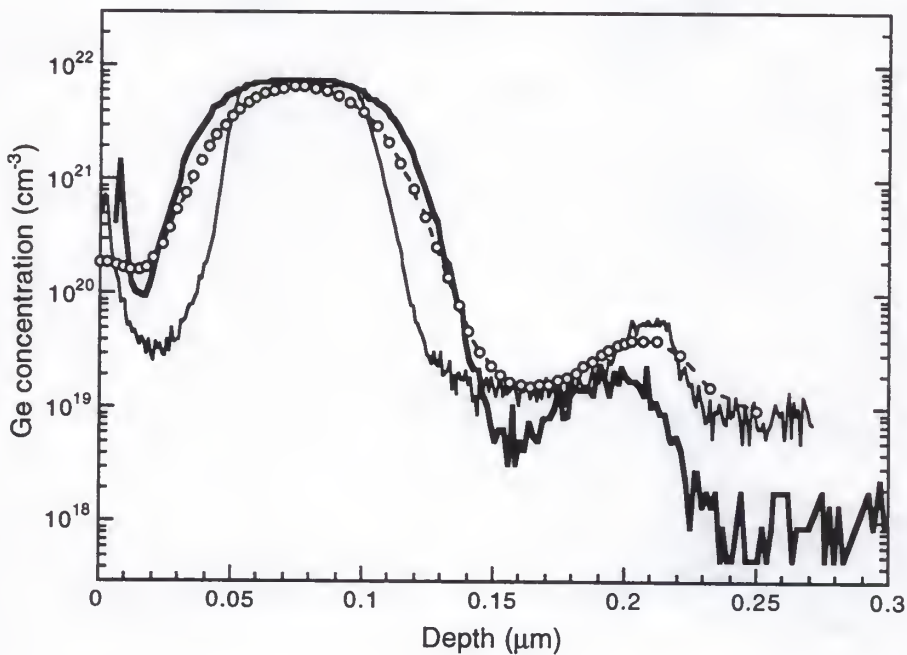


Figure 3-9. Comparison of experimentally determined SIMS profile and FLOOPS profile. Sample annealed at 1000 °C for 43 min in (a) inert ambient and (b) oxidizing ambient; (c) annealed at 1100 °C for 3 min in nitriding ambient.



a.



b.

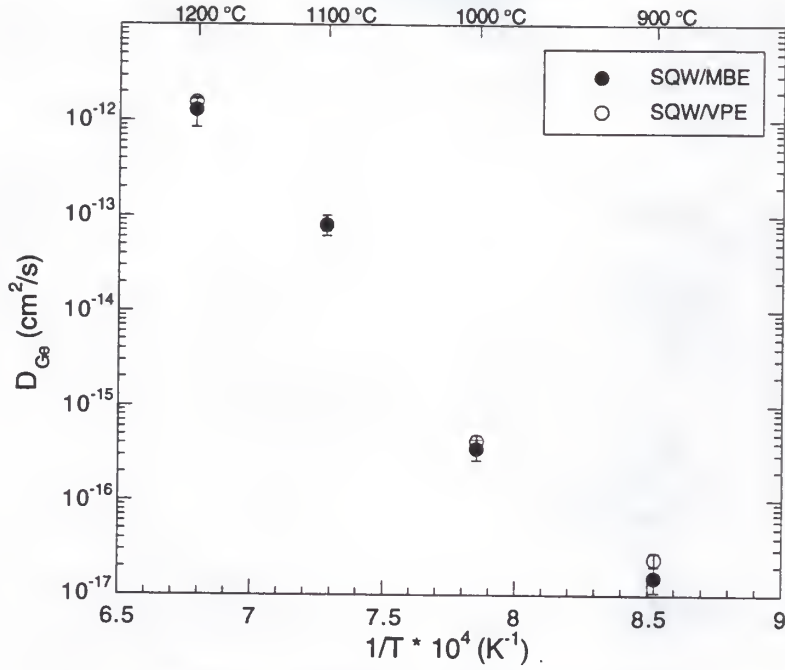
Figure 3-10. Illustration of non-Gaussian shape of SQW diffused profiles. of The as-grown, SIMS, and FLOOPS profiles of anneals at (a) 900 °C for 1532 min and (b) 1000 °C for 55 min. Each SIMS profile shows a flatter peak and steeper slopes than the corresponding FLOOPS profile.

875 °C. Results from this study show clearly that, in conjunction with the Cowern results, the possibility of a concentration dependent diffusion coefficient needs to be investigated further. Flat peaks were not seen in profiles of samples annealed in nitriding ambient.

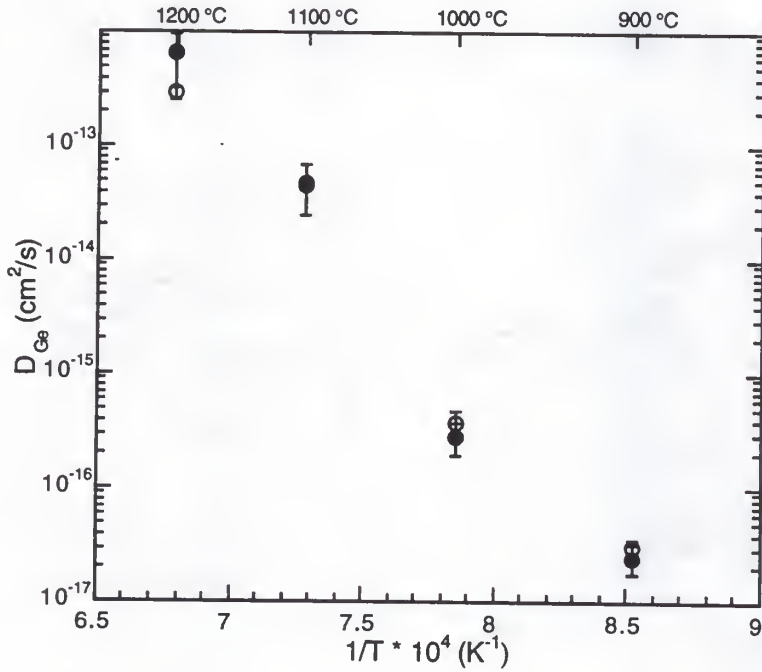
Comparison of the diffusivities of the two structures SQW/MBE and SQW/VPE (Table 3-7) shows that in inert, oxidizing, and nitriding ambients the diffusivities are equivalent within error, as determined from the analysis method in Section 2.3.2. Figure 3-11 shows this graphically for the inert and oxidizing ambient cases.

Activation energies of diffusion for each ambient given in Equations 3-8 through 3-10 are not all within one standard deviation of each other, but all are well within two standard deviations of each other. Because the diffusivities and activation energies of both SQW/MBE and SQW/VPE are similar throughout the entire temperature range of this study, it can be concluded that the different growth methods, in this case, have no effect on diffusion behavior. For the remainder of the discussion on SQW results, the two structures will be considered identical.

Previously reported values for the diffusivity of Ge in Si/Si_{1-x}Ge_x/Si structures in inert ambient are shown in Figure 3-12 [Sun94, Hol89, Zau94, Van90]. The diffusivities determined from this study at 900 and 1000 °C are slightly lower but still agree well with the diffusivities reported in the



a.



b.

Figure 3-11. Comparison of diffusivities of structures SQW/MBE and SQW/VPE in (a) inert ambient and (b) oxidizing ambient. Diffusivities at all temperatures are within error of each other.

Table 3-7. Comparison of diffusivities of SQW/MBE and SQW/VPE in inert and oxidizing ambients.

T (°C)	time (min)	Inert		Oxidizing		Nitriding	
		D:SQW/MBE (cm ² /s)	D:SQW/VPE (cm ² /s)	D:SQW/MBE (cm ² /s)	D:SQW/VPE (cm ² /s)	D:SQW/MBE (cm ² /s)	D:SQW/VPE (cm ² /s)
900	330	1.70×10^{-17}	2.18×10^{-17}	2.32×10^{-17}	2.53×10^{-17}	-	-
1000	43	3.00×10^{-16}	3.94×10^{-16}	3.028×10^{-16}	3.29×10^{-16}	-	-
1100	1	5.20×10^{-14}	9.00×10^{-14}	1.14×10^{-14}	4.72×10^{-14}	1.46×10^{-14}	1.73×10^{-14}
1200	1	2.38×10^{-12}	1.54×10^{-12}	2.47×10^{-14}	2.73×10^{-13}	1.10×10^{-13}	1.40×10^{-13}

literature over the temperature range 800 to 1010 °C. The values at 1100 and 1200 °C from this study are the only known diffusivities reported for this temperature range. This work reports diffusivities that span over five orders of magnitude (10^{-17} cm²/s to 10^{-12} cm²/s) while previous studies report diffusivities that extend over only two orders of magnitude at most. Therefore, the diffusivity data and activation energies determined in this study can be considered to be more reliable than any values reported previously.

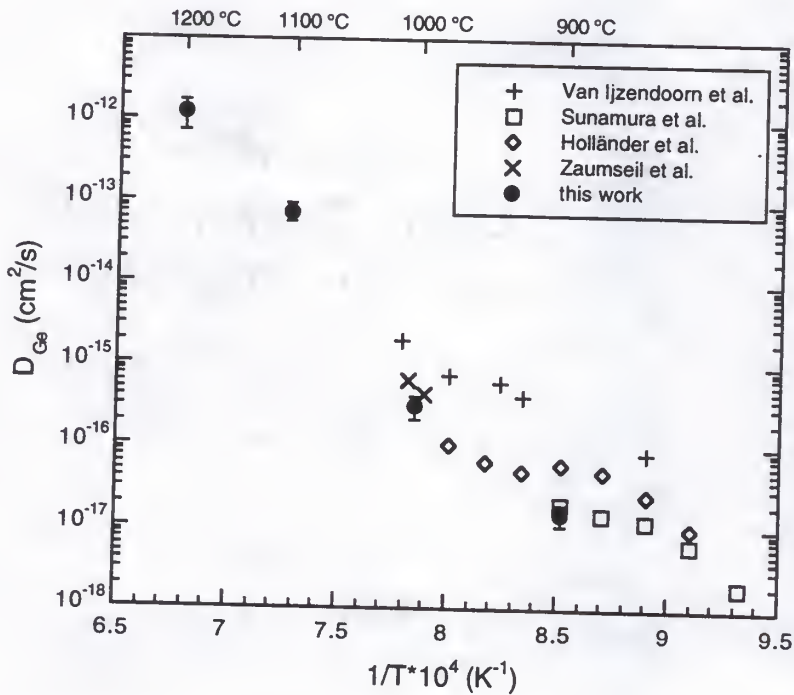


Figure 3-12. Diffusivities of Ge in Si/Si_{1-x}Ge_x/Si SQWs from previous studies and this work.

The activation energy of Ge diffusion in $\text{Si}/\text{Si}_{1-x}\text{Ge}_x/\text{Si}$ in inert ambient determined in this study, $5.87 \text{ eV} \pm 0.14$, is substantially higher than activation energies previously reported [Van90, Sun94]. Van Ijzendoorn *et al.* and Sunamura *et al.* both reported activation energies of approximately 2.5 eV for SQWs with Ge compositions $x=0.17$ and 0.16, respectively. While the thickness of the SQW studied in Sunamura *et al.* was below critical thickness, the thickness of the SQW studied by Ijzendoorn *et al.* was above critical thickness and the same as that of this study (50 nm). Because the SQWs of all three studies are similar, the larger activation energy determined from this study can most likely be attributed to the difference in temperature range investigated. The studies of Van Ijzendoorn *et al.* and Sunamura *et al.* were conducted in a relatively narrow temperature range from 800 to 1010 °C. It should also be noted that the activation energy calculated in this work (~ 5.8 eV) physically compares with the reported value for the Ge tracer diffusivity in pure Si [Fah89]. There is a possibility that after the structure has relaxed during the very first stage of processing, Ge diffusion in relaxed $\text{Si}_{1-x}\text{Ge}_x$ is similar to Ge diffusion in bulk (relaxed) Si.

The diffusivities given in Table 3-1 for inert ambient are constant with increasing time within error for temperatures from 900 to 1200 °C. At 1200 °C, the diffusivity of the shortest time anneal is not within error of the diffusivities of the longer anneals (Figure 3-13). This slight deviation of D for the shortest anneal time, however, is not seen at any other temperature. This does not seem to indicate a trend and is within one standard deviation of the

accepted error so will therefore be ignored. It can be concluded from this data that diffusion in inert ambient is time-independent at all temperatures within the studied range.

While the diffusivities for each temperature given in Table 3-1 for oxidizing ambient seem to vary more than in the inert case, the calculated error in measurement is greater. It can therefore be concluded that diffusion in an oxidizing ambient is also time-independent at all temperatures within 900 to 1200 °C. In nitriding ambient, at both anneal temperatures 1100 and 1200 °C, diffusivities at all anneal times are also within error of each other and diffusion can be considered time-independent.

Comparison of diffusion in inert, oxidizing and nitriding ambients yields interesting conclusions. At all temperatures, the diffusion profiles in an oxidizing ambient are very similar to the diffusion profiles in an inert ambient (Figure 3-14).

Diffusivities extracted are the same, within error, for temperatures 900 and 1000 °C, as illustrated in Figures 3-2 and 3-3. This indicates that a supersaturation of interstitials has very little effect on Ge diffusion at these temperatures and that vacancies are the dominant diffusing species. Diffusivities extracted for anneals at 1100 and 1200 °C are also within error of each other, as illustrated in Figures 3-2 and 3-3. The difference in diffusion coefficients increases moderately with increasing temperature, with the maximum divergence occurring at 1200 °C. At these higher temperatures, diffusivities are moderately *smaller* in oxidizing ambient than inert,

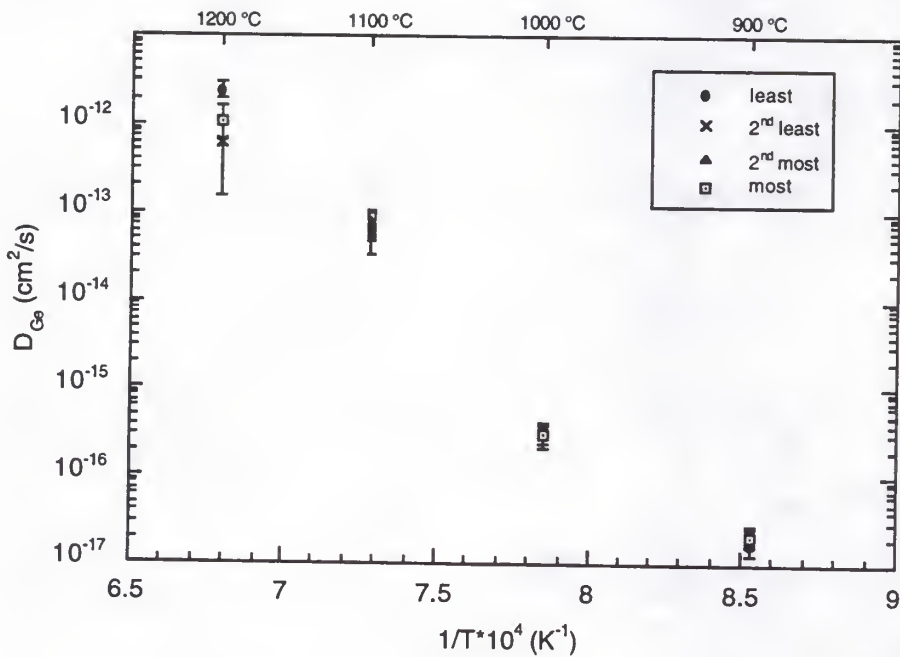


Figure 3-13. Plot of diffusivities of all anneal times in inert ambient for each temperature for SQW/MBE. Error bars show that at each temperature all diffusivities are within error of each other.

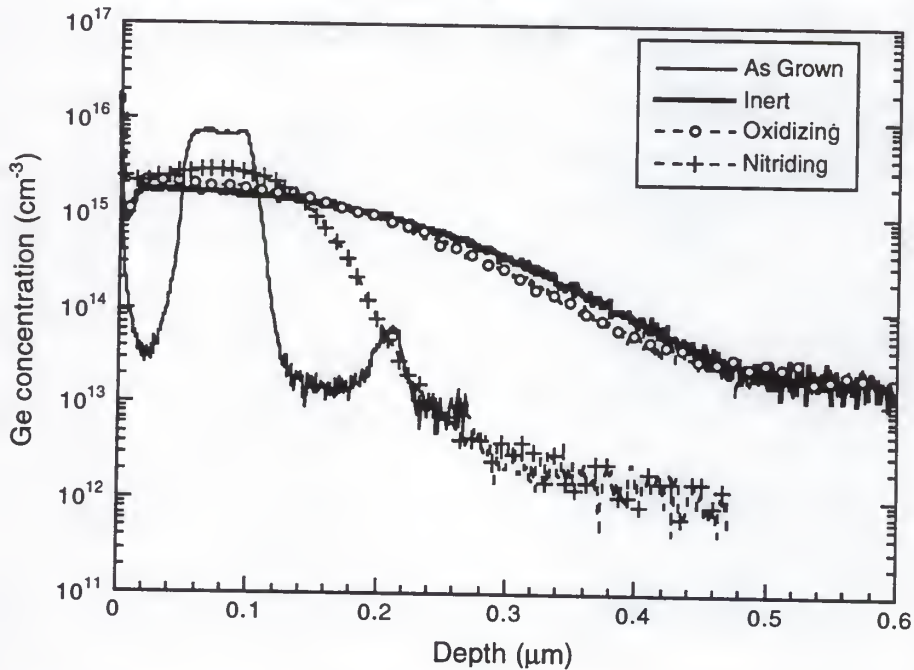
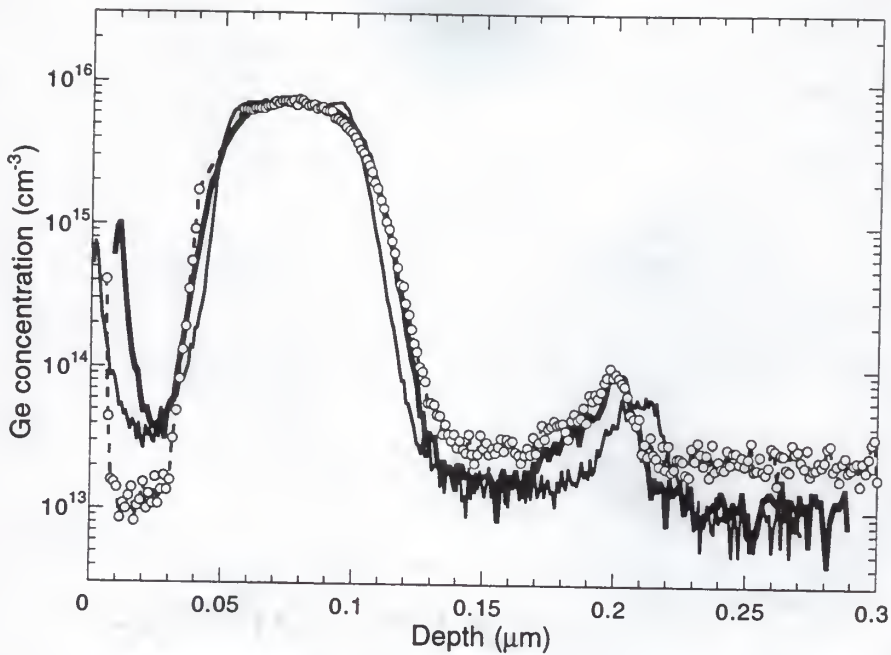


Figure 3-14. Comparison of Ge SIMS profiles in inert, oxidizing and nitriding ambients for SQW/MBE. Sample annealed at (a) 900 °C for 330 min in inert and oxidizing ambient and (b) 1200 °C for 2 min in all three ambients.

therefore diffusion is temperately retarded under interstitial supersaturation. This leads to the conclusion that interstitials play a minimal role in diffusion at all temperatures and at high temperature, injected interstitials may even combine with vacancies, reducing the vacancy concentration and retarding vacancy-dependent diffusion.

The activation energy of $5.27 \text{ eV} \pm 0.11$ (SQW/MBE) calculated for interdiffusion in oxidizing ambient is the first activation energy reported for $\text{Si}_{1-x}\text{Ge}_x/\text{Si}$ interdiffusion under interstitial injection. This activation energy is similar to that in inert ambient and reinforces the belief that interstitials do not have a significant affect on the interdiffusion process.

The activation energy of $3.27 \text{ eV} \pm 0.10$ calculated for the interdiffusion in nitriding ambient is the first activation energy of interdiffusion under vacancy injection reported for a $\text{Si}/\text{Si}_{1-x}\text{Ge}_x$ SQW. This activation energy is approximately 2 eV lower than that for diffusion in inert ambient as well as oxidizing ambient. At anneal temperatures 1100 and 1200°C , the diffusion profiles in a nitriding ambient show significant retardation compared to diffusion profiles in inert and oxidizing ambients (Figure 3-14b). Diffusivities extracted are much lower and not within error of those for inert and oxidizing ambients (Figures 3-2 and 3-3). This indicates that interstitials are the dominant diffusing species and that injected vacancies recombine with intrinsic interstitials to lower the interstitial concentration and retard diffusion. These results are opposite to those found from oxidizing experiments, which predicted that *vacancies* are the dominant diffusion

species and injected interstitials recombine with the vacancies to retard diffusion. Which experiment gives the correct results or how can the two experiments be examined together to form an accurate theory of the actual diffusion process? These questions are addressed in Section 3.5.4.

3.5.2 Diffusivities of Partially-relaxed Structures

Comparison of the Ge diffusivity in initially fully strained SQW structures and initially partially relaxed structures shows that the value is the same in both strain states, in inert, oxidizing, and nitriding ambients, within error. The diffusivities in inert ambient, given in Table 3-3, are plotted versus temperature in Figure 3-15. Diffusivities in oxidizing ambient and nitriding ambient show much the same result. Dislocation formation and strain relaxation seem to have an insignificant effect on Ge diffusion in $\text{Si}/\text{Si}_{1-x}\text{Ge}_x/\text{Si}$ SQWs in this case. This is supported, in some respects, by an investigation by Kuo *et al.* [Kuo95], who found that there is no relation between boron diffusion and strain in $\text{Si}_{1-x}\text{Ge}_x$. This led them to surmise that the equilibrium interstitial concentration is independent of strain.

There are some issues, however, which need to be addressed in future work. At 1200 °C, the initially fully strained structure has a diffusivity in inert ambient that is not within error of the values determined for the partially relaxed structures. This divergence between fully strained and partially relaxed values does not occur at any other temperature. This may just be a one-time anomaly in the data, but further studies should be done at this high temperature to confirm this result.

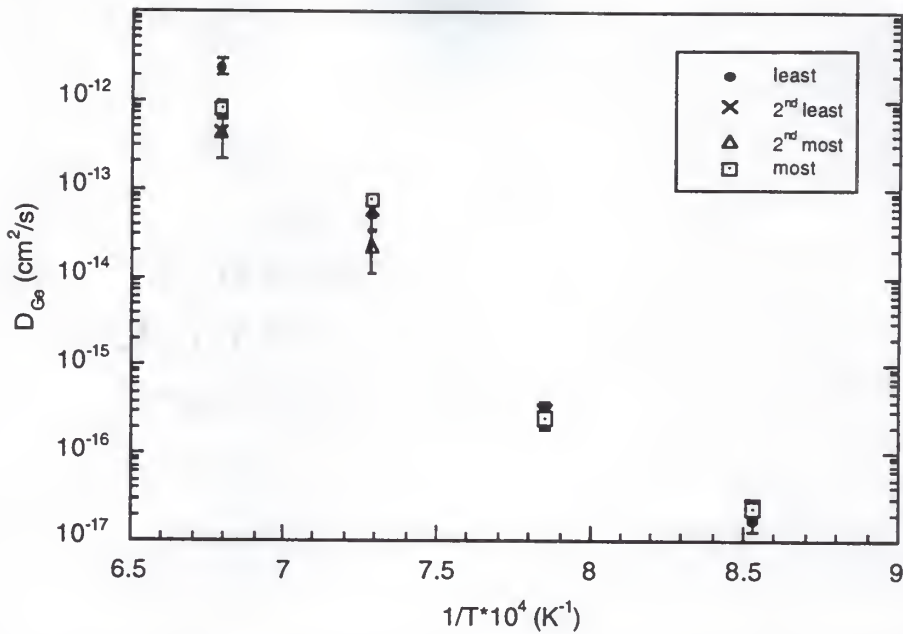


Figure 3-15. Comparison of Ge diffusivities of partially relaxed structures in inert ambient.

As explained in Section 3.4.2, the initial profile used in simulations was the experimentally determined SIMS profile from samples annealed from a time of 0 to t_{init} . The final profile used to extract the diffusivity was the experimentally determined SIMS profile from samples annealed from a time of 0 to t_{final} . The total time of anneal simulated in FLOOPS, t_{anneal} , was $t_{\text{final}} - t_{\text{init}}$. It is ultimately desired that, in future work, the final profile used to extract the diffusivity will be the experimentally determined SIMS profile from samples previously annealed from 0 to t_{init} , which are subsequently annealed from a time of 0 to t_{anneal} . For example, the SIMS profile of a sample annealed at 900 °C from 0 to 330 min, known as Sample 1, was used as the initial partially relaxed profile. In FLOOPS, this profile was annealed for 650 min

and fit to the SIMS profile determined from a sample annealed at 900 °C from 0 to 980 min, known as Sample 2. In future work, a simulated anneal will be performed on the initial profile (Sample 1) for 650 min and fitted to a SIMS profile of Sample 1 further experimentally annealed at 900 °C for 650 minutes. While it is currently unknown whether there will be any difference in diffusivity values between the two approaches, this second method will more accurately reflect the simulations being performed.

It is also important to note here that Fang [Fan96] concluded that the degree of $\text{Si}_{1-x}\text{Ge}_x$ relaxation is relatively independent of the number of absorbed interstitials and that the interstitials do not accelerate or hinder the relaxation process.

3.5.3 Misfit Dislocation Effects

It has been shown through XTEM and PTEM results (Section 3.4.3) that, at such high processing temperatures, strain from the sample structure is relieved through misfit and threading dislocation formation. There is then a possibility that during processing in an oxidizing ambient or a nitriding ambient, the injected interstitials or vacancies may be captured by the dislocations. The injected interstitials or vacancies, once captured, can play no role in altering the C_i or C_v value under interstitial or vacancy injection and therefore C_i remains equal to C_i^* or C_v remains equal to C_v^* . The experiment described in Section 3.4.3 was employed to determine whether excess interstitials injected through surface oxidation are captured by dislocations or travel through the dislocated layers unimpeded.

Qualitatively, at all anneal temperatures the boron marker layer diffused farther in oxidizing ambient than in inert ambient (Figure 3-5). This result indicates that interstitials are transported through the dislocated Si and $\text{Si}_{1-x}\text{Ge}_x$ layers, and reach the buried B layer to enhance its diffusion. It can therefore be concluded that interstitials injected through the surface oxidation process also are available to aid in the Ge diffusion across Si and $\text{Si}_{1-x}\text{Ge}_x$ layers.

Quantitatively, this conclusion requires further investigation. Using FLOOPS, the simulated profiles and experimental SIMS profiles should fit perfectly if and only if (1) the FLOOPS model of B diffusion in Si is perfect and (2) the dislocations capture no interstitials. The first assumption is incorrect: while the FLOOPS model for B diffusion in Si is the most accurate of published models, it is restricted by the experimental data reported in the literature to date. Differences in FLOOPS predicted profiles and experimental profiles would therefore be expected even in the case of inert diffusion with no point defect capture by dislocations. This deviation can be expressed as $[D_{\text{inert}}(\text{actual})/D_{\text{inert}}(\text{FLOOPS})]$. Additionally, the diffusivity of boron, D_B , only enters into the diffusion equations through the product Dt , so that the deviation can be expressed with respect to the results listed in Table 6 as the ratio $[t_{\text{inert}}(\text{FLOOPS})/t_{\text{inert}}(\text{actual})]$ when simulations are run with the default D_B value, which was done in this experiment. This time ratio represents a 'calibration' of the D^* , indicating the accuracy of the experimental set-up and the simulation model.

In an oxidizing ambient, if no injected interstitials are being captured by dislocations, the ratio $[t_{\text{oxidizing}}(\text{FLOOPS})/t_{\text{oxidizing}}(\text{actual})]$ should be equal to $[t_{\text{inert}}(\text{FLOOPS})/t_{\text{inert}}(\text{actual})]$ such that:

$$\frac{t_{\text{oxidizing}}(\text{FLOOPS})}{t_{\text{oxidizing}}(\text{actual})} = \frac{t_{\text{inert}}(\text{FLOOPS})}{t_{\text{inert}}(\text{actual})} \quad (3-14)$$

which can be written as:

$$\frac{t_{\text{oxidizing}}(\text{FLOOPS})}{t_{\text{inert}}(\text{FLOOPS})} = \frac{t_{\text{oxidizing}}(\text{actual})}{t_{\text{inert}}(\text{actual})} \quad (3-15)$$

which means simply that the enhancement to boron diffusion seen in FLOOPS must equal the actual boron diffusion enhancement. If there is interstitial capture then:

$$\text{enh}(\text{FLOOPS}) > \text{enh}(\text{actual}) \quad (3-16)$$

If all interstitials are being captured then:

$$\text{enh}(\text{actual}) = 1 \quad (3-17)$$

The time of anneals listed in Table 3-4 result in FLOOPS enhancements which are greater than actual enhancements for each anneal temperature. The enhancements predicted by FLOOPS vary from 1.78 to 5.33. This result, along with the fact that enhancement of B diffusion is indeed seen in the SIMS profiles (Figure 3-5), allows the expression:

$$1 < \text{enh}(\text{actual}) < \text{enh}(\text{FLOOPS}) \quad (3-18)$$

to be written. Interstitials are captured but not completely, thus there is an upper bound on the interstitial capture.

Movement of the B marker layer cannot determine the vacancy supersaturation as a result of surface nitridation because it is primarily an interstitial diffuser. Any evidence of retardation of B diffusion can, however, qualitatively show that vacancies are being injected to the extent that they are depleting the interstitial concentration. From the values of $t_{\text{Nit}}/t_{\text{Actual}}$ given in Table 3-4 for 1100 °C, it is apparent that there is slight retardation of the diffusion of the B marker layer, which indicates that vacancies are indeed being injected into the bulk and are traveling to some extent through the $\text{Si}_{1-x}\text{Ge}_x$ layer. Future work with Sb marker layers (Sb is known to diffuse almost entirely via a vacancy mechanism) would allow an quantitative estimate of the vacancy supersaturation under nitriding ambient through similar a method similar to that described above.

Fang [Fan96] also used the presence of misfit dislocations nucleated by an unstably strained $\text{Si}_{1-x}\text{Ge}_x$ layer to determine whether the dislocations act as an interstitial barrier. Boron marker layers were grown in and on either side of a $\text{Si}_{0.80}\text{Ge}_{0.20}$ layer of varying thickness and the resulting samples were annealed at 850 °C in either an inert or dry O_2 ambient, much like the experiment performed above. For the thin layers, including the 50 nm layer similar to that used in this thesis, boron diffusivity was equivalent for the surface and buried B marker layers in inert ambient. Under oxidizing ambient, the surface marker layer diffused much more than the buried

marker layer. Fang concludes that under interstitial supersaturation, dislocations act as interstitial sinks, while under inert ambient they do not.

Kuo *et al.* [Kuo95] also examined the effects of oxidation upon diffusion of boron marker layers in Si/Si_{1-x}Ge_x/Si structures similar to those used in Fang. Unlike the results of Fang, they found that a thin Si_{1-x}Ge_x layer does not interfere with the motion of interstitials. In particular they investigated a highly unstable structure that had a Si_{0.70}Ge_{0.30} layer that was 53nm thick, and saw no difference in oxidation enhancements between the surface and buried B marker layers. Fang discussed this study and offered no explanation for the conflicting results.

It is concluded from this experiment, with consideration of the results presented by Fang and Kuo *et al.*, as well as those of the partially relaxed structures (Section 3.5.2), that a portion of interstitials injected during surface oxidation travel throughout the Si_{1-x}Ge_x layer and beyond. The remaining excess interstitials are captured by dislocations. This merely means that the f_i estimated in this work is a lower bound for the fraction of Ge diffusion occurring via interstitials. This also supports the possibility discussed in Section 3.5.1 that dislocations alter C_i/C_i^* and C_v/C_v^* ratios. In the next section the boron marker layer results will be used to give a best estimate of the C_i/C_i^* and C_v/C_v^* ratios for the SQW structure investigated in this chapter. It is recommended, however, that future work with pseudomorphic structures be done to determine if there is any difference between D_{Ge} of

dislocated and dislocation-free structures and whether f_i is, in fact, greater than indicated by oxidation experiments.

3.5.4 Fractional Interstitial Components from Marker Layer Experiments

In Section 3.4.4 it was suggested that the measured D^* values represented diffusion which was severely altered by dislocations and this might account for the inability to estimate an f_i from nitride experiments using the Pair model. The inert diffusivities, D^* , calculated using the method described in Section 3.4.4 were different from those measured in Section 3.4.1. The higher bound of C_v/C_v^* produced diffusivities which were lower than the measured values while the lower bound of C_v/C_v^* produced diffusivities which were higher. In all cases, however, the calculated values were within error of the measured values. It could be concluded that the dislocations had a negligible effect on the Ge diffusivity in inert ambient and that Equation 3-8 should have been able to accurately estimate an f_i using the measured D^* values.

It was alternately suggested in Section 3.4.4 that C_i/C_i^* and C_v/C_v^* could be different in the dislocated SQW/MBE in all ambients from the established values for silicon under normal intrinsic, interstitial supersaturation and vacancy supersaturation conditions. The calculated C_i/C_i^* values given in Tables 3-5 and 3-6 were indeed different, and in most cases lower, than the generally accepted values [Pac90, Pac91] for intrinsic and interstitial supersaturation conditions. Both intrinsic and injected interstitials were captured by the dislocations, altering both C_i/C_i^* and C_v/C_v^* . A general result

of the B marker layer analysis was that the lower bound for C_v/C_v^* seemed to result in C_i/C_i^* values that were more physically reasonable than those resulting from the higher bound. This is most apparent at 1200 °C where the limit of $C_v/C_v^*=1$ could provide no reasonable results. It could be said that the point defect balance is governed by the relation $C_i C_v = C_i^* C_v^*$.

This conclusion was then be used to estimate f_i values for diffusion in SQW/MBE. The lower bound of C_v/C_v^* and the corresponding C_i/C_i^* values resulted in similar f_i values of 0.127 and 0.148 for 900 and 1000 °C, respectively. The values dropped significantly at 1100 °C and 1200 °C to approximately 0.01 and 0.03, respectively. It would seem that there is a significant change in the respective contributions of interstitial and vacancy point defects between 1000 and 1100 °C.

The only other estimate of f_i determined from oxidation studies was made by Cowern *et al.* [Cow96], who reported an f_i value of 0.220 at 875 °C. While the value of Cowern *et al.* is greater than values estimated at 900 °C from this work, it is reasonably similar and corroborates a diffusion mechanism dominated by vacancies.

The method employed with success to the oxidation experiments to determine f_i did not result in equal success when applied to the nitridation experiments. As stated in Section 3.4.4, the D_{Ge}^{Nit}/D^* ratios used in Equation 3-8 were consistently too small to extract f_i values that were less than one, regardless of the bounds used for C_v/C_v^* . The problem of significant retardation seen in all nitriding profiles remains unresolved. Diffusion

dominated by vacancies, as predicted by the oxidation experiments, would be expected to show large enhancements under vacancy supersaturation. The boron marker layer experiments indicated that vacancies were being injected under nitriding ambient and should have enhanced the diffusion of the Ge. A possible explanation for this contradictory behavior is that stress effects at the nitride/silicon interface near the $\text{Si}_{1-x}\text{Ge}_x$ layer, which are not present at the depths of the B marker layer, contribute to this anomalous behavior of the diffusion Ge. This possibility needs to be investigated further in future work.

3.6 Conclusions

The experimental results discussed above have provided considerable contributions to the knowledge of Ge diffusion behavior in $\text{Si}_{1-x}\text{Ge}_x/\text{Si}$ single quantum well structures. The diffusion model used in FLOOPS simulations, while employing several simplifying assumptions, proved to be a satisfactory first effort at predicting Ge diffusion behavior. The diffusion coefficient appeared to be concentration-independent, however, further studies need to be done to verify this conclusion. Diffusivities extracted from profiles obtained over a wide range of anneal times and temperatures showed the Ge diffusivity to be time-independent. Interdiffusivity also seemed to be independent of growth method, as structures grown by both vapor phase epitaxy or molecular beam epitaxy exhibited almost identical diffusion behavior.

Diffusivities extracted in an inert ambient at low temperature agreed well with previously reported values. A major contribution of this work was to extend the anneal temperature regime beyond 1000 °C for the first time, providing diffusivity values for temperatures up to 1200 °C. An activation energy of diffusion of $5.87 \text{ eV} \pm 0.14$ was extracted, which is much higher than previously reported values. This investigation, however, covered a larger temperature range and provided diffusivities spanning five orders of magnitude, therefore, the extracted activation energy could be considered more comprehensive than any previously reported.

For the first time, diffusivities extracted under interstitial injection conditions were reported, with a resulting activation energy for diffusion of $5.27 \text{ eV} \pm 0.11$. No significant enhancement or retardation of Ge diffusion was seen in oxidizing ambient when compared to inert ambient. Also for the first time, diffusivities extracted under vacancy injection conditions were reported, with a resulting activation energy for diffusion of $3.27 \text{ eV} \pm 0.10$. Values of f_i of approximately 0.10 at the lower temperatures and 0.02 at the higher temperatures were estimated from oxidizing experiments, however, f_i could not be estimated from nitriding experiments, possibly due to stress effects originating at the nitride/silicon interface. It was concluded that C_i/C_i^* and C_v/C_v^* ratios were affected by material properties.

Two experiments were performed to investigate the effect of strain and strain relief on Ge diffusivity as well as excess point defect concentrations in $\text{Si}_{1-x}\text{Ge}_x/\text{Si}$ structures. Initially partially relaxed structures showed no

difference in diffusion behavior when compared to initially fully strained structures. This result seems to indicate that strain state does not affect Ge diffusivity. Further investigations involving pseudomorphic structures is needed to confirm this conclusion. Finally, a portion of injected excess interstitials proved to be captured by misfit dislocations, however enhancement of boron marker layer diffusion under oxidizing ambient compared to inert ambient established that a modest amount of excess interstitials are available to participate in the diffusion process.

CHAPTER 4

BEHAVIOR OF ANNEALED ASYMMETRICALLY STRAINED Si/Si_{1-x}Ge_x SUPERLATTICES WITH Si_{1-x}Ge_x BUFFER

A basic requirement for any optical application of a material is its transparency in the near infrared (IR) region, at wavelengths of $\lambda=1.3\mu\text{m}$ and/or $\lambda=1.55\mu\text{m}$. This basic condition is met by silicon and can also be met by Si_{1-x}Ge_x through material engineering. In properly designed quantum wells (QWs), absorption results in photodetection and the QW absorption can be used for IR detection. There has been growing interest in Si-Ge for applications in optics such as photodetectors, waveguides and photodiodes [Qas98, Eng97]. Most of these devices use thin, periodic Si_{1-x}Ge_x and Si layers in superlattice form. The bandgap for absorption in the 1.3 to 1.55 μm range can be obtained with Ge fraction $x>0.25$ in a single strained alloy layer. However, critical thickness for these large Ge fractions is small and sufficiently thick strained layers without misfit dislocations are currently impossible to grow. This difficulty is overcome by using a Si_{1-x}Ge_x/Si superlattice, as the thin Si_{1-x}Ge_x layers are more stable even for large values of Ge fraction because the *average* value of x is not large. In particular, when Si_{1-x}Ge_x and Si layers are grown on a Si_{1-y}Ge_y substrate such that the Si layers are under tensile strain, the conduction band offset is large and n type quantum wells (electron confinement in the conduction band) can be formed which

cause absorption and lead to photodetection. In this chapter results and discussion of diffusion studies performed using this n type quantum well structure are presented.

Thermal stability of these lattice-mismatched SL heterostructures is a critical issue because high-temperature processing steps are often unavoidable during optical device fabrication. Thermal treatment can result in interdiffusion as well as strain relaxation through the formation of dislocations. Any smearing of interfaces due to Ge segregation during the growth and processing of the SLs can lower the transition energy significantly [Fuj92]. As a consequence, the electronic and optical properties of the device structure, such as band alignment, may change, severely degrading the device performance [Zhu97].

Interdiffusion of $\text{Si}_{1-x}\text{Ge}_x/\text{Si}$ asymmetrically strained superlattice (ASL) material in inert, oxidizing, and nitriding ambients over a temperature range 850 to 1000 °C has been investigated. Thermal processing in all three ambients over the same temperature range has allowed estimation of diffusivity values for interdiffusion of $\text{Si}_{0.85}\text{Ge}_{0.15}/\text{Si}$ superlattice material with $\text{Si}_{1-x}\text{Ge}_x$ buffer under interstitial and vacancy supersaturation as well as under inert conditions.

4.1 Growth Parameters and Structure

Test structure SL/SiGe was grown using an ASM Epsilon 1 vapor phase epitaxy reactor at a temperature of 700 °C. As shown in Figure 4-1, the structure consists of a lightly p-doped (100) Si substrate with an undoped 100

nm $\text{Si}_{0.85}\text{Ge}_{0.15}$ buffer, followed by 15 periods of 6 nm $\text{Si}_{0.85}\text{Ge}_{0.15}$ and 12 nm Si. The $\text{Si}_{0.85}\text{Ge}_{0.15}$ layers were grown using dichlorosilane, GeH_4 (germane), and H_2 as the carrier gas. The silicon layers were grown at a rate of 5.0 nm/min while the $\text{Si}_{0.85}\text{Ge}_{0.15}$ layers were grown at a rate of 18.8 nm/min. The Ge concentrations of both the buffer and superlattice layers were verified by Rutherford Backscattering Spectroscopy (RBS) and the layer thicknesses were verified by cross-sectional Transmission Electron Microscopy (XTEM).

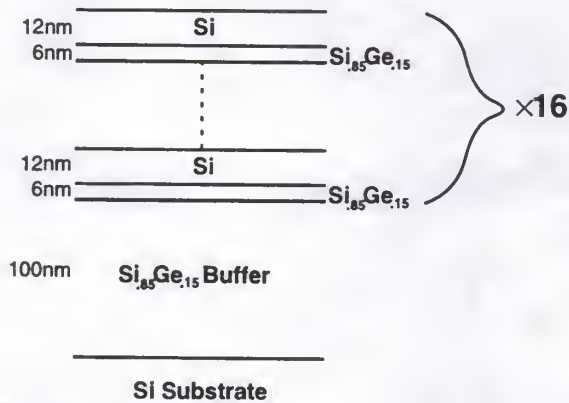


Figure 4-1. Schematic of sample structure SL/SiGe.

The Ge depth versus concentration profiles for as-grown and annealed samples were determined by Secondary Ion Mass Spectroscopy (SIMS) using a Perkin Elmer PHI 6600 quadrupole analyzer with a 6 kV oxygen beam. The profile depth scales were determined from Tencor Alpha-Step 500 surface profiler measurements of the SIMS sputtered craters.

4.2 Strain State

The diffusion coefficient for $\text{Si}_{1-x}\text{Ge}_x/\text{Si}$ has been thought by some investigators to be a sum of strain and composition contributions [Cow96]. If this theory is indeed true, it is important to completely determine the strain state of a system under investigation in order to correctly interpret its diffusion behavior. Initial characterization using SIMS, TEM and RBS enables the general structure and composition of a system to be defined. High Resolution Xray Diffraction (HRXRD) and FLOOPS together provide more specific quantitative data which can correlate change in strain and diffusivity. This progression of characterization techniques was used in this study to first define the initial structure, composition and strain state of both SL/SiGe and SL/Si (to be discussed in Chapter 5) and second to define the final strain state and diffusion profile after thermal processing of these materials. Ultimately, the diffusion and strain relaxation results determined for the ASL grown on a $\text{Si}_{1-x}\text{Ge}_x$ buffer will be compared to those of the ASL grown on a Si buffer to establish independently the influence of strain distribution on the interdiffusion. The general structure and composition of SL/SiGe as grown have already been discussed, therefore it is important to now consider the particulars of the initial strain state of the structure.

The structure SL/SiGe was originally intended to be a symmetrically strained superlattice (SSL), in which the relaxed $\text{Si}_{1-y}\text{Ge}_y$ buffer layer has an intermediate lattice parameter between those of Si and the $\text{Si}_{1-x}\text{Ge}_x$ SL layers. This results in Si and $\text{Si}_{1-x}\text{Ge}_x$ layers which are alternatingly under tensile and

compressive strain respectively. These equal amounts of tensile and compressive strain theoretically offset each other and result in a structure which is essentially strain-free and therefore has a theoretically infinite critical thickness. Structure SL/SiGe was also intended to have a 50 nm Si cap layer as protection against oxide growth.

Structure SL/SiGe, however, was found through RBS characterization to have a $\text{Si}_{1-y}\text{Ge}_y$ buffer layer with the same Ge content as the $\text{Si}_{1-x}\text{Ge}_x$ SL layers, i.e. $y=x$ (Figure 2-14). Structure SL/SiGe was then considered to be an asymmetrically strained superlattice (ASL) because the Si layers were in tensile strain and the $\text{Si}_{0.85}\text{Ge}_{0.15}$ layers were unstrained with respect to the $\text{Si}_{0.85}\text{Ge}_{0.15}$ buffer layer. Also, it was determined from SIMS and XTEM analysis that SL/SiGe lacked the intended 50 nm Si cap layer. However, for the oxidation times and temperatures employed, the top 12 nm Si layer was considered adequate protection against the possibility of oxide growth into the topmost $\text{Si}_{1-x}\text{Ge}_x$ layer.

There is a finite critical thickness which is approximated by the critical layer thickness of a single alloy layer with the same volume-averaged Ge composition as described in Section 2.1. The average Ge content, x_{av} , is determined by:

$$x_{av} = \frac{x d_{\text{SiGe}}}{d_{\text{SiGe}} + d_{\text{Si}}} \quad (4-1)$$

where x is the Ge composition in the $\text{Si}_{1-x}\text{Ge}_x$ layer, d_{SiGe} is the thickness of the $\text{Si}_{1-x}\text{Ge}_x$ layers and d_{Si} is the thickness of the Si layers. Using this equation, the

Ge concentration, averaged over the entire thickness of the multilayers, of SL/SiGe was $x=0.05$. This created a 'bulk' lattice constant of 0.5441 nm, leading to a lattice mismatch with the $\text{Si}_{0.85}\text{Ge}_{0.15}$ buffer of 0.18%. The critical layer thickness, h_c , of an uncapped $\text{Si}_{1-x}\text{Ge}_x$ layer with a lattice mismatch, f_m , of 0.0018, is approximately 80 nm [Jai93]. The total thickness of the 'pseudo-epilayer' of structure SL/SiGe was 270 nm which was more than three times the critical layer thickness. High temperature thermal treatment was expected to cause relaxation through significant misfit dislocation generation.

4.3 Processing

All samples were processed in an AG Associates Heatpulse 2101 rapid thermal processor (RTP), the details of which can be found in section 3.2.1. Initial experiments with structures SL/SiGe and SL/Si employed the diffusivities determined from the single quantum well experiments in Chapter 3. The resulting diffusion lengths after both furnace and rapid thermal anneals were much too large; the structures had essentially annealed to one average alloy composition, with no remaining wells in evidence. It was concluded that, for the thickness of wells in structures SL/SiGe and SL/Si, anneal temperatures and times must be lowered relative to the SQW experiments. While anneal times were much too short to employ furnace anneal, some anneal times were just beyond the reliability for RTP. The longer SL anneals performed in the RTP were therefore pushing the limits of the processing technique and future experiments should be done to confirm the reliability at these times.

Before annealing, the test wafer was cut into 1 x 1 cm pieces which were cleaned using a regimen of deionized water, $\text{H}_2\text{SO}_4\text{:H}_2\text{O}_2$ (1:2) and $\text{H}_2\text{O}\text{:HF}$ (10:1) and then dried with N_2 . Samples were rapid thermal processed with all ambient gases (Ar , O_2 , NH_3) flowing at 1.5 slm.

4.4 Simulation of Diffusion

The diffused Ge profiles were analyzed using the FLorida Object Oriented Process Simulator (FLOOPS) [Law96]. Details regarding the FLOOPS simulation program can be found in section 3.3. The model used to simulate SQW diffusion was used to determine diffusivities for structure SL/SiGe as well. Once again, details can be found in Section 3.3.

4.5 Results

4.5.1 SIMS/FLOOPS

The Ge concentrations of the annealed SIMS profiles were standardized with respect to the total Ge concentration of the as-grown profile using the method described in Section 2.3.1. The depth scale of SL/SiGe was standardized by aligning the Ge plateau (Figure 2-14) of the buffer layer of the annealed and as-grown profiles. In each case, the depth scale of annealed samples was shifted no more than 20 nm in one direction. This lateral movement is well within one standard deviation, estimated at 0.05, in relative depth scale error of SIMS [Gos93]. The error in the extracted diffusivity values was determined from the method described in Section 2.3.2.

The extracted diffusivity and enhancement values for structure SL/SiGe annealed in inert, oxidizing, and nitriding ambients are given in Table 4-1. Diffusion occurring in nitriding ambient at 900 °C for 6 min was not investigated and data for these conditions is therefore absent in Table 4-1. It is once again imperative to state here that the diffusivities measured and discussed throughout this chapter represent *effective* diffusivities, and have not been labeled $D_{\text{Ge}}^{\text{eff}}$ for purposes of textual convenience only.

Table 4-1. Extracted diffusivity and enhancement values for SL/SiGe.

T (°C)	time (min)	$D_{\text{Ge}}^{\text{Inert}}(\text{cm}^2/\text{s})$	$D_{\text{Ge}}^{\text{Ox}}(\text{cm}^2/\text{s})$	$D_{\text{Ge}}^{\text{Nit}}(\text{cm}^2/\text{s})$	$f_{\text{enh}}^{\text{Ox}}$	$f_{\text{enh}}^{\text{Nit}}$
850	8	6.70×10^{-17}	2.32×10^{-16}	8.49×10^{-18}	3.46	0.13
900	4	6.80×10^{-17}	4.58×10^{-17}	1.70×10^{-17}	0.67	0.25
900	6	1.23×10^{-16}	4.04×10^{-16}	-	3.28	-
950	3	1.73×10^{-15}	1.31×10^{-15}	2.86×10^{-16}	0.76	0.17
1000	2	1.77×10^{-15}	2.23×10^{-15}	8.96×10^{-16}	1.26	0.51

The values of the diffusivities for structure SL/SiGe as a function of temperature in inert, oxidizing, and nitriding ambients are shown in Figure 4-2. Fitting this data to Arrhenius expressions results in the following equations when the interdiffusion is carried out in inert, oxidizing and nitriding ambients:

$$D_{\text{Ge}}^{\text{Inert}}(\text{SL/SiGe}) = 6.7 \times 10^{-3} \exp(-3.14\text{eV} \pm 0.20/\text{kT}) \text{ cm}^2/\text{s} \quad (4-2)$$

$$D_{\text{Ge}}^{\text{Ox}}(\text{SL/SiGe}) = 7.22 \times 10^{-6} \exp(-2.43\text{eV} \pm 0.19/\text{kT}) \text{ cm}^2/\text{s} \quad (4-3)$$

$$D_{\text{Ge}}^{\text{Nit}}(\text{SL/SiGe}) = 10.8 \exp(-4.07\text{eV} \pm 0.29/\text{kT}) \text{ cm}^2/\text{s} \quad (4-4)$$

This is the first time that activation energies for interdiffusion under interstitial injection and vacancy injection for $\text{Si}_{1-x}\text{Ge}_x/\text{Si}$ superlattice layers with a $\text{Si}_{1-x}\text{Ge}_x$ buffer have been directly determined from experiment.

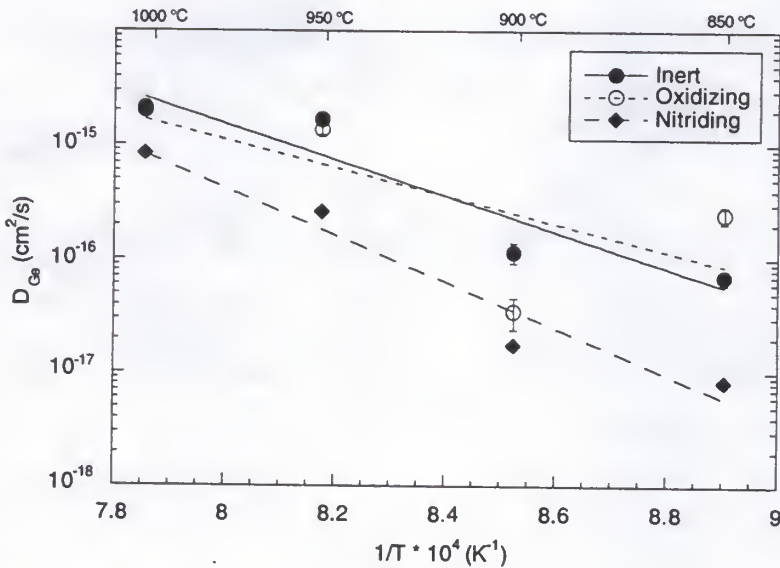


Figure 4-2. Effective Ge diffusivity of structure SL/SiGe as a function of annealing temperature in inert, oxidizing, and nitriding ambients.

The method used in Chapter 3 to estimate fractional interstitial components of diffusion for SQW/MBE could not be applied to SL/SiGe. No SL structure was available with a buried boron marker layer underneath the multiple SiGe/Si layers to estimate point defect concentrations. Therefore, the non-equilibrium values of C_i and C_v specific to dislocated SL/SiGe which occurred as a result of surface oxidation and nitridation could not be estimated. It was considered scientifically pointless to estimate an f_i for diffusion from

either oxidation or nitridation experiments without some knowledge of C_I/C_I^* and C_V/C_V^* for SL/SiGe under the investigated processing conditions.

4.5.2 High Resolution Xray Diffraction

As discussed in Section 4.2, diffusion in $\text{Si}_{1-x}\text{Ge}_x/\text{Si}$ is thought by some to be affected by both strain and composition. HRXRD is a versatile characterization technique which can be used to determine the extent of both diffusion and strain relaxation in heteroepitaxial structures. In Section 4.5.2.1, the technique used in this work to extract diffusivity values for $\text{Si}_{1-x}\text{Ge}_x/\text{Si}$ SLs is described and results are presented. The analysis of the effect of high-temperature processing on $\text{Si}_{1-x}\text{Ge}_x/\text{Si}$ SLs is completed in Section 4.5.2.2 by determining strain relaxation as a function of anneal time. The method of using HRXRD to calculate strain is described and results are presented.

4.5.2.1 Diffusivities

In crystalline materials analyzed by XRD there will be Bragg reflections from the lattice planes resulting in Bragg peaks. A composition modulation, such as is created in a SL material, gives rise to satellites about these Bragg peaks. The satellites about the zero-order reflection are the reflections that can be attributed to the artificial Bragg planes created by the composition modulation. For a sinusoidal composition modulation of wavelength λ , the intensity, I , of the corresponding Bragg reflection should decrease according to:

$$\frac{d}{dt} \left[\ln \left(\frac{I}{I_0} \right) \right] = -\frac{8\pi^2}{\lambda^2} D \quad (4-5)$$

where I_0 is the initial intensity of the satellite peak and D is a composition-independent diffusion coefficient. By measuring the decay in the intensity of the first order satellite with time, the diffusion coefficient can be extracted. This was the procedure used to extract effective diffusion coefficients from HRXRD scans taken of SL/SiGe.

For the purpose of measuring the intensity of the 1st order satellite peak of SL/SiGe, symmetric scans only were needed. As described in Section 2.4.1, symmetric scans are those in which the reflection plane is identical to the substrate/growth plane. The scans of SL/SiGe were performed using the (004) reflection plane, the substrate/growth plane direction. Scans were taken at $\omega \approx 34.5^\circ$ and $2\theta \approx 69.1^\circ$, the values at which the Si(004) peak is at maximum intensity. ω - 2θ scans were taken over a 4° range of ω , with a step size of

Table 4-2. Extracted diffusivities for SL/SiGe using HRXRD.

T (°C)	$D_{\text{Ge}}^{\text{Inert}}(\text{cm}^2/\text{s})$	$D_{\text{Ge}}^{\text{Ox}}(\text{cm}^2/\text{s})$	$D_{\text{Ge}}^{\text{Nit}}(\text{cm}^2/\text{s})$
900	1.33×10^{-17}	1.23×10^{-17}	2.39×10^{-17}
1000	3.21×10^{-16}	-	1.32×10^{-16}

0.00025° and time per step of 4s, resulting in 16001 steps. ω - 2θ scans were taken of the as-grown SL/SiGe structure as well as for samples annealed at 900 °C for 4, 6 and 8 min and at 1000 °C for 1, 2 and 3 min. Examples of resulting scans are shown in Figure 4-3, taken at increasing anneal times for a constant anneal temperature of 1000 °C in inert ambient.

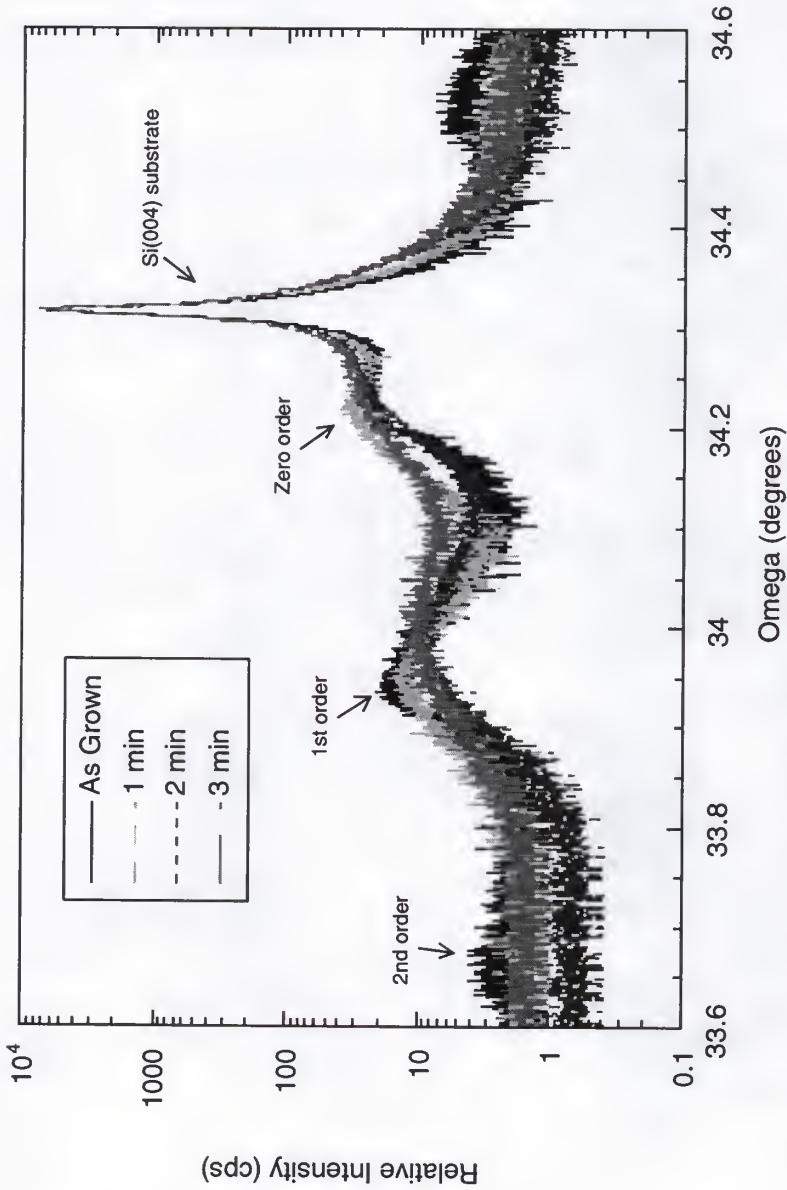


Figure 4-3. X-ray diffractometer scans of the SL/SiGe superlattice peaks about Si(004) with increasing anneal times in inert ambient. The diffusion coefficients have been obtained from the decay of the SL peak marked '1st order'.

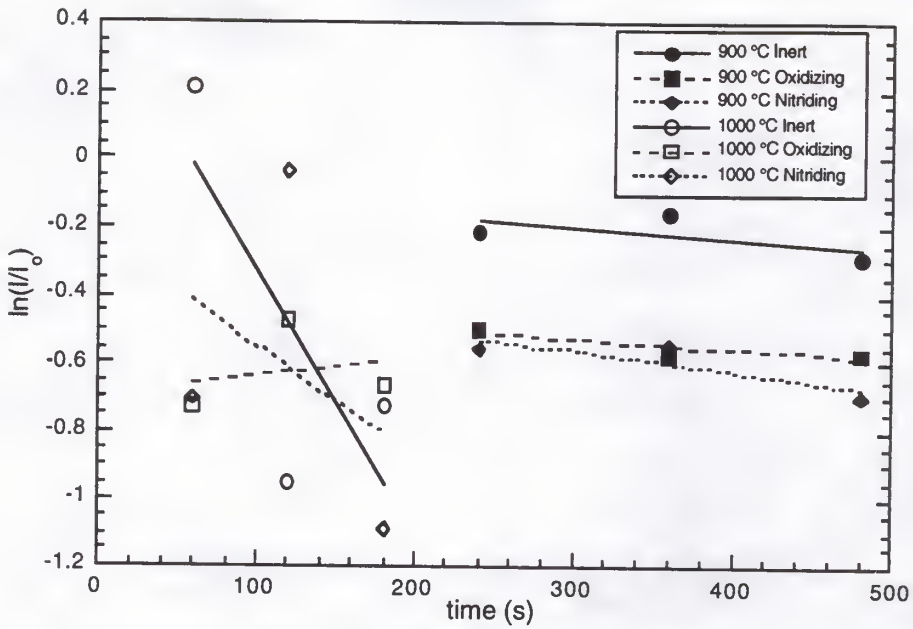


Figure 4-4. Decay of the integrated intensity of the first order superlattice peak about Si(004) as a function of annealing time, temperature and ambient of SL/SiGe.

The decay of the intensity of the first order satellite peak with increasing anneal time resulted in diffusion coefficients extracted using equation 4-5 for anneal temperatures of 900 and 1000 °C in inert, oxidizing, and nitriding ambient (Figure 4-4). These diffusivities are presented in Table 4-2. The absence of a diffusivity for processing in oxidizing ambient at 1000 °C is explained in Section 4.6.2.

The relative intensities of the substrate, zeroth order and satellite peaks can vary from scan to scan, therefore scans must undergo a standardization procedure to enable peak intensities to be compared and used accurately in equation 4-5. The (004) substrate peak is expected to remain constant

regardless of sample thermal processing history, therefore this peak was used to standardize all scans. The ratio of the intensity of the (004) substrate peak in the scans of the annealed samples to the intensity of the (004) substrate peak of the as grown structure was used to standardized the zeroth order and higher order satellite peaks in the scans of the annealed samples. This standardization technique results in a error in intensity measurement that is negligible.

4.5.2.2 Strain relaxation

X-ray double crystal diffractometry allows the accurate determination of the orientation and size of the unit cell of an epilayer compared to the unit cell of its substrate. When a heteroepitaxial layer is grown on a single crystal substrate, two diffraction peaks may be recorded with the diffractometer, one from the substrate and one from the epilayer. The angular separation of these two peaks allows the calculation of the difference in lattice spacing of the two layers and therefore, ultimately, the strain. The method of extraction of lattice constant values is described in detail in Section 2.4.4. This method was employed to extract the change in lattice constants with increasing anneal time of SL/SiGe in inert, oxidizing, and nitriding ambients. The entire $\text{Si}_{1-x}\text{Ge}_x$ multilayer structure was considered in this analysis to be the 'epilayer', as discussed above. The angular separation of this peak and the substrate peak was the main parameter used in calculating the overall strain. In this particular analysis, quantitative calculation of changing lattice constants with anneal time was used as a qualitative indication of changing strain.

A Ge content of $x=0.15$ for the $\text{Si}_{1-x}\text{Ge}_x$ superlattice layers was estimated originally using RBS. However, the peak in HRXRD which was used to calculate strain relaxation represented the *average* epilayer composition of the combined SL multilayers, which, from Section 4.2, was determined to be $x=0.05$. Using Equation 1-1 in section 1.1.1, the fully-relaxed lattice constant of the $\text{Si}_{0.95}\text{Ge}_{0.05}$ cubic unit cell is $a_{\parallel}=a_{\perp}=0.5441$ nm, with a total cell volume of 0.1611 nm³. When the $\text{Si}_{0.95}\text{Ge}_{0.05}$ 'epilayer' is grown on a $\text{Si}_{0.85}\text{Ge}_{0.15}$ buffer layer, the $\text{Si}_{0.95}\text{Ge}_{0.05}$ 'epilayer' is under tensile strain in the parallel direction so that the fully strained value of a_{\parallel} is 0.5461 nm, identical to the lattice constant of the $\text{Si}_{0.85}\text{Ge}_{0.15}$ buffer. At the same time, the unit cell becomes tetragonally distorted such that $a_{\parallel} \neq a_{\perp}$. The total volume of the $\text{Si}_{0.95}\text{Ge}_{0.05}$ unit cell must remain the same, however, so that the fully strained value of a_{\perp} is 0.5402 nm. These theoretical values of a_{\parallel} and a_{\perp} for the epilayer will be compared to those calculated through HRXRD scans of the as grown SL/SiGe structure.

All scans mentioned in this study underwent optimization procedures detailed in Section 2.4.2. Asymmetric scans are adequate to calculate the parallel and perpendicular lattice constants, and, ultimately, the strain. Symmetrical scans can be performed to obtain a perpendicular lattice constant that can be used as a check against the symmetrical scan value. Asymmetric scans were performed in this investigation using the (115) reflection plane. Scans were taken at an ω^- of $\sim 31.5^\circ$ and an ω^+ of $\sim 63.2^\circ$ and a 2θ value of $\sim 95.0^\circ$.

At both ω^- and ω^+ , scans were taken at a rotational angle of -90° and 90° . ω -2 θ scans were taken over a 1° range of ω , with a step size of 0.00025° and time per step of 0.5s for a total of 4001 steps.

Scans of the as grown SL/SiGe structure were taken in order to determine what were considered fully-strained values of the parallel and perpendicular lattice constants. These values gave a good idea of the dimensions of the original unit cell of the epilayer and allowed estimation of the comparative amount of relaxation that occurred through processing. It must be stated, though, that these values are probably not the actual fully-strained values, as TEM micrographs of the as grown structure showed evidence of relaxation through misfit dislocation formation (Section 4.5.3). Scans were limited to two anneal temperatures, 900 and 1000 $^\circ\text{C}$, and two anneal times 6 and 8 min and 1 and 3 min for 900 and 1000 $^\circ\text{C}$, respectively. Scans were taken of samples annealed at these temperatures and times in inert, oxidizing, and nitriding ambients. Table 4-3 presents the resulting $a_{e//}$ and $a_{e\perp}$ values after analysis using the equations given in Section 2.4.4. The error was determined through the minimum resolution in the omega angle, (0.00025°) which is the only parameter used to calculate $a_{e//}$ and $a_{e\perp}$. The error in both $a_{e//}$ and $a_{e\perp}$ was estimated at $\pm 0.0002\text{nm}$.

4.5.3 TEM

The amount of initial relaxation of the structures immediately after growth is determined by the growth temperature, layer thickness, number of

periods, Ge content and the initial condition of the substrate [Iye89]. Upon annealing, the structure will relax to reduce the strain energy. The minimum energy can be attained by compositional modulation of the superlattice or by the generation of misfit dislocations. Both of these mechanisms compete and their respective contributions are dictated by kinetic conditions. Because SL/SiGe is strained and has been shown to have dislocations after growth and before thermal processing, it is important to know at least qualitatively the dislocation density after annealing compared to that of the as grown structure. This will give a qualitative idea of the possible contribution of relaxation through dislocation formation to the diffusivity values calculated in the preceding section.

Table 4-3. Parallel and perpendicular lattice constants of SL/SiGe.

T (°C)	time (min)	Inert		Oxidizing		Nitriding	
		$a_{e//}(\text{nm})$	$a_{e\perp}(\text{nm})$	$a_{e//}(\text{nm})$	$a_{e\perp}(\text{nm})$	$a_{e//}(\text{nm})$	$a_{e\perp}(\text{nm})$
As Grown	-	0.5430	0.5446	0.5430	0.5446	0.5430	0.5446
900	6	0.5436	0.5443	0.5438	0.5442	0.5433	0.5444
900	8	0.5437	0.5443	0.5441	0.5442	0.5433	0.5444
1000	1	0.5434	0.5441	0.5438	0.5441	0.5434	0.5445
1000	3	0.5440	0.5441	0.5440	0.5442	0.5443	0.5440

All plan views were taken with the zone axis of (100) so that the sample is exactly perpendicular to the electron beam, and the (220) reflection was used.

Both plan view and cross section can only provide qualitative defect density data instead of quantitative results in the case of multiple deposited epilayers. In plan view, the image is taken from the top of the sample surface, so the interfaces of every multilayer are not visible. There may be dislocations at interfaces that are buried from view using the plan view perspective that make it impossible to precisely state the number of dislocations present in an entire unit volume. Similarly, it is nearly impossible to get a meaningful estimate of the number of dislocations from cross-sectional view. XTEM only investigates a very small area of the entire sample and is therefore not statistically significant. More importantly, the direction of view used in these and most cross sections is the (110) direction, so that half the dislocation is hidden while the other half lies parallel to the interface, making it impossible to observe whether one or more dislocations are contained within the thickness of the sample.

As discussed in Section 2.2.3, the as-grown SL/SiGe exhibited strain relief through an array of misfit dislocations spaced an average of approximately $0.5\text{ }\mu\text{m}$ apart, however, no threading dislocations were present in cross-section images of the as-deposited structure. As stated above, this does not necessarily mean that there *were* no threading dislocations, there was just no conclusive evidence of them. The precise source of the misfit dislocations is unclear at present but could most likely be due to the high growth temperature of $700\text{ }^{\circ}\text{C}$.

The cross sectional image of SL/SiGe annealed in oxidizing ambient at 850 °C for 8 min exhibits threading and misfit dislocations at the substrate/buffer interface that propagate into the *substrate* layer (Figure 4-5). It is hard to conclude from the image whether the dislocations also propagate into the buffer layer, but it seems that they do not. The minimal view of the $\text{Si}_{1-x}\text{Ge}_x/\text{Si}$ multilayers shows no threading or misfit dislocations. It can be tentatively stated that most of the relaxation occurs in the Si substrate and not in the $\text{Si}_{1-x}\text{Ge}_x$ buffer or $\text{Si}_{1-x}\text{Ge}_x/\text{Si}$ layers. This is probably due to differences in Poisson's ratio and hardness of the two materials.

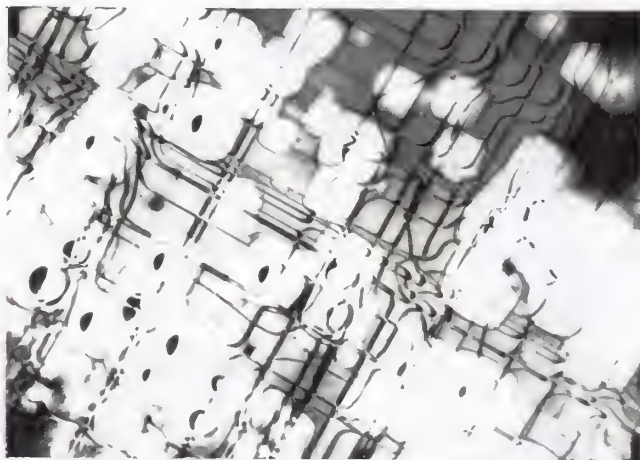
Plan view images were taken of samples annealed at the extremes of the temperatures used in these experiments, 850 and 1000 °C. The misfit dislocation density increased dramatically for SL/SiGe annealed at 850 °C for 8 minutes (Figure 4-6a). The misfit dislocations occurred an average of approximately 2 μm apart. There was also an origination of curved segments not seen in the as-grown materials. These are most likely expanded threading dislocations seen from an overhead perspective. In the micrograph shown in Figure 4-6a there were sample preparation artifacts, light square areas, which can be attributed to the etching process. These artifacts did not, however, affect the ability to examine the dislocation density of the structure. For the sample annealed at 1000 °C for 2 minutes, the dislocation density was very similar to that at 850 °C (Figure 4-6b), and once again, noticeably greater than



50,000x


200nm

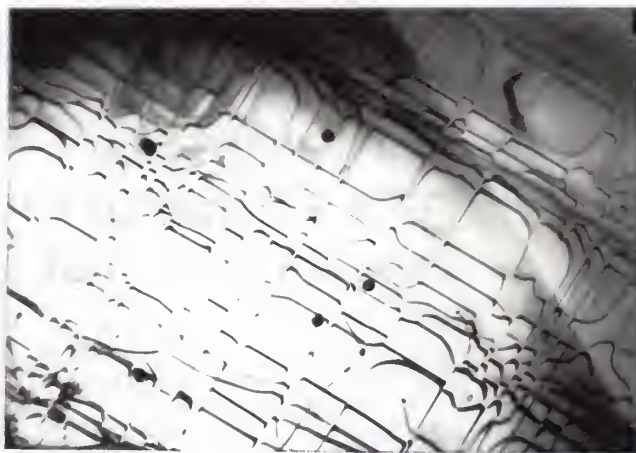
Figure 4-5. Cross sectional view TEM micrograph of structure SL/SiGe after annealing in oxidizing ambient at 850°C for 8 min.



a.

20,000x

500nm



b.

20,000x

500nm

Figure 4-6. Plan view TEM micrographs of structure SL/SiGe after annealing in inert ambient at (a) 850 °C for 8 min and (b) 1000 °C for 2 min.

that of the as-deposited SL/SiGe. From the experiments done in this study, it is difficult to determine exactly what impact this increase in dislocation density had on interdiffusion. These TEM results do suggest that future work needs to be done with structures which are pseudomorphic.

4.6 Discussion

4.6.1 Diffusivities Determined from SIMS and FLOOPS

The FLOOPS diffusion models used in this study were the Fermi and Pair models. The diffusion profiles generated by the Fermi model provided very good fits to the experimentally determined SIMS profiles in the case of anneals performed in inert ambient, as demonstrated in Figure 4-7 for an anneal temperature of 950 °C and an anneal time of 3 min. This indicates that the assumptions made in the Fermi model (Section 3.3), while not completely accurate, provide diffusivity values that reflect the actual diffusion process.

When analyzing the diffusion profiles for structure SQW/MBE and SQW/VPE in Chapter 3, there was a question of whether the profiles were flat in the high Ge concentration region and if so, whether this indicated a concentration-dependent diffusivity (Section 3.5.1). The diffusion profiles determined for SL/SiGe are Gaussian in all ambients and show no flatness in high Ge concentration region of the wells whatsoever at any temperature. It can therefore be concluded that diffusion in structure SL/SiGe is most likely concentration-independent.

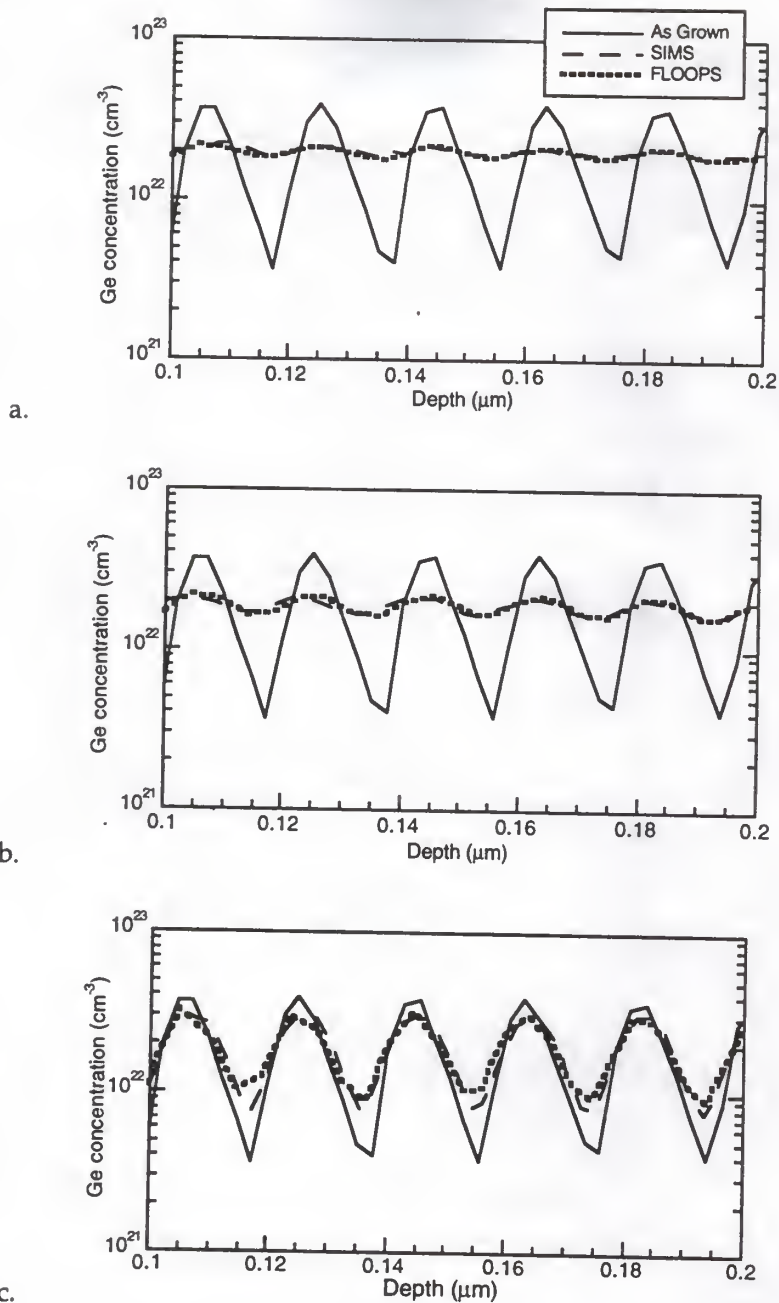


Figure 4-7. Comparison of experimentally determined SIMS profile and FLOOPS profile using the Fermi model for samples annealed at 950 °C and 3 min in (a) inert (b) oxidizing and (c) nitriding ambient.

There has been only one other known study of the diffusivity of Ge in $\text{Si}_{1-x}\text{Ge}_x/\text{Si}$ SL structures with a $\text{Si}_{1-x}\text{Ge}_x$ buffer, annealed in inert ambient. Holländer *et al.* [Hol92] studied interdiffusion of a $\text{Si}_{0.80}\text{Ge}_{0.20}/\text{Si}$ SL with five periods of 10 nm Si and 10 nm $\text{Si}_{0.80}\text{Ge}_{0.20}$ layers. The $\text{Si}_{0.82}\text{Ge}_{0.18}$ buffer layer was grown with a composition which created compressive strain in the $\text{Si}_{0.80}\text{Ge}_{0.20}$ layers that was of equal magnitude to the tensile strain in the Si layers. Thus, the SL investigated by Holländer *et al.* was symmetrically strained. It is also important to note that Holländer *et al.* investigated additional structures with Ge compositions as high as $x=0.68$, but for purposes of direct comparison to the results of this study, these structures will be ignored. The extracted diffusivities (using a Fourier algorithm to fit RBS spectra) from Holländer *et al.* over anneal temperatures 1000 to 1125 °C are plotted in Figure 4-8. The study by Holländer *et al.* differs in temperature range, structure composition, and strain state from that performed using SL/SiGe. The symmetrically strained SL of their study had a different strain state than asymmetrically strained SL/SiGe. The composition difference between the two structures amounts to five percent and SL/SiGe has 10 more periods than that used by Holländer *et al.* The only common anneal temperature studied was 1000 °C. Figure 4-8 illustrates that the diffusion coefficient determined from SL/SiGe at this common temperature is greater than, and not within error of, that reported by Holländer *et al.* The difference in the diffusion coefficients is, however, well below an order of magnitude and could be attributed to the minor differences in composition and layer

thicknesses of the two structures, or to the more significant differences in strain state and diffusivity extraction method. The temperature and diffusivity spans of Holländer *et al.* and this study are almost identical, therefore it is impossible to conclude that one study is more reliable than the other. Furthermore, the diffusivities are similar enough to consider both studies dependable contributions.

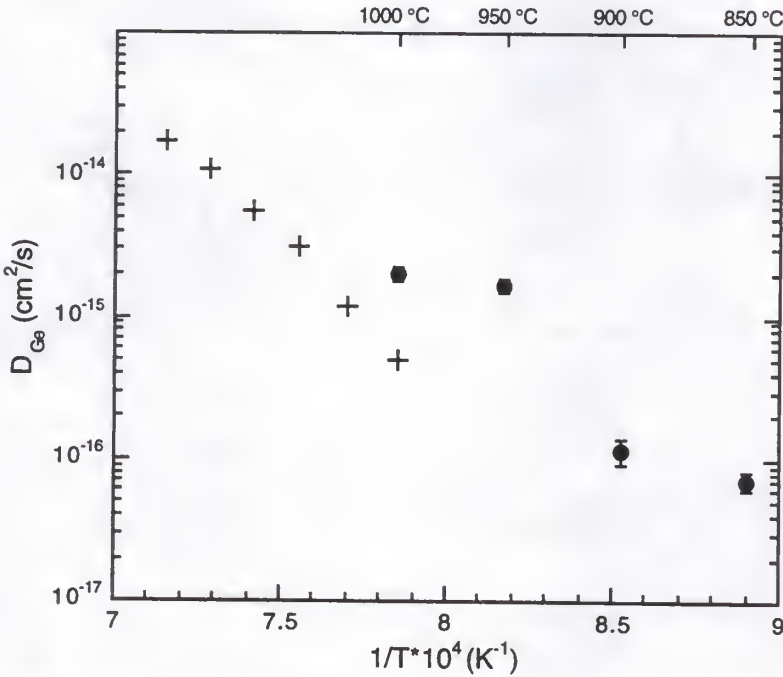


Figure 4-8. Diffusivities of Ge in $\text{Si}_{1-x}\text{Ge}_x/\text{Si}$ SLs with a $\text{Si}_{1-x}\text{Ge}_x$ buffer layer from (+) Holländer *et al.* and (•) this work.

The activation energy of Ge diffusion in $\text{Si}_{1-x}\text{Ge}_x/\text{Si}$ SLs with a $\text{Si}_{1-x}\text{Ge}_x$ buffer layer in inert ambient determined in this study, approximately $3.14 \text{ eV} \pm 0.20$, is lower than, and not within error of, that reported by Holländer *et al.*, $4.5 \text{ eV} \pm 0.20$. Once again, the temperature range of both studies overlaps at

only at an intermediate temperature of 1000 °C. If the Arrhenius expression generated by the data points of Holländer *et al.* is extrapolated to the lower temperatures studied for SL/SiGe, the values are still not within error of those determined for SL/SiGe. The difference in temperature ranges studied cannot, therefore, necessarily account for the disagreement in activation energies. The discrepancy is most likely due to differences in layer thickness, composition, or analysis method, as mentioned above, with neither study considered more reliable than the other.

Time dependence of diffusion in structure SL/SiGe was not thoroughly addressed compared to the investigation of structure SQW/MBE discussed in Chapter 3. Only diffusion at 900 °C was investigated for more than one processing time. At this temperature, diffusivities for anneal times of 4 and 6 min were extracted. The diffusivities given in Table 4-1 for inert ambient are not within error of each other, however they are well within two standard deviations of each other. From this small amount of data, it cannot be stated conclusively whether $\text{Si}_{1-x}\text{Ge}_x/\text{Si}$ SL diffusion in inert ambient is independent of time. Future studies must be done. The diffusivities given in Table 4-1 for oxidizing ambient are not within error of each other and are in fact one entire order of magnitude apart. There is therefore a strong possibility that diffusion is time-dependent in oxidizing ambient. As in the inert ambient case, future studies need to be performed to confirm this preliminary result. In both ambients, this possible time dependence of diffusion is in contrast to the definite time-independence of diffusion in the SQW structures discussed in

Chapter 3. The reason for this difference in behavior is presently not understood and further studies are needed. One possible reason may be a difference in the evolution of strain relaxation with time in the SQW compared to the SL. The bulk $\text{Si}_{1-x}\text{Ge}_x$ layer in the SQW may complete relaxation in the initial phase of the thermal treatment, while the SL relaxation may occur more gradually. The varying relaxation rates may affect diffusion rates. The time dependence of SL/SiGe in nitriding ambient was not investigated.

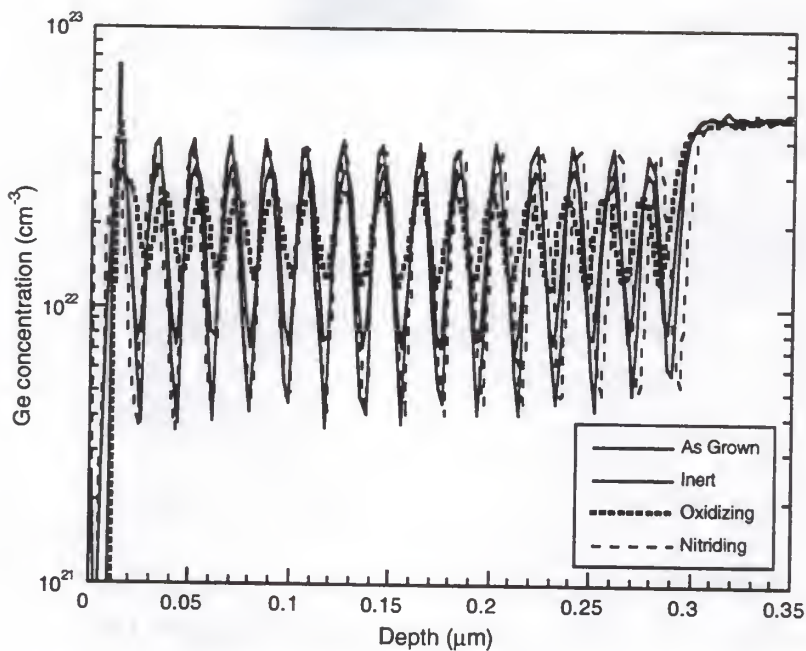
Comparison of diffusion in inert, oxidizing, and nitriding ambients yields interesting conclusions. At the lower temperatures studied, Ge profiles in oxidizing ambient show greater diffusion than profiles in inert ambient (Figure 4-9a). The diffusivity extracted at 850 °C in oxidizing ambient is greater than that in inert ambient and the values are not within error of each other. This indicates that at this low temperature a supersaturation of interstitials results in enhancement of Ge diffusion; interstitial point defects play a measurable role in the diffusion process. This logic, however, is not supported by the diffusivities in inert and oxidizing ambients at 900 °C, where $D_{\text{Ge}}^{\text{Ox}}$ is less than $D_{\text{Ge}}^{\text{Inert}}$ and the values are not within error of each other. It is most likely that, as indicated by the Arrhenius fit to the data, at these lower temperatures, excess interstitial injection has very little effect on diffusion. Diffusivities extracted for both ambients at higher temperatures 950 and 1000 °C are similar and within error of each other, as illustrated in Figure 4-2. Ge depth versus concentration profiles at these temperatures are virtually

identical (Figure 4-9b). At these higher temperatures, diffusion is also unaffected by interstitial supersaturation.

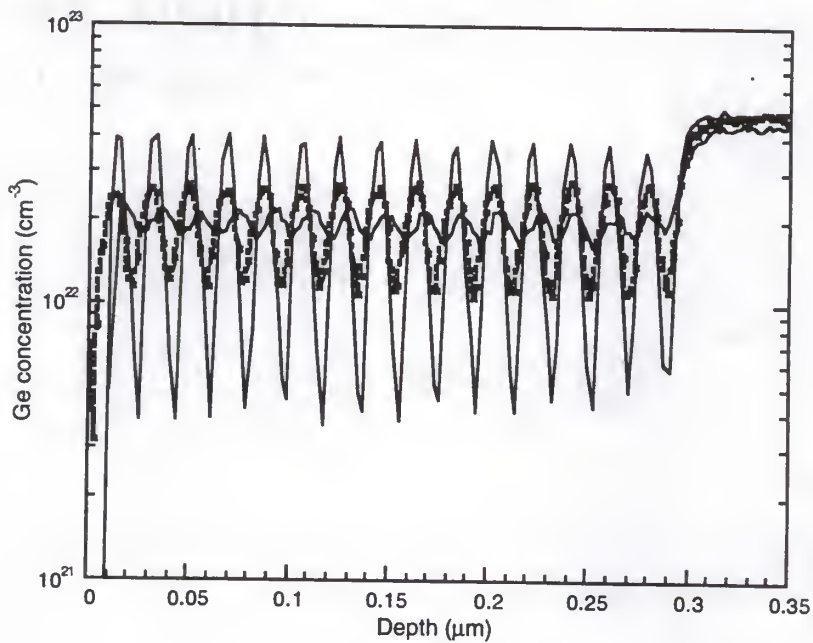
The activation energy of $2.43 \text{ eV} \pm 0.19$ calculated for interdiffusion in oxidizing ambient is the first activation energy of interdiffusion under interstitial injection reported for a $\text{Si}/\text{Si}_{1-x}\text{Ge}_x$ SL with a $\text{Si}_{1-x}\text{Ge}_x$ buffer layer. This activation energy is 0.7 eV less than that for diffusion in inert ambient.

The activation energy of $4.07 \text{ eV} \pm 0.29$ calculated for interdiffusion in nitriding ambient is the first activation energy of interdiffusion under vacancy injection reported for a $\text{Si}/\text{Si}_{1-x}\text{Ge}_x$ SL with a $\text{Si}_{1-x}\text{Ge}_x$ buffer layer. This activation energy is notably higher than that for diffusion in inert ambient as well as in oxidizing ambient. From the activation energies alone, one would expect that oxidation (interstitial injection) would enhance diffusion, while nitridation (vacancy injection) would retard diffusion. Significant retardation was indeed seen in profiles of samples annealed in nitriding ambient, however, little, if any enhancement was observed for samples annealed in oxidizing ambient. It is obvious that activation energies in and of themselves do not provide an accurate picture of the diffusion process.

It is natural to wish to compare the diffusion results of structure SL/SiGe with those of SQW/MBE and SQW/VPE to determine the impact of heterostructure on diffusion behavior. Table 4-4 gives a summary of the major diffusion parameters of both structures for common temperatures



a.



b.

Figure 4-9. Comparison of Ge SIMS profiles in inert, oxidizing, and nitriding ambients for SL/SiGe. Samples annealed at (a) 850 °C for 8 min and (b) 1000 °C for 2 min.

studied. Diffusivities at anneal temperatures of 900 and 1000 °C are approximately one order of magnitude higher for SL/SiGe than for SQW/MBE in both inert and oxidizing ambients. Diffusivities in nitriding ambient cannot be compared since SQW/MBE was not annealed in NH_3 ambient at 900 °C and 1000 °C. The activation energy for diffusion in inert and oxidizing ambients is ~ 2.5 eV lower for SL/SiGe than for SQW/MBE. In nitriding ambient, however, the activation energy of diffusion for SL/SiGe is ~ 1 eV higher than for SQW/MBE.

Table 4-4. Comparison of parameters of interdiffusion of SQW/MBE and SL/SiGe.

	SQW	SL/SiGe
E_A :Inert	5.8 eV	3.14 eV
E_A :Oxidizing	5.0 eV	2.43 eV
E_A :Nitriding	3.0 eV	4.07 eV
$D_{\text{Ge}}^{\text{Inert}}:900^\circ\text{C}$	$2.00 \times 10^{-17} \text{ cm}^2/\text{s}$	$1.16 \times 10^{-16} \text{ cm}^2/\text{s}$
$D_{\text{Ge}}^{\text{Ox}}:900^\circ\text{C}$	$1.00 \times 10^{-17} \text{ cm}^2/\text{s}$	$3.46 \times 10^{-17} \text{ cm}^2/\text{s}$
$D_{\text{Ge}}^{\text{Inert}}:1000^\circ\text{C}$	$3.00 \times 10^{-16} \text{ cm}^2/\text{s}$	$2.01 \times 10^{-15} \text{ cm}^2/\text{s}$
$D_{\text{Ge}}^{\text{Ox}}:1000^\circ\text{C}$	$3.00 \times 10^{-16} \text{ cm}^2/\text{s}$	$2.13 \times 10^{-15} \text{ cm}^2/\text{s}$

Disregarding possible equilibrium point defect concentration effects, what other influences could be the cause of the different diffusion behaviors of SQWs and SLs? One possible reason could be that the average Ge composition of the superlattice layers, $x=0.05$, is substantially lower than the $\text{Si}_{0.85}\text{Ge}_{0.15}$ layer of the SQW. This reason is unlikely, however, because previous studies have reported diffusivities that have increased and

activation energies that have decreased with increasing Ge composition, which are both opposite trends to those seen in Table 4-4. Once again, it seems as if the difference in strain states of the two materials might account for the discrepancies. Interrelated factors such as layer thickness, dislocation formation energy and Si versus $\text{Si}_{1-x}\text{Ge}_x$ buffers may all contribute to the general strain state of each material such that their diffusion behaviors differ drastically.

4.6.2 Diffusivities Determined from HRXRD

Section 4.5.2.1 described the method used to determine diffusivities of periodic SLs from ω -2 θ scans using HRXRD and listed results for SL/SiGe. The relative intensities of the first order satellite peaks did not show the expected trends and therefore the desired diffusion coefficients were difficult to extract. The ω -2 θ scans resulted in standardized first order satellite peaks that did not necessarily decrease progressively in intensity with increasing anneal time (Figure 4-4) as they were expected to do. The zero order peak, which represents the entire sum of epilayers deposited on the substrate, broadened and increased in intensity, which indicated that the periodicity of the SL layers was indeed degrading and the multilayers were stabilizing towards one homogenized layer with an average composition. This zero order epilayer peak shifted towards the angular value of the Si(004) substrate peak, which indicated that the lattice constant of the 'epilayer' was slowly approaching that of bulk Si, and therefore relaxation was occurring.

Confirmation of diffusion and relaxation of SL/SiGe through the behavior of the zero order peak introduces the question of why the first order satellite peak behaved anomalously. The irregularities can most likely be attributed to instrumental issues that consistently arose during HRXRD characterization. Specifically, the maximum intensity of the Si(004) substrate peak was surprisingly low, compared to expected values, for all scans of samples annealed in inert and oxidizing ambients. The low intensity of the substrate peaks resulted in first order peaks that had very small intensities, even when long scans with small angular steps sizes and longer times per step were employed. Upon annealing, the first order peak decreased very quickly with time to intensity levels that were either very small or else were beyond detection. Detection of small changes in intensities of first order peaks with time under these instrumental conditions was therefore questionable. However, the scans of samples annealed in nitriding ambient were performed at a later date, when much higher substrate intensities were obtained, yet there were still anomalies in the resulting data, so this explanation is not necessarily correct.

Figure 4-4 is a plot of the natural logarithm of the standardized intensity of the first order satellite peak versus time. The slope of the decay of the intensity is expected to be negative and is the value to be used in equation 4-5 to extract diffusion coefficients for each temperature. The slopes of the curves for the decrease in intensity of the first order satellite peak for increasing anneal times at 900 °C in inert, oxidizing and nitriding ambients

are negative, making the calculated values D negative, even though for all ambients actual $\ln(I/I_0)$ values do not decay consistently with increasing anneal time. The actual values of $\ln(I/I_0)$ of the first order satellite peak for increasing anneal times at 1000 °C are even more erratic. A linear fit to the data points yields a negative slope for both inert and nitriding ambients, yet the slope of the decay in oxidizing ambient is positive, such that a diffusion coefficient cannot be extracted using Equation 4-5. Diffusivity values can be calculated from all curves except that for 1000 °C in oxidizing ambient, but based purely on the intensity data, no extracted diffusivity can be considered reliable. HRXRD characterization in conjunction with Equation 4-5 shows potential for providing dependable diffusion coefficient data, however much more work needs to be done to refine the instrumental method needed to obtain scans that are reliable.

Having questioned the dependability of the diffusivities obtained through HRXRD, it is still of interest to compare these values with those determined from SIMS and FLOOPS presented in Section 4.5.1. These values are compared in Table 4-5. The diffusivities in all ambients at an anneal temperature of 900 °C are not within error of each other, yet show reasonable agreement. The diffusivities in all ambients at an anneal temperature of 1000 °C are also not within error of each other, and disagree by approximately an order of magnitude. The slope of the decay in intensity of the first order satellite peak with anneal time for SL/SiGe in oxidizing ambient at 1000 °C was found to be positive and therefore could not physically apply to Equation

4-5, and a diffusion coefficient could not be determined. Due to the reasons explained above, the diffusivities extracted using SIMS/FLOOPS are considered to be much more reliable.

Table 4-5. Diffusivities of SL/SiGe extracted from FLOOPS and HRXRD.

T (°C)	$D_{\text{Ge}}^{\text{Inert}}$ (cm ² /s)		$D_{\text{Ge}}^{\text{Ox}}$ (cm ² /s)		$D_{\text{Ge}}^{\text{Nit}}$ (cm ² /s)	
	FLOOPS	HRXRD	FLOOPS	HRXRD	FLOOPS	HRXRD
900	6.80×10^{-17}	1.33×10^{-17}	4.58×10^{-17}	1.23×10^{-17}	1.70×10^{-17}	2.39×10^{-17}
1000	1.77×10^{-15}	3.21×10^{-16}	2.23×10^{-15}	-	8.96×10^{-16}	1.32×10^{-16}

4.6.3 Strain Relaxation Determined from HRXRD

Section 4.5.2.2 described the HRXRD method used to determine the perpendicular and parallel lattice constants of the epilayer which are used to estimate the strain relaxation which occurs in periodic SLs with thermal processing. All results using this method are listed for SL/SiGe in Table 4-3.

The change in the angular separation of the zero order epilayer peak and the Si(004) substrate peak with time did not initially show the expected trend. Because the epilayer is in tensile strain when grown on the $\text{Si}_{1-x}\text{Ge}_x$ buffer, it is expected that progressive relaxation would cause the parallel lattice constant to shrink towards its natural value, while the perpendicular lattice constant would increase towards its unstrained value. The values of $a_{e//}$ were expected to decrease with increasing anneal time, while the values of $a_{e\perp}$ were expected to increase. After calculations were performed using the equations given in Section 2.4.4, the values of $a_{e//}$ were found to *increase*

slightly with time in all ambients, while the values of $a_{e\perp}$ were found to decrease slightly.

Disregarding the possible errors in lattice constant measurement (Section 4.5.2.2), and assuming the evident trends are correct, it is logical to conclude that the strain state of the structure must be redefined to fit the experimental results. One possible way to accomplish this is to consider that the $\text{Si}_{1-x}\text{Ge}_x$ buffer layer contributes to the epilayer peak. The average composition of the 'epilayer' then changes and the Si(004) substrate, not the $\text{Si}_{1-x}\text{Ge}_x$ buffer, becomes the basis for defining the state of the epilayer strain.

If this approach is adopted then the average composition of the 'epilayer' is now $x=0.08$. This creates a 'bulk' lattice constant of 0.5447 nm, leading to a lattice mismatch with the Si(100) substrate of 0.29%. The strained layer grown on the Si(100) buffer would be in compressive strain therefore its parallel lattice constant would increase with increasing relaxation, while the perpendicular lattice constant would decrease.

While this approach yields theoretical values that correspond better with experimentally determined values than those of the original approach, there are still some anomalies. The $a_{e//}$ value does increase with time in inert and oxidizing ambients towards the fully relaxed value, reaching a partially relaxed value of approximately 0.5440 nm for both temperatures. In nitriding ambient at 900 °C, $a_{e//}$ decreases from its original value but remains the same, ~ 0.5433 nm, with increasing anneal time, while at 1000 °C there is obvious relaxation with increasing time. In all ambients the $a_{e\perp}$ value, however,

begins at an amount that is the same as the fully relaxed cubic lattice constant. While this departs from theory, it is still remarkably accurate for the approximations made to obtain the theoretical values. The value decreases only slightly from the as-deposited values, and, with one exception, remains constant with anneal time, for both temperatures and in all ambients. This could be due to shear deformation in the epitaxial layer [Bar78] or distortion in all three lattice constants and further studies are needed. The only exception is in nitriding ambient at 1000 °C for an anneal time of 3 min, where a_{e1} shrinks. This can probably be attributed to error in measurement.

4.7 Conclusions

The experimental results discussed above have provided considerable contributions to the knowledge of Ge diffusion behavior in $\text{Si}_{1-x}\text{Ge}_x/\text{Si}$ asymmetrically strained SL with a $\text{Si}_{1-x}\text{Ge}_x$ buffer. The diffusion model used in FLOOPS simulations, while employing several simplifying assumptions, proved to be a satisfactory first effort at predicting Ge diffusion behavior. The diffusion coefficient exhibited Gaussian, concentration-independent behavior. Diffusivities extracted from profiles obtained over a limited range of anneal times and temperatures showed Ge diffusivity to have a possible time-dependence. Further experiments must be performed to support this conclusion.

A major contribution of this work was to extend the anneal temperature regime below 1000 °C for the first time, providing diffusivity

values for temperatures down to 850 °C. Diffusivities extracted in inert ambient at low temperatures agreed well with previously reported values. An activation energy of diffusion of $3.14 \text{ eV} \pm 0.20$ was extracted, which is considerably lower than the one available reported value of 4.5 eV [Hol92]. Both investigations spanned a similar temperature gradient and therefore both can be considered as reliable in that respect as the other. The difference in the diffusion coefficients is, however, well below an order of magnitude and could be attributed to the minor differences in composition and layer thicknesses of the two structures, or to the more significant differences in strain state and diffusivity extraction method.

For the first time, diffusivities extracted under interstitial injection conditions were reported, with a resulting activation energy for diffusion of $2.43 \text{ eV} \pm 0.19$. No significant enhancement of Ge diffusion was seen in oxidizing ambient when compared to inert ambient at any temperature. This leads to the conclusion that interstitials play a minimal role in diffusion.

For the first time, diffusivities extracted under vacancy injection conditions were reported, with a resulting activation energy for diffusion of $4.07 \text{ eV} \pm 0.29$. Significant retardation of Ge diffusion was seen in nitriding ambient when compared to inert ambient at all temperatures, indicating that diffusion is dominated by interstitials. This contradicted the results of the oxidation experiments.

Plan-view TEM micrographs showed qualitatively that dislocation density increased from the as-deposited value after anneal. However, the

dislocation densities of the annealed samples were approximately constant regardless of anneal time or temperature. This suggests that misfit dislocations are created in the initial stages of relaxation and remain constant with further annealing. Cross-sectional TEM micrographs showed that, due to differences in hardness between Si and $\text{Si}_{1-x}\text{Ge}_x$, most of these misfit and threading dislocations propagated into the Si substrate and Si cap, and *not* into the $\text{Si}_{1-x}\text{Ge}_x$ multilayer region. This conclusion regarding misfit dislocation generation was supported by HRXRD analysis of SL/SiGe strain relaxation. The lattice constants of the SL/SiGe pseudo-epilayer were seen to change upon anneal when compared to the as-deposited values, but remained relatively constant when compared to other annealed samples. Attempts to extract a diffusion coefficient from the intensities of the first order satellite peaks from ω -2 θ HRXRD scans provided values that were unreliable. While characterization through HRXRD seems promising, future work must be done to perfect the experimental technique and diffusion coefficient extraction method.

CHAPTER 5

BEHAVIOR OF ANNEALED ASYMMETRICALLY STRAINED Si/Si_{1-x}Ge_x SUPERLATTICES WITH Si BUFFER

The limitless variations of Si_{1-x}Ge_x/Si superlattice structures enables the synthesis of materials with custom-tailored electronic band structures which can be utilized in a variety of optical applications. The Si_{1-x}Ge_x/Si SL with a Si_{1-x}Ge_x buffer discussed in Chapter 4, which produces n-type wells, is one example of wavefunction engineering. Si_{1-x}Ge_x/Si superlattice layers grown on a Si buffer result in p-type quantum wells which have most of the band offset, and therefore hole confinement, in the valence band. This p-type quantum well structure is easier and less costly to fabricate than the n-type structure, due to its simple Si buffer. It is, therefore, more commonly used in device applications and its interdiffusion behavior has been investigated more thoroughly.

Even in superlattice material, with the Ge composition averaged over many layers to create a more stable structure, strain relaxation through dislocation formation and smearing of interfaces through interdiffusion remain dominant issues in Si_{1-x}Ge_x/Si high temperature processing. The effects of strain and composition are normally coupled, as Ge composition determines overall strain between Si_{1-x}Ge_x and Si layers. Comparing diffusion behavior of Si_{1-x}Ge_x/Si SLs that are identical in every respect but their buffer

layer allows the effects of composition and strain to be decoupled. $\text{Si}_{1-x}\text{Ge}_x/\text{Si}$ multilayers grown on a $\text{Si}_{1-x}\text{Ge}_x$ buffer produces tensile strain in the Si layers and only residual strain in the $\text{Si}_{1-x}\text{Ge}_x$ layers. On the other hand, $\text{Si}_{1-x}\text{Ge}_x/\text{Si}$ multilayers grown on a Si buffer produces only residual strain in the Si layers and compressive strain in the $\text{Si}_{1-x}\text{Ge}_x$ layers. By comparing structures with identical Ge composition, layer thickness and number of periods, the effect of strain state on interdiffusion can be independently determined.

Interdiffusion of a $\text{Si}_{1-x}\text{Ge}_x/\text{Si}$ asymmetrically strained superlattice (ASL) with a Si(100) buffer over a temperature range 850 to 1000 °C in inert, oxidizing, and nitriding ambients has been investigated. Thermal processing in all three ambients over the same temperature range has allowed estimation of the diffusion coefficient of interdiffusion of $\text{Si}_{0.85}\text{Ge}_{0.15}/\text{Si}$ superlattice material with Si(100) buffer under interstitial and vacancy supersaturation as well as under inert conditions. These results have been compared to those reported in Chapter 4 for $\text{Si}_{0.85}\text{Ge}_{0.15}/\text{Si}$ ASLs with a $\text{Si}_{1-x}\text{Ge}_x$ buffer to determine the effect of strain state on interdiffusion.

5.1 Growth Parameters and Structure

Test structure SL/Si was grown using an ASM Epsilon 1 vapor phase epitaxy reactor at a temperature of 700 °C. As shown in Figure 5-1, the structure consists of a lightly p-doped (100) Si substrate with an undoped 100 nm Si buffer, followed by 16 periods of 6 nm $\text{Si}_{0.85}\text{Ge}_{0.15}$ and 12 nm Si and an undoped 50 nm Si cap. The $\text{Si}_{0.85}\text{Ge}_{0.15}$ layers were grown using dichlorosilane (DCS), GeH_4 (germane), and H_2 as the carrier gas. The silicon layers were

grown at a rate of 5.0 nm/min while the $\text{Si}_{0.85}\text{Ge}_{0.15}$ layers were grown at a rate of 18.8 nm/min. The Ge concentrations of both the buffer and superlattice layers were verified by Rutherford Backscattering Spectroscopy (RBS) and the layer thicknesses were verified by cross-sectional Transmission Electron Microscopy (XTEM).

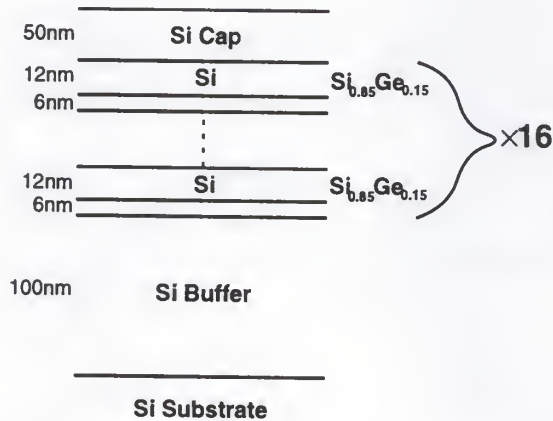


Figure 5-1. Schematic of sample structure SL/Si.

The Ge depth versus concentration profiles for as-grown and annealed samples were determined by Secondary Ion Mass Spectroscopy (SIMS) using a Perkin Elmer PHI 6600 quadrupole analyzer with a 6 kV oxygen beam. The profile depth scales were determined from Tencor Alpha-Step 500 surface profiler measurements of the SIMS sputtered craters.

5.2 Strain State

Structure SL/Si is considered asymmetrically strained because the $\text{Si}_{0.85}\text{Ge}_{0.15}$ layers are in compressive strain while the Si layers are unstrained

with respect to the Si buffer layer. This differs from SL/SiGe in which the Si layers are in tensile strain while the $\text{Si}_{0.85}\text{Ge}_{0.15}$ layers are unstrained with respect to the $\text{Si}_{0.85}\text{Ge}_{0.15}$ buffer layer. There is a finite critical thickness which is approximated by the critical layer thickness of a single alloy layer with the same volume-averaged Ge composition as described in Section 2.1. The average Ge content, x_{av} , is determined by [Kas95]:

$$x_{av} = \frac{xd_{\text{SiGe}}}{d_{\text{SiGe}} + d_{\text{Si}}} \quad (5-1)$$

where x is the Ge composition in the $\text{Si}_{1-x}\text{Ge}_x$ layer, d_{SiGe} is the thickness of the $\text{Si}_{1-x}\text{Ge}_x$ layers and d_{Si} is the thickness of the Si layers. Using this equation, the Ge concentration, averaged over the entire thickness of the multilayers, of SL/Si is $x=0.05$. The critical thickness of a capped layer of $\text{Si}_{0.95}\text{Ge}_{0.05}$ grown on a Si buffer is $h_c \sim 100\text{nm}$ [Jai94]. The total multilayer thickness of structure SL/Si, 288 nm, greatly exceeds this value, therefore misfit dislocations are expected to be present before and after thermal processing.

The cubic unit cell of the $\text{Si}_{1-x}\text{Ge}_x$ can be isolated and used to describe the strain state. A Ge composition of $x=0.15$ results in a lattice constant of 0.5461 nm and a volume of 0.1629 nm^3 for the fully relaxed $\text{Si}_{1-x}\text{Ge}_x$ cubic unit cell (Equation 1-1). Making an approximation which ignores any residual strain in the Si layer, this lattice constant represents a lattice mismatch with the underlying Si layer of 0.55% when fully strained. Assuming tetragonal distortion, the perpendicular lattice constant, a_{\perp} , is 0.5523 nm when fully strained. As the structure relaxes, a_{\perp} decreases while the parallel lattice

constant, $a_{//}$, increases. These values can be measured using high resolution x-ray diffraction (Section 5.5.3), to completely determine the strain state after anneal.

5.3 Processing

All samples were processed in an AG Associates Heatpulse 2101 rapid thermal processor (RTP), the details of which can be found in section 3.2.1. Anneal times and temperatures were identical to those of structure SL/SiGe to enable comparison of results with regard to the effect of strain state. Before annealing, the test wafer was cut into 1 x 1 cm pieces which were cleaned using a regimen of deionized water, $\text{H}_2\text{SO}_4:\text{H}_2\text{O}_2$ (1:2) and $\text{H}_2\text{O}:\text{HF}$ (10:1) and then dried with N_2 . Samples were rapid thermal processed with all ambient gases (Ar , O_2 , NH_3) flowing at 1.5 slm.

5.4 Simulation of Diffusion

The diffused Ge profiles were analyzed using the FLorida Object Oriented Process Simulator (FLOOPS) [Law96]. Details regarding the FLOOPS simulation program can be found in section 3.3. The model used to simulate SQW and SL/SiGe diffusion was used to determine diffusivities for structure SL/Si as well. Once again, details can be found in Section 3.3.

5.5 Results

5.5.1 SIMS/FLOOPS

The Ge concentrations of the annealed profiles were standardized with respect to the total Ge concentration of the as-grown profile using the method described in Section 2.3.1. The depth scale of SL/Si was difficult to standardize because there was no Ge plateau or segregation peak with which to align the as-grown and annealed profiles. The profiles were depth-aligned by matching the depths of the first quantum well peak. In each case, the depth scale of annealed samples was shifted no more than 20 nm in one direction. This lateral movement was well within one standard deviation, estimated at 0.05, in relative depth scale error of SIMS [Gos93]. Even so, minimal variations in sputter rate from sample to sample caused a small amount of increasing misalignment with depth. This misalignment did not hinder the fitting process. The error in the extracted diffusivity values was determined from the method described in Section 2.3.2.

The extracted diffusivity values for structure SL/Si annealed in inert, oxidizing, and nitriding ambients are given in Table 5-1.

Table 5-1. Extracted diffusivity and enhancement values for SL/Si.

T (°C)	time (min)	$D_{\text{Ge}}^{\text{Inert}}(\text{cm}^2/\text{s})$	$D_{\text{Ge}}^{\text{Ox}}(\text{cm}^2/\text{s})$	$D_{\text{Ge}}^{\text{Nit}}(\text{cm}^2/\text{s})$	$f_{\text{enh}}^{\text{Ox}}$	$f_{\text{enh}}^{\text{Nit}}$
850	8	4.00×10^{-17}	1.12×10^{-16}	1.42×10^{-17}	1.80	0.355
900	4	4.58×10^{-17}	4.58×10^{-17}	1.70×10^{-17}	1.00	0.371
950	3	1.73×10^{-15}	1.31×10^{-15}	3.46×10^{-16}	0.76	0.106
1000	2	1.18×10^{-15}	1.70×10^{-15}	1.07×10^{-15}	1.40	0.907

The values of the diffusivities for structure SL/Si as a function of temperature in inert, oxidizing, and nitriding ambients are shown in Figure 5-2. Fitting this data to Arrhenius expressions results in the following equations when the processing was performed in inert, oxidizing, and nitriding ambients:

$$D_{\text{Ge}}^{\text{Inert}}(\text{SL/Si}) = 3.6 \times 10^{-1} \exp(-3.63\text{eV} \pm 0.24/\text{kT}) \text{cm}^2/\text{s} \quad (5-2)$$

$$D_{\text{Ge}}^{\text{Ox}}(\text{SL/Si}) = 2.3 \times 10^{-4} \exp(-2.81\text{eV} \pm 0.21/\text{kT}) \text{cm}^2/\text{s} \quad (5-3)$$

$$D_{\text{Ge}}^{\text{Nit}}(\text{SL/Si}) = 2.7 \times 10^1 \exp(-4.16\text{eV} \pm 0.22/\text{kT}) \text{cm}^2/\text{s} \quad (5-4)$$

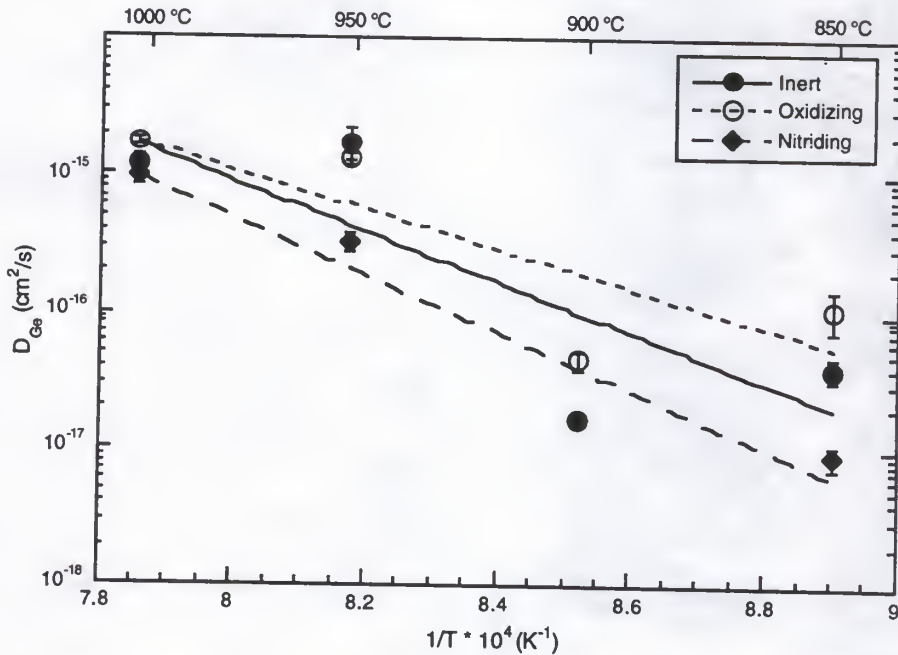


Figure 5-2. Effective Ge diffusivity of structure SL/Si as a function of annealing temperature in inert, oxidizing, and nitriding ambient.

This is the first time that activation energies for interdiffusion under interstitial injection and vacancy injection for $\text{Si}_{1-x}\text{Ge}_x/\text{Si}$ superlattice layers with a Si buffer have been directly determined from experiment.

As stated in Chapter 4 for SL/SiGe, the method used in Chapter 3 to estimate fractional interstitial components of diffusion for SQW/MBE could not be applied to SL/Si. No SL structure was available with a buried boron marker layer underneath the multiple $\text{Si}_{1-x}\text{Ge}_x/\text{Si}$ layers to estimate point defect concentrations. Therefore, the non-equilibrium values of C_i and C_v specific to dislocated SL/Si which occurred as a result of surface oxidation and nitridation could not be estimated. It was considered scientifically pointless to estimate an f_i for diffusion from either oxidation or nitridation experiments without some knowledge of C_i/C_i^* and C_v/C_v^* for SL/Si under the investigated processing conditions.

5.5.2 High Resolution Xray Diffraction

As described in Section 4.5.2, HRXRD characterization provides information about the lattice constants of a crystal structure both before and after thermal treatment. The strain relaxation process resulting from anneal can, therefore, be completely defined. Through alternate analysis, HRXRD can also provide values of the diffusivities of the annealed crystal (Section 4.5.2). The knowledge of the process by which the crystal relaxes enables a more thorough interpretation of the diffusivity data obtained. Lattice constants and diffusivities of SL/SiGe have already been calculated and reported in Chapter 4. Structures SL/SiGe and SL/Si are similar in every

respect except for their original strain state. Applying identical HRXRD experimental method and analysis for structure SL/Si to that performed for SL/SiGe will allow the impact of strain state to be determined directly.

The technique used to extract diffusivity values for SL/Si is identical to that described in Section 4.5.2.1. In Section 5.5.2.1, results for SL/Si are presented. The analysis of the effect of high-temperature processing on SL/Si is completed in Section 5.5.2.2 by determining strain relaxation as a function of anneal time.

5.5.2.1 Diffusivities

For the purpose of measuring the intensity of the 1st order satellite peak of SL/Si, symmetric scans only were needed. The scans of SL/Si were performed using the (004) reflection plane, the substrate/growth plane direction. Scans were taken at $\omega \approx 34.5^\circ$ and $2\theta \approx 69.1^\circ$, the values at which the Si(004) peak is at maximum intensity. ω - 2θ scans were taken over a 4° range of ω , with a step size of 0.00025° and time per step of 4s, resulting in 16001 steps. ω - 2θ scans were taken of the as-grown SL/Si structure as well as for samples annealed at 900 °C for 4, 6 and 8 min and at 1000 °C for 1, 2 and 3 min. These anneal times and temperatures were identical to those used in Chapter 4 for SL/SiGe, in order facilitate direct comparison of diffusion behavior in both structures. Examples of resulting scans of SL/Si are shown in Figure 5-3, taken at increasing anneal times for a constant anneal temperature of 1000 °C in inert ambient.

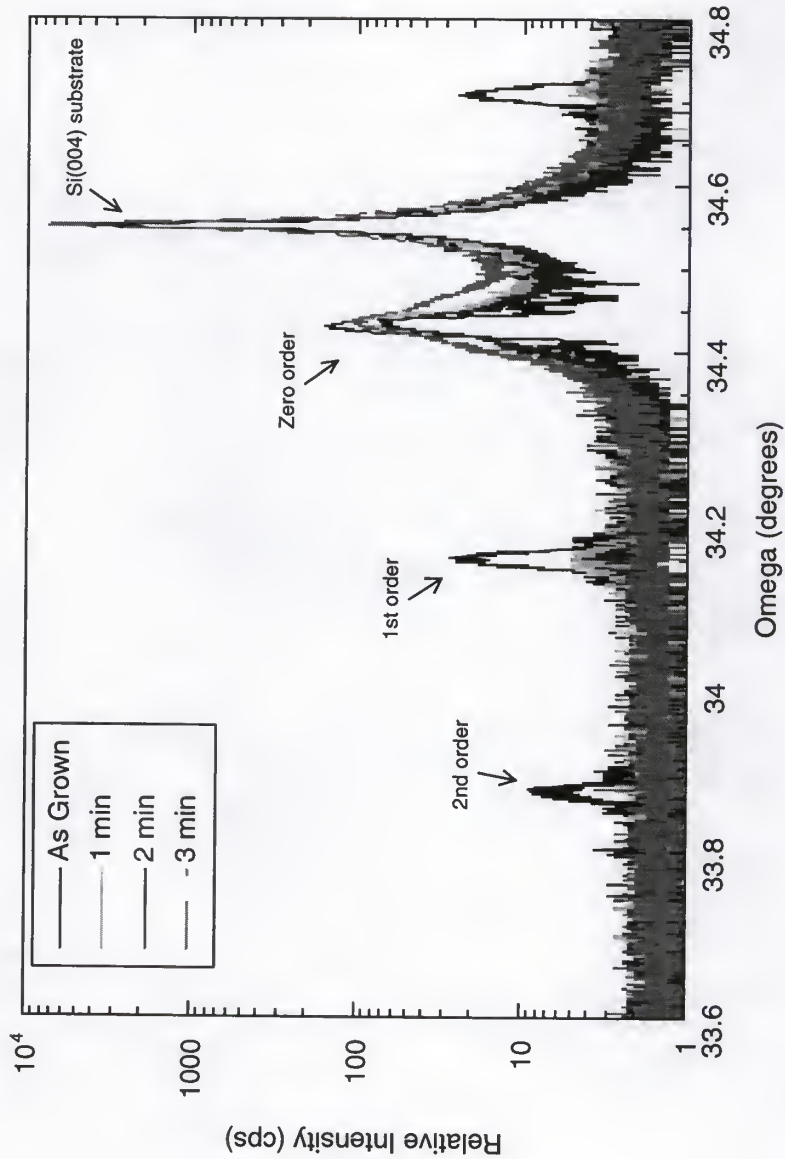


Figure 5-3. X-ray diffractometer scans of the SL/SiGe superlattice peaks about Si(004) with increasing anneal times in inert ambient. The diffusion coefficients have been obtained from the decay of the SL peak marked '1st order'.

The decay of the intensity of the first order satellite peak with increasing anneal time resulted in diffusion coefficients extracted using Equation 5-1 for anneal temperatures of 900 and 1000 °C in inert, oxidizing, and nitriding ambient (Figure 5-4). These diffusivities are presented in Table 5-2. A diffusion coefficient for SL/Si annealed in oxidizing ambient at 900 C could not be extracted because of the positive slope of the decay of the intensity of the first order satellite peak.

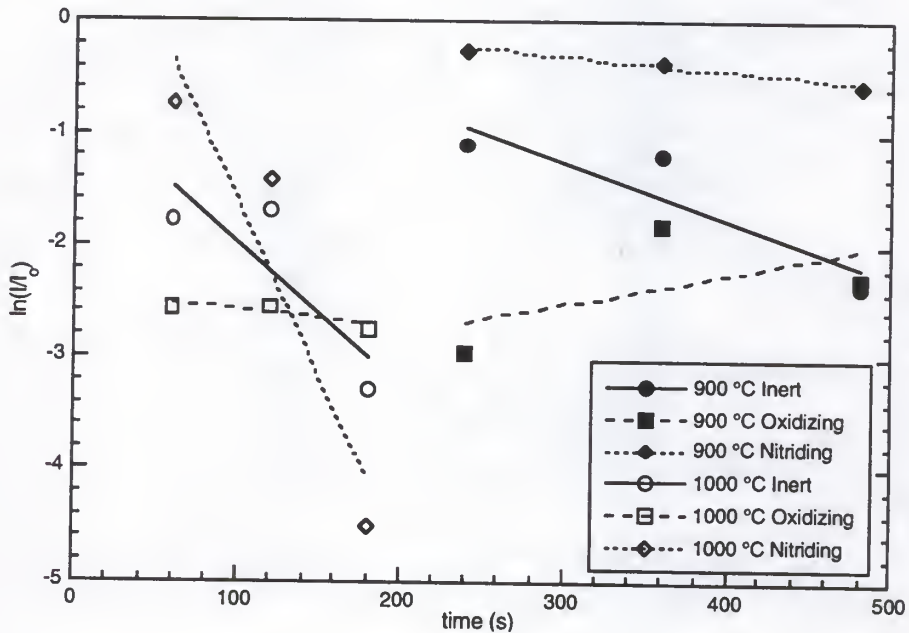


Figure 5-4. Decay of the integrated intensity of the first order superlattice peak about Si(004) as a function of annealing time, temperature and ambient of SL/Si.

Table 5-2. Extracted diffusivity values for SL/Si using HRXRD.

T (°C)	$D_{\text{Ge}}^{\text{Inert}}(\text{cm}^2/\text{s})$	$D_{\text{Ge}}^{\text{Ox}}(\text{cm}^2/\text{s})$	$D_{\text{Ge}}^{\text{Nitr}}(\text{cm}^2/\text{s})$
900	2.13×10^{-16}	-	5.24×10^{-17}
1000	5.17×10^{-16}	6.14×10^{-17}	1.29×10^{-15}

5.5.2.2 Strain relaxation

The method of extraction of strain values is described in detail in Sections 2.4.4 and 4.5.2.2. This method was employed to extract the change in strain with increasing anneal time of SL/Si in inert, oxidizing, and nitriding ambients.

A Ge content of $x=0.15$ for $\text{Si}_{1-x}\text{Ge}_x$ superlattice layers was estimated originally using RBS. As described in Section 4.5.2.2, the peak in HRXRD which was used to calculate strain relaxation represents the *average* epilayer composition of the combined SL multilayers, which was determined to be 0.05. Using Equation 1-1 from Section 1.1.1, the fully relaxed lattice constant of the $\text{Si}_{0.95}\text{Ge}_{0.05}$ cubic unit cell is $a_{\parallel}=a_{\perp}=0.5441$ nm, with a total volume of 0.1611 nm³. When the $\text{Si}_{0.95}\text{Ge}_{0.05}$ 'layer' is grown on a Si buffer layer, the $\text{Si}_{0.95}\text{Ge}_{0.05}$ is compressed in the parallel direction so that the fully strained value of a_{\parallel} is 0.5431 nm. At the same time, the unit cell becomes tetragonally distorted such that $a_{\parallel} \neq a_{\perp}$. The total volume of the $\text{Si}_{0.95}\text{Ge}_{0.05}$ unit cell must remain the same, however, so that the fully strained value of a_{\perp} is 0.5461 nm. These theoretical values of a_{\parallel} and a_{\perp} for the epilayer will be compared to those calculated through HRXRD scans of the as grown SL/Si structure.

All scans mentioned in this study underwent optimization procedures detailed in Section 2.4.2. Asymmetric scans are adequate to calculate the parallel and perpendicular lattice constants, and, ultimately, the strain. Symmetrical scans can be performed to obtain a perpendicular lattice constant

that can be used as a check against the symmetrical scan value. Asymmetric scans were performed in this investigation using the (115) reflection plane. Scans were taken at an ω^- of $\sim 31.5^\circ$ and an ω^+ of $\sim 63.2^\circ$ and a 2θ value of $\sim 95.0^\circ$. At both ω^- and ω^+ , scans were taken at a rotational angle of -90° and 90° . ω - 2θ scans were taken over a 1° range of ω , with a step size of 0.00025° and time per step of 0.5s for a total of 4001 steps.

Scans of the as grown SL/Si structure were taken in order to determine what were considered fully-strained values of the parallel and perpendicular lattice constants. These values gave a good idea of the dimensions of the original unit cell of the epilayer and would allow estimation of the comparative amount of relaxation that occurred through processing. Scans were limited to two anneal temperatures, 900 and 1000 $^\circ\text{C}$, and two anneal times 6 and 8 min and 1 and 3 min for 900 and 1000 $^\circ\text{C}$, respectively. Scans were taken of samples annealed at these temperatures and times in inert, oxidizing, and nitriding ambients. Table 5-3 presents the resulting $a_{e//}$ and $a_{e\perp}$ values after analysis using the equations given in Section 2.4.4. The estimated error in the values of $a_{e//}$ and $a_{e\perp}$ is ± 0.0002 nm and is derived from the error in ω angle measurement (0.00025°).

5.5.3 TEM

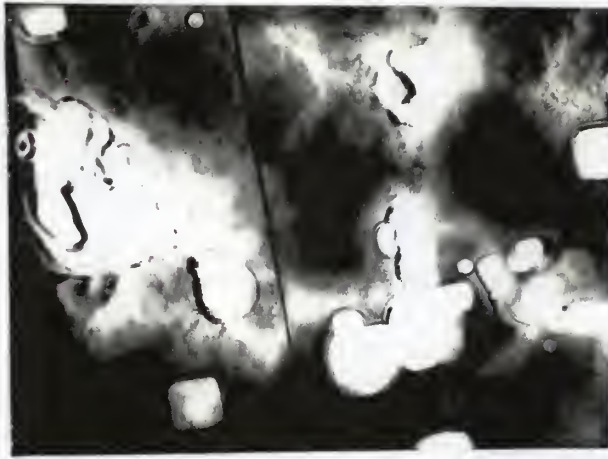
Because SL/Si is strained and has been shown to have dislocations after growth and before thermal processing, it is important to know at least qualitatively the dislocation density after annealing compared to that of the as

grown structure. This will give a qualitative idea of the possible contribution of relaxation through dislocation formation to the diffusivity values calculated in the preceding section. All plan-views were taken with the zone axis of (100) so that the sample is exactly perpendicular to the electron beam, using the (220) reflection.

Table 5-3. Parallel and perpendicular lattice constants of SL/Si.

T (°C)	time (min)	Inert		Oxidizing		Nitriding	
		$a_{e//}$	$a_{e\perp}$	$a_{e//}$	$a_{e\perp}$	$a_{e//}$	$a_{e\perp}$
As Grown	-	0.5431	0.5448	0.5431	0.5448	0.5431	0.5448
900	6	0.5432	0.5447	0.5431	0.5447	0.5431	0.5447
900	8	0.5431	0.5447	0.5431	0.5447	0.5431	0.5447
1000	1	0.5431	0.5447	0.5432	0.5447	0.5431	0.5447
1000	3	0.5432	0.5447	0.5432	0.5447	0.5431	0.5447

As discussed in Section 2.2.3, the as-grown SL/Si exhibited no misfit dislocations in the areas viewed by plan-view micrograph, however, threading dislocations were present in cross-section images of the as-deposited structure. One threading dislocation existed in the area of view, spanning from the substrate/buffer interface to the surface. This was most likely indicative of additional threading dislocations present throughout the further regions of the structure. As stated above, due to the nature of XTEM, it was impossible to determine precisely what this dislocation volume might have been. The source of both the misfit and threading dislocations is unclear at present but could most likely be due to the high growth temperature of 700 °C. The plan view image of SL/Si annealed in inert



20,000x  500nm

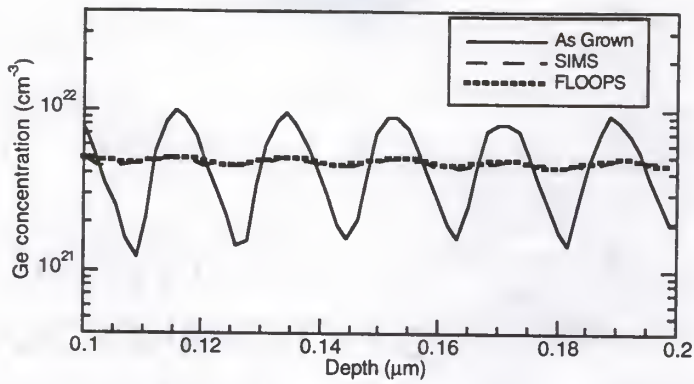
Figure 5-5. Plan view TEM micrographs of structure SL/Si after annealing in inert ambient at 850°C for 8 min.

ambient at 850°C for 8 min is shown in Figure 5-5. An isolated misfit is present which qualitatively suggests that the annealed sample contained approximately as many misfit dislocations as the as-deposited structure, and the density was still significantly small. This is in direct contrast to the results of structure SL/SiGe. Furthermore, no curved lines existed in micrographs of SL/Si, as were seen for SL/SiGe (Figure 4-5). This indicates that the threading dislocation density and lengths were minimal and far less than those in SL/SiGe. In the micrograph shown in Figure 5-5 there are sample preparation artifacts, light square areas, similar to those seen in SL/SiGe TEM micrographs, which can be attributed to the etching process. These artifacts did not, however, affect the ability to examine the dislocation density of the structure. Clearly, the initial strain state of SL/Si is markedly different than that of SL/SiGe and strain relaxation evolution through the generation of dislocations is different as well. It would appear that SLs with $\text{Si}_{1-x}\text{Ge}_x$ layers in compressive strain generate less dislocations through relaxation than SLs with Si layers in tensile strain.

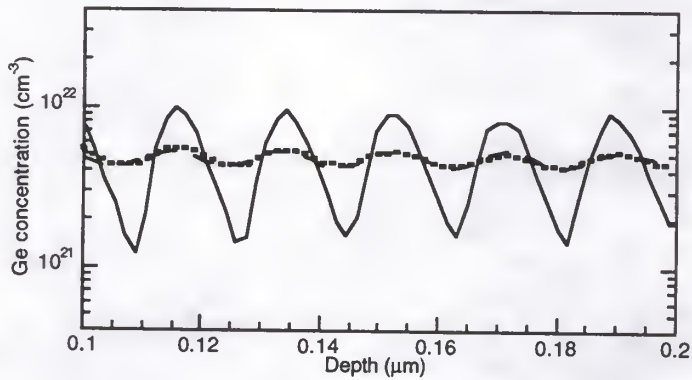
5.6 Discussion

5.6.1 Diffusivities Determined from SIMS and FLOOPS

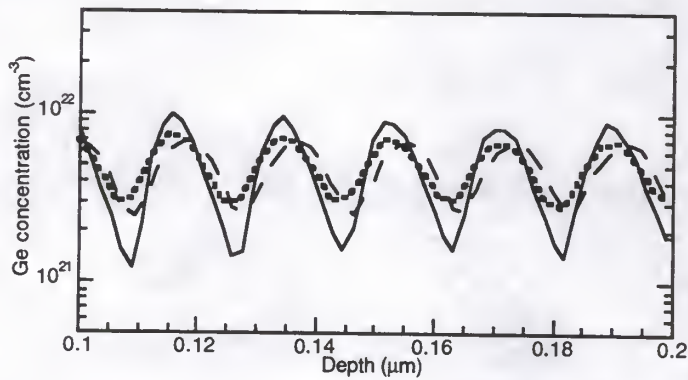
The diffusion profiles generated by the Fermi model provided very good fits to the experimentally determined SIMS profiles in the case of anneals performed in inert ambient, as demonstrated in Figure 5-6 for 950 °C and an anneal time of 3 min. This indicates that the assumptions made in



a.



b.



c.

Figure 5-6. Comparison of experimentally determined SIMS profile and FLOOPS profile for 950 °C and 3 min in (a) inert (b) oxidizing and (c) nitriding ambient.

the FLOOPS model (Section 3.3), while not necessarily accurate, are good enough to provide diffusivity values that are reasonable.

When analyzing the diffusion profiles for structure SQW/MBE and SQW/VPE in Chapter 3, there was a question of whether the profiles were flat, and if so, whether this indicated a concentration-dependent diffusivity (Section 3.5.1). The diffusion profiles determined for SL/Si are Gaussian and show no flatness in the wells whatsoever at any temperature. It can therefore be concluded that diffusion in structure SL/Si is concentration-independent. This corresponds with the concentration-independent diffusion found in structure SL/SiGe discussed in Chapter 4.

There have been more studies and analysis of diffusion behavior in inert ambient of $\text{Si}_{1-x}\text{Ge}_x/\text{Si}$ SL structures with a Si buffer than for those with a $\text{Si}_{1-y}\text{Ge}_y$ buffer. Holländer *et al.* [Hol92] studied interdiffusion of a $\text{Si}_{0.80}\text{Ge}_{0.20}/\text{Si}$ SL with five periods of 10 nm Si and 10 nm $\text{Si}_{0.80}\text{Ge}_{0.20}$ layers. It is also important to note that Holländer *et al.* investigated additional structures with Ge compositions as high as $x=0.70$, but for purposes of direct comparison to the results of this study, these structures will be ignored. The diffusivities of Holländer *et al.* plotted in Figure 5-7 were extracted using a Fourier algorithm to fit RBS spectra over anneal temperatures 1000 to 1125 °C. Prokes and Wang [Pro90] studied interdiffusion of a $\text{Si}_{0.65}\text{Ge}_{0.35}/\text{Si}$ SL with sixty periods of 12 nm Si and 4 nm $\text{Si}_{0.65}\text{Ge}_{0.35}$ layers. The diffusivities plotted in Figure 5-7 were extracted using the decay of intensity of the first order satellite peak from HRXRD scans, a method identical that described in Section

5.5.2.1, over anneal temperature 700 to 880 °C. Bean *et al.* [Bea85] studied interdiffusion of a $\text{Si}_{0.40}\text{Ge}_{0.60}/\text{Si}$ SL with three periods of 50 nm Si and 14 nm $\text{Si}_{0.40}\text{Ge}_{0.60}$ layers. The diffusivities reported by Bean *et al.*, plotted in Figure 5-7, were extracted using an algorithm that fit the second moment of the peak in the RBS spectra, over anneal temperatures 800 to 1050 °C. Boucaud *et al.* [Bou96] studied interdiffusion of a $\text{Si}_{0.70}\text{Ge}_{0.30}/\text{Si}$ SL with fifty periods of 17 nm Si and 2 nm $\text{Si}_{0.70}\text{Ge}_{0.30}$ layers. The diffusivities of Boucaud *et al.*, covering anneal temperatures 750 to 950 °C plotted in Figure 5-10, were extracted using the shifts of photoluminescence (PL) peaks.

Every study discussed above used $\text{Si}_{1-x}\text{Ge}_x$ compositions, layer structures, temperature ranges, and extraction methods which were different from each other and different than those used in this work. Every previous study used $\text{Si}_{1-x}\text{Ge}_x$ layers with greater, and in some cases, much greater, Ge composition than the $x=0.15$ for SL/Si. The temperature ranges of all studies included at least one temperature common to those used for this investigation. At all anneal temperatures used in this work, however, diffusivities are higher than, and not within error of, those previously reported (Figure 5-7). This may be due to differences in structure composition or analysis methods used in each study compared to this investigation. Interestingly, Prokes and Wang used the same HRXRD method to extract diffusivities as was used to extract diffusivities presented in Section 5.5.2.1. Comparison of these results (Section 5.6.2) will provide insight into the effect of extraction method on diffusion coefficient values.

The diffusivity values of this work show non-Arrhenius behavior (Figure 5-7). The values at 850 and 900 °C are practically the same, as are the values at 950 and 1000 °C. The diffusivity extracted for 950 °C is the most anomalous, with a value *above* that for 1000 °C for this work and also much greater than the general curve of previously reported values. Most of the reported studies have larger temperature spans and provide diffusivities that cover more orders of magnitude than those of this work. These factors indicate that the extracted diffusivities of this work are more unreliable than those reported in previous investigations. A possible reason for the unreliability of the data of this work may be temperature measurement problems with the RTA, especially within the smaller 50 degree increments.

The activation energy of Ge diffusion in $\text{Si}_{1-x}\text{Ge}_x/\text{Si}$ SLs with a Si buffer layer in inert ambient determined in this study, approximately $3.63 \text{ eV} \pm 0.24$, is within the range of those previously reported. As stated above, the Ge concentrations of the $\text{Si}_{1-x}\text{Ge}_x$ layers in previous studies were all significantly higher than the Ge content of SL/Si. All SL structures and experimental parameters of the respective studies have been described above. Holländer *et al.* and Prokes and Wang reported intermediate activation energies of 4.0 eV and 4.4 eV respectively. Boucaud *et al.* reported a low activation energy of 2.42 eV while Bean *et al.* reported the highest activation energy, 5.0 eV. This wide range of activation energies may be due factors such as differences in layer thicknesses, Ge content and analysis method used. Once again, the activation energy reported by Prokes and Wang using HRXRD will be

compared to that obtained in this investigation through HRXRD (Section 5.6.2) to determine whether, in this instance, analysis method affects calculated values.

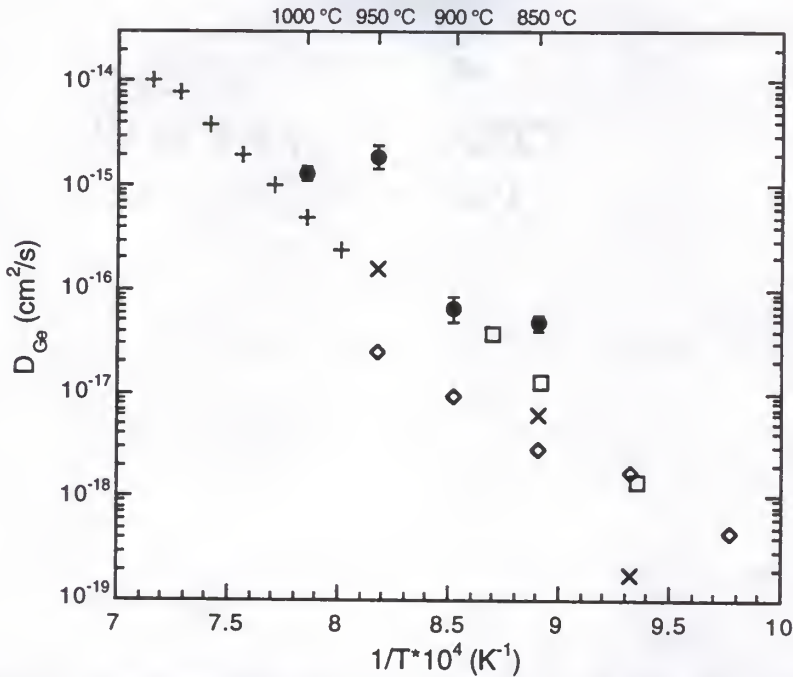
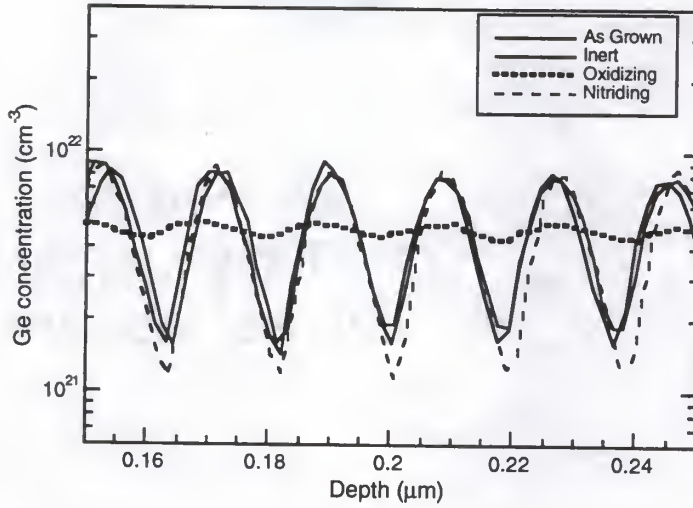
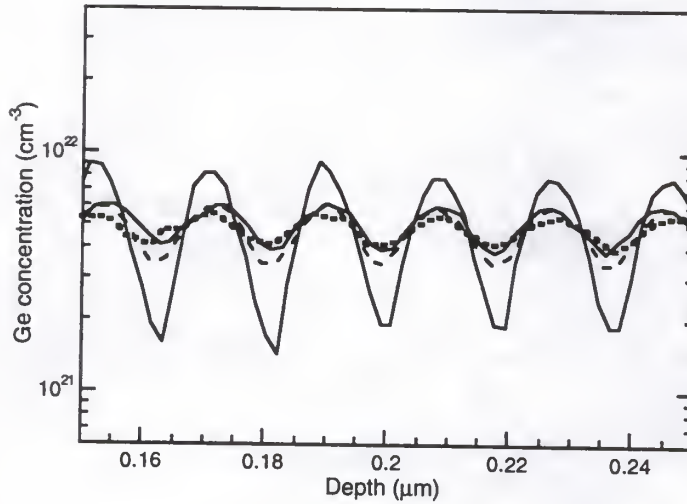


Figure 5-7. Diffusivities of Ge in $Si_{1-x}Ge_x/Si$ SLs with a Si(100) buffer layer from previous studies and this work.

Comparison of diffusion in inert, oxidizing, and nitriding ambients yields questionable conclusions due to the apparent non-Arrhenius behavior of the actual diffusivity values in each ambient. At the lower temperatures studied, Ge profiles in oxidizing ambient show greater diffusion than profiles in inert ambient (Figure 5-8a). Diffusivities extracted at 850 and 900 °C in oxidizing ambient are greater than those in inert ambient and are not within error of each other. This indicates that at these lower temperatures a supersaturation of interstitials results in enhancement of Ge diffusion;



a.



b.

Figure 5-8. Comparison of Ge SIMS profiles in inert, oxidizing and nitriding ambients for SL/Si. Sample annealed at (a) 900 °C for 6 min and (b) 1000 °C for 2 min.

interstitial point defects play a measurable role in the diffusion process in this temperature range. Diffusivities extracted for both ambients at highertemperatures 950 and 1000 °C are similar and within error of each other, as illustrated in Figure 5-2. Ge depth versus concentration profiles at these temperatures are virtually identical (Figure 5-8b). At these higher temperatures, diffusion is unaffected by interstitial supersaturation. This leads to the conclusion that interstitials play a decreasing role in diffusion with increasing temperature. Once again, because of the non-Arrhenius behavior of the diffusivity values, these conclusions must be confirmed with continued studies.

The activation energy of $2.81 \text{ eV} \pm 0.21$ calculated for interdiffusion in oxidizing ambient is the first reported for Si/Si_{1-x}Ge_x SL with a Si buffer layer. This activation energy is notably less than that for diffusion in inert ambient and may indicate that the interstitial component of Si/Si_{1-x}Ge_x SL interdiffusion is significant. This result is similar to that found for SL/SiGe.

The activation energy of $4.16 \text{ eV} \pm 0.22$ calculated for the interdiffusion in nitriding ambient is the first activation energy of interdiffusion under vacancy injection reported for a Si/Si_{1-x}Ge_x SL with a Si buffer layer. This activation energy is 0.5 and 1.5 eV higher than that for diffusion in inert ambient and oxidizing ambient, respectively, and very similar to the results found for SL/SiGe. Like the behavior found for SL/SiGe, from the activation energies alone, one would expect that oxidation (interstitial injection) of SL/Si would enhance diffusion, while nitridation (vacancy injection) would

retard diffusion. Very slight retardation was seen in profiles of samples annealed in nitriding ambient (Figure 5-8), however, little enhancement, and in some cases retardation, was observed for samples annealed in oxidizing ambient.

5.6.2 Diffusivities Determined from HRXRD

Section 5.5.2.1 described briefly the method used to determine diffusivities of periodic SLs from ω -2 θ scans using HRXRD and listed results for SL/Si. As discussed in Section 4.6.2 for SL/SiGe, the relative intensities of the first order satellite peaks showed the expected trends and diffusion coefficients were extracted. The ω -2 θ scans resulted in standardized first order satellite peaks that did not always decrease progressively in intensity with time (Figure 5-4). As in Chapter 4, this can most likely be attributed to instrumental error in the measurement of intensity.

Figure 5-4 is a plot of the natural logarithm of the standardized intensity of the first order satellite peak versus time. The slope of the decay of the intensity is expected to be negative and is the value to be used in Equation 4-5 to extract diffusion coefficients for each temperature. The slopes of the fitted curves for the decrease in intensity of the first order satellite peak for increasing anneal times at 1000 °C in inert, oxidizing and nitriding ambients are negative, making the calculated D values negative, even though for all ambients actual $\ln(I/I_0)$ values do not decay consistently with increasing anneal time. The values of $\ln(I/I_0)$ of the first order satellite peak for increasing anneal times at 900 °C are even more erratic. A linear fit to the

data points yields a negative slope for both inert and nitriding ambients, yet the slope of the decay in oxidizing ambient is positive, such that a diffusion coefficient cannot be extracted using Equation 4-5. Diffusivity values can be calculated from all curves except that for 1000 °C in oxidizing ambient, but based purely on the intensity data, no extracted diffusivity can be considered reliable. As stated in Chapter 4, HRXRD characterization in conjunction with Equation 4-5 shows potential for providing dependable diffusion coefficient data, however much more work needs to be done to refine the instrumental method needed to obtain scans that are reliable.

It is still of interest to compare these values with those determined from SIMS and FLOOPS presented in Section 5.5.1 (Table 5-4). The diffusivities in inert and nitriding ambients at an anneal temperature of 900 °C are not within error of each other. At an anneal temperature of 1000 °C only the diffusivities in nitriding ambient are within error of each other. In inert and oxidizing ambients the diffusion coefficients of the two methods disagree by orders of magnitude. Due to the reasons explained above, the diffusivities extracted using SIMS/FLOOPS are considered to be much more reliable. It is pointless to fit these diffusivities to an Arrhenius expression, as there are only two temperatures investigated.

As a final analysis of the diffusivities extracted using HRXRD, it is interesting to compare them with the values reported by Prokes and Wang [Pro90] using the same method. Prokes and Wang studied diffusion in inert ambient over a lower temperature range than that of this study, 700 to 880 °C.

If their Arrhenius expression derived for the diffusivity over this temperature range is slightly extended to 900 °C, a diffusion coefficient of approximately 9.4×10^{-17} cm²/s can be extracted, which is *three orders of magnitude* lower than that of this study, but almost the same as that determined from SIMS/FLOOPS. This is additional verification that the values determined through SIMS/FLOOPS are more reliable than those through HRXRD and that, while HRXRD shows potential for providing dependable diffusion coefficient data, much more work needs to be done to refine the instrumental method needed to obtain scans that are reliable.

5.6.3 Strain Relaxation from HRXRD

Table 5-4. Diffusivities of SL/Si extracted from FLOOPS and HRXRD.

T (°C)	D _{Ge} ^{Inert} (cm ² /s)		D _{Ge} ^{Ox} (cm ² /s)		D _{Ge} ^{Nit} (cm ² /s)	
	FLOOPS	HRXRD	FLOOPS	HRXRD	FLOOPS	HRXRD
900	4.58×10^{-17}	2.13×10^{-16}	4.58×10^{-17}	-	1.70×10^{-17}	5.24×10^{-17}
1000	1.18×10^{-15}	5.17×10^{-16}	1.70×10^{-15}	6.14×10^{-17}	1.07×10^{-15}	1.29×10^{-15}

Section 5.5.2.2 briefly described the HRXRD method used to determine the perpendicular and parallel lattice constants of the epilayer which are used estimate the strain relaxation which occurs in periodic SLs with thermal processing. All results using this method are listed for SL/Si in Table 5-3.

The change in the angular separation of the zero order epilayer peak and the Si(004) substrate peak with time did not show the expected trend. Because the epilayer is in compressive strain when grown on the Si buffer, it

is expected that progressive relaxation would cause the parallel lattice constant to increase towards its natural value, while the perpendicular lattice constant would decrease towards its unstrained value. The values of $a_{e//}$ in Table 5-3 were expected to increase with increasing anneal time, while the values of $a_{e\perp}$ were expected to decrease. After calculations were performed using Equations 2-7 and 2-8, the values of both $a_{e//}$ and $a_{e\perp}$ were found to remain constant with time in all ambients, with values almost identical to those of the as deposited cubic unit cell.

Disregarding the possible errors in lattice constant measurement, which are estimated at only ± 0.0002 nm, and assuming the evident trends are correct, it is logical to conclude that the strain state of the structure must be redefined to fit the experimental results. The reason for uniform $a_{e//}$ and $a_{e\perp}$ could be due to shear deformation in the epitaxial layer [Bar78] or distortion in all three lattice directions. In a normal cubic unit cell, the lengths of the sides of the cell, a , b , and c , are all equal. In tetragonal strain discussed previously, $a=b \neq c$, in which a and b have been denoted as $a_{e//}$ during this work, and c has been denoted as $a_{e\perp}$. In orthogonal strain, $a \neq b \neq c$. The b direction cannot be measured using the normal HRXRD method described, so if a and b are not equal, then there might be relaxation in the b direction that is immeasurable. Further studies are needed to determine the reason for this behavior. There are two other possible reasons for the constant lattice parameter values: (1) the as-deposited structure is fully relaxed, from

dislocations generated during the growth process or (2) the annealed structures do not relax significantly. The first reason is highly improbable due to PTEM results discussed in Section 5.5.3, in which a low density of misfit dislocations were seen in micrographs of the as-deposited structure. While the as grown structure is definitely slightly relaxed, due to threading dislocations visible in XTEM micrographs, the lack of misfit dislocations in the PTEM micrograph indicate that it is far from fully relaxed. The second reason is more probable because qualitatively the same misfit dislocations are visible in micrographs of annealed samples as the as grown sample. Further studies must be done to determine the reasons for the uniform lattice constants seen in Table 5-3.

5.6.4 Effect of Strain State on Diffusivity Values

As has been stated throughout this dissertation, diffusion of Ge in $\text{Si}_{1-x}\text{Ge}_x/\text{Si}$ materials is affected by both strain and compositional changes. Chapter 4 presented results and discussion of the strain relaxation of SL/SiGe after thermal treatment through TEM and HRXRD characterization. Results of compositional changes were also presented for SL/SiGe through characterization by SIMS and analysis using FLOOPS. Chapter 5 presented results of these same influences on structure SL/Si. The utility of both sets of information is the ability to directly compare the respective parameters of SL/Si and SL/SiGe, whose only difference is the strain state of the Si and $\text{Si}_{1-x}\text{Ge}_x$ layers in the periodic material. This section attempts to provide an organized, tabular comparison of the diffusion coefficients, fractional vacancy,

components of diffusion and activation energies of diffusion of SL/SiGe and SL/Si extracted from SIMS/FLOOPS analysis. Comparison of HRXRD and TEM results has already been modestly addressed in Sections 5.6.2, 5.6.3 and 5.5.3. HRXRD results, while interesting, were proven unreliable, and therefore extensive comparison of the resulting values would be useless.

The diffusivities of SL/SiGe and SL/Si are compared in tabular form in Table 5-5. In inert ambient values for 850, 950 and 1000 °C are not within error of each other, yet the separation is not large. The diffusion coefficients for 900 °C are the only values that are within error of each other. The values for 850, 950 and 1000 °C, while not within standard error, are within two standard deviations of each other, which is not large. In oxidizing and nitriding ambients, values at all temperatures are within error of each other. Based on these results, it can be concluded that strain state of the Si and Si_{1-x}Ge_x layers does not affect the overall diffusivity.

The activation energies of diffusion of SL/SiGe and SL/Si in inert, oxidizing, and nitriding ambients are compared in Table 5-6. The activation energies of SL/Si in inert and oxidizing ambient are higher than and not within error of, those for SL/SiGe. This may indicate a possible effect of strain state of the layers, however, it is unlikely. The activation energies in nitriding ambient are within error of each other.

From the information presented above, it seems most likely that diffusion is not significantly affected by the difference in tensile and compressive strain in the periodic multilayers of the SLs studied.

Table 5-5. Comparison of diffusivities of SL/SiGe and SL/Si in inert, oxidizing and nitriding ambients.

T (°C)	time (min)	Inert		Oxidizing		Nitriding	
		D:SL/SiGe (cm ² /s)	D:SL/Si (cm ² /s)	D:SL/SiGe (cm ² /s)	D:SL/Si (cm ² /s)	D:SL/SiGe (cm ² /s)	D:SL/Si (cm ² /s)
850	8	6.70×10 ⁻¹⁷	4.00×10 ⁻¹⁷	2.32×10 ⁻¹⁶	4.00×10 ⁻¹⁷	8.49×10 ⁻¹⁸	1.42×10 ⁻¹⁷
900	4	6.80×10 ⁻¹⁷	4.58×10 ⁻¹⁷	4.58×10 ⁻¹⁷	4.58×10 ⁻¹⁷	1.70×10 ⁻¹⁷	1.70×10 ⁻¹⁷
950	3	1.73×10 ⁻¹⁵	3.26×10 ⁻¹⁵	1.31×10 ⁻¹⁵	1.31×10 ⁻¹⁵	2.86×10 ⁻¹⁶	3.46×10 ⁻¹⁶
1000	2	1.77×10 ⁻¹⁵	1.18×10 ⁻¹⁵	2.23×10 ⁻¹⁵	1.77×10 ⁻¹⁵	8.96×10 ⁻¹⁶	1.07×10 ⁻¹⁵

Table 5-6. Comparison of activation energies of SL/SiGe and SL/Si in inert, oxidizing and nitriding ambients.

T (°C)	E_a :SL/SiGe (eV)	E_a :SL/Si (eV)
Inert	3.14 ± 0.20	3.63 ± 0.24
Oxidizing	1.71 ± 0.19	2.81 ± 0.21
Nitriding	4.07 ± 0.29	4.16 ± 0.22

5.7 Conclusions

The experimental results discussed above have provided considerable contributions to the knowledge of Ge diffusion behavior in $\text{Si}_{1-x}\text{Ge}_x/\text{Si}$ asymmetrically strained SLs with a Si buffer, as well as the effect of strain on interdiffusion in such a material. The diffusion model used in FLOOPS simulations, while employing several simplifying assumptions, proved to be a satisfactory first effort at predicting Ge diffusion behavior. The diffusion coefficient exhibited Gaussian, concentration-independent behavior.

Diffusivities extracted in inert ambient were consistently higher than previously reported values [Pro90, Bou96, Hol92, Bea85] and showed non-Arrhenius behavior. Irregularities in the RTA temperature control may be a reason for this behavior. An activation energy of diffusion of $3.63 \text{ eV} \pm 0.24$ was extracted, which was within the range of previously reported values.

For the first time, diffusivities extracted under interstitial injection conditions were reported, with a resulting activation energy for diffusion of $2.81 \text{ eV} \pm 0.21$. Slight enhancement of Ge diffusion was seen in oxidizing ambient when compared to inert ambient at the lower temperatures, 850 and

900 °C. At the higher temperatures, 950 and 1000 °C, no enhancement was seen. This leads to the conclusion that interstitials play a decreasing role in diffusion with increasing temperature, due to either an actual decrease in interstitial contribution to the diffusion mechanism or to the increase in the recombination rate of interstitials and vacancies.

For the first time, diffusivities extracted under vacancy injection conditions were reported, with a resulting activation energy for diffusion of $4.16 \text{ eV} \pm 0.22$. Significant retardation of Ge diffusion was seen in nitriding ambient when compared to inert ambient at all temperatures, indicating that diffusion is dominated by interstitials. This contradicted the results of the oxidation experiments.

Plan-view TEM micrographs showed qualitatively that dislocation density remained constant after anneal relative to the as-deposited value. This suggests that a minimal amount of misfit dislocations, and therefore relaxation, is created with thermal processing. This conclusion was supported by HRXRD analysis of SL/Si strain relaxation. The lattice constants of the SL/Si pseudo-epilayer were seen to remain constant upon anneal when compared to the as-deposited values. Attempts to extract a diffusion coefficient from the intensities of the first order satellite peaks from ω -2 θ HRXRD scans provided values that were unreliable. While characterization through HRXRD seems promising, future work must be done to perfect the experimental technique and diffusion coefficient extraction method.

Comparisons of SL/SiGe results from Chapter 4 with SL/Si results presented in this chapter reveal that, whether the Si and $\text{Si}_{1-x}\text{Ge}_x$ layers are in tensile, compressive or strain-free states, diffusivities and activation energies are similar. This could imply very sweeping statements regarding the lack of contribution of the strain component to diffusion, however, throughout Chapter 3, 4 and 5, there has been evidence that strain does have some sort of impact on interdiffusion. Intense future work must be done to clarify the role of strain energy in $\text{Si}_{1-x}\text{Ge}_x/\text{Si}$ diffusion.

CHAPTER 6

CONCLUSIONS AND FUTURE WORK

This dissertation has focused on diffusion behavior of $\text{Si}_{1-x}\text{Ge}_x/\text{Si}$ as a function of layer structure, processing temperature and processing time. In particular, the roles of vacancy and interstitial point defects in the diffusion process have been investigated. Section 6.1 will summarize the conclusions reached from this research, Section 6.2 will state the original contributions of this work to the fast-growing interest in diffusion in $\text{Si}_{1-x}\text{Ge}_x$, and Section 6.3 will offer suggestions for areas of continued research.

6.1 Conclusions

6.1.1 Single Quantum Well Structures

In Chapter 3, the diffusion behavior of single quantum wells of $\text{Si}_{1-x}\text{Ge}_x/\text{Si}$ over anneal temperatures 900 to 1200 °C was investigated and results were presented. The extraction of diffusion coefficients using SIMS and FLOOPS yielded activation energies of ~5.8 eV, 5.0 eV, and 3.0 eV for diffusion in inert, oxidizing, and nitriding ambients, respectively. No difference in diffusion behavior was seen between SQW structures grown by molecular beam epitaxy and vapor phase epitaxy.

The diffusivities extracted for diffusion in inert ambient agreed well with values previously reported in literature. The calculated activation

energy of diffusion in inert ambient, 5.8 eV, was higher than values previously reported in literature. This was attributed to the much larger temperature span used in this work. This factor, as well as resulting diffusivities that cover over five orders of magnitude compared to just two orders of magnitude of other studies, led to the conclusion that the value of E_a calculated in this dissertation was more reliable than those of previous investigations. The extracted diffusion coefficients, at constant temperature, were found to be time-independent in all three ambients.

Neither enhancement nor retardation was observed for diffusion at the lower temperatures of 900 and 1000 °C in oxidizing ambient compared to inert ambient. At the higher temperatures of 1100 and 1200 °C, however, diffusion retardation under oxidizing ambient (interstitial supersaturation) compared to inert ambient was seen. This led to the conclusion that interstitial participation is negligible and vacancy point defects dominate the diffusion process. This conclusion was further supported by the estimated value of $f_i=0.10$ at the low temperatures and $f_i=0.02$ at the higher temperatures from oxidation and B marker layer experiments. The large value of the vacancy component of diffusion agreed well with that reported by Cowern *et al.* [Cow96] for 875 °C.

Significant retardation of diffusion occurred at all temperatures in nitriding ambient compared to inert ambient. This contradicted the results from oxidation experiments. Fractional interstitial and vacancy components

could not be estimated due to inert diffusivities that overestimated diffusion in the FLOOPS Pair model.

Experiments conducted using buried boron marker layers verified that excess interstitials injected as a result of surface oxidation during anneals in oxidizing ambient did indeed travel to and through the $\text{Si}_{1-x}\text{Ge}_x$ layer and were available to participate in the diffusion process. These experiments also indicated that a portion of the injected interstitials were captured by dislocations. Experiments conducted using this same marker layer structure verified that vacancies were injected as a result of surface nitridation and were also partially trapped by the dislocations.

6.1.2 Superlattice Structures

In Chapters 4 and 5, the diffusion behavior of $\text{Si}_{1-x}\text{Ge}_x/\text{Si}$ superlattices over anneal temperatures 850 to 1000 °C was investigated and results were presented. Two structures were studied, a SL with a $\text{Si}_{1-x}\text{Ge}_x$ buffer layer and a SL with a Si buffer. It was determined from investigations of both structures that rapid thermal annealing for the time and temperature profiles needed to obtain the proper diffusion lengths was pushing the limits of the processor. Accurate temperature control at these processing regimes was questionable. The concentration versus depth profiles of the wells exhibited strictly Gaussian decay, which indicated that the extracted diffusion coefficients were concentration-independent. Calculated diffusivities for both structures were higher at all temperatures than those previously reported in literature. These diffusivities also exhibited non-Arrhenius behavior that was attributed to

temperature control issues. For both structures, minimal diffusion enhancement occurred in oxidizing ambient compared to inert ambient at all temperatures. For both structures, diffusion retardation occurred in nitriding ambient compared to inert ambient at all temperatures. High resolution x-ray diffraction was used as an alternate method to extract diffusion coefficients. The resulting values were found to be unreliable and the experimental and analysis method must be refined. Finally, the diffusivities, activation energies and fractional vacancy components of the two structures were found to be within error of each other.

The extraction of diffusion coefficients using SIMS and FLOOPS yielded activation energies for the SL with a $\text{Si}_{1-x}\text{Ge}_x$ buffer of 3.14, 2.43 and 4.07 eV for diffusion in inert, oxidizing and nitriding ambients, respectively. HRXRD analysis of the cubic unit cell revealed that, when the $\text{Si}_{1-x}\text{Ge}_x$ buffer layer was viewed as part of the pseudo-epilayer, the perpendicular lattice constant, $a_{e\perp}$, was constant with increased annealing time, while the parallel lattice constant, $a_{e\parallel}$, increased slightly.

The extraction of diffusion coefficients using SIMS and FLOOPS yielded activation energies for the SL with a Si buffer of 3.63, 2.81 and 4.16 eV for diffusion in inert, oxidizing, and nitriding ambients, respectively. HRXRD analysis of the cubic unit cell of the $\text{Si}_{1-x}\text{Ge}_x/\text{Si}$ pseudo-epilayer revealed that both the perpendicular lattice constant, $a_{e\perp}$, and the parallel lattice constant, $a_{e\parallel}$, remained constant with increasing anneal time.

6.1.3 Strain Effects

Diffusion coefficients of initially fully strained samples were equivalent to those simulated for initially partially relaxed samples after anneal in both inert and oxidizing ambients. Strain relaxation and increased dislocation densities seemed to have an insignificant effect on Ge diffusion in Si/Si_{1-x}Ge_x/Si SQWs. Diffusivities calculated for SLs with a Si_{1-x}Ge_x buffer and for SLs with a Si buffer were equivalent. Both of these results led to the conclusion that strain has a very minimal effect on diffusion.

Cross sectional and plan view TEM micrographs showed that in the SQWs and the SL with the Si_{1-x}Ge_x buffer, dislocation densities increased noticeably after anneal compared to as-deposited values. The SL with the Si_{1-x}Ge_x buffer showed dislocation formation and propagation into the Si substrate and cap layers only, with the Si_{1-x}Ge_x/Si multilayers relatively dislocation-free. The SL with the Si buffer showed a very small increase in dislocation density after anneal compared to its as-grown value.

6.2 Contributions

6.2.1 Modeling

- A successful, simple model was developed within the Florida Object Oriented Process Simulation software which effectively simulated the diffusion behavior of both SQW and SL material in inert, oxidizing, and nitriding ambients.

6.2.2 Experimental

- Diffusion coefficients and an activation energy for diffusion of $\text{Si}_{1-x}\text{Ge}_x/\text{Si}$ SQWs were extracted for the temperature range 1000 to 1200 °C in inert ambient.

- Diffusion coefficients spanning a larger temperature range than any previous study and with values covering five orders of magnitude were extracted for $\text{Si}_{1-x}\text{Ge}_x/\text{Si}$ SQWs.

- Diffusion coefficients and an activation energy for diffusion of $\text{Si}_{1-x}\text{Ge}_x/\text{Si}$ SQWs were extracted for temperatures 900 to 1200 °C in oxidizing ambient.

- Diffusion coefficients and an activation energy for diffusion of $\text{Si}_{1-x}\text{Ge}_x/\text{Si}$ SQWs were extracted for temperatures 1100 and 1200 °C in nitriding ambient.

- It was determined that the diffusion coefficients at constant temperature for SQWs were independent of time in inert, oxidizing and nitriding ambients.

- A fractional interstitial component of diffusion, f_i , for SQWs was estimated for a temperature range 900 to 1200 °C from oxidizing experiments.

- Diffusivities of initially partially relaxed SQWs were extracted over a temperature range 900 to 1200 °C, for a wide variety of times in inert, oxidizing, and nitriding ambients.

- Diffusion coefficients and an activation energy for diffusion of an $\text{Si}_{1-x}\text{Ge}_x/\text{Si}$ SL with a $\text{Si}_{1-x}\text{Ge}_x$ buffer layer were extracted for the temperature range 850 to 1000 °C in inert, oxidizing, and nitriding ambients.

- Diffusion coefficients and an activation energy for diffusion of an $\text{Si}_{1-x}\text{Ge}_x/\text{Si}$ SL with a Si buffer layer were extracted for the temperature range 850 to 1000 °C in inert, oxidizing and nitriding ambients.

- Unit cell lattice parameter values for annealed SLs with both $\text{Si}_{1-x}\text{Ge}_x$ and Si buffer layers were calculated using HRXRD (inert, oxidizing, and nitriding ambients).

6.3 Future Work

6.3.1 Single Quantum Well Investigations

It is recommended that attempts be made to replicate some of the less conclusive experiments presented for SQW diffusion. Particularly, it should be conclusively determined whether the fractional vacancy component is constant with temperature, as interpreted in Chapter 3, and in relation, whether the retarded diffusion observed in oxidizing ambient at high temperatures can be attributed to an increasing fractional interstitial component or to a higher recombination rate. It is also recommended that experiments be performed to confirm whether diffusivities of fully strained SQWs are different from those of partially relaxed for an anneal temperature of 1200 °C, as reported in Chapter 3. Further studies should also be performed

to study more closely the relationship between relaxation and interstitial absorption.

The most important work that should be accomplished is to repeat all diffusion experiments described in this dissertation using pseudomorphic structures. This is the most definitive method of determining the impact of dislocations and relaxation on $\text{Si}_{1-x}\text{Ge}_x/\text{Si}$ diffusion parameters and obtaining f_v and f_i values from both oxidation and nitridation experiments that more closely reflect the true values. Experimental anneal of partially relaxed structures should also be done to address this issue, as well as to confirm the simulated results of Section 3.4.2.

6.3.2 Superlattice Investigations

The non-Arrhenius behavior of both SL structures should be further investigated. Two possible reasons for this behavior must be addressed: (1) the reliability and effectiveness of rapid thermal processing at thermal budgets needed for the correct diffusion lengths and (2) possible time dependency of diffusion in SLs at constant temperature. If a time-dependent diffusivity for SLs is confirmed, then it would be interesting to investigate the reason they differ from the time-independent diffusivity of the SQWs.

The experimental and analytic method of determining diffusivities and lattice constants from HRXRD data must be refined. More experiments should be performed to conclude if strain state of the layers indeed has no effect on diffusivity values. Better structure correspondence between SLs is needed, and work with a symmetrically strained SL would be interesting.

6.3.3 Simulations and Modeling

The model employed in $\text{Si}_{1-x}\text{Ge}_x/\text{Si}$ FLOOPS diffusion simulations in this dissertation should be revised to include some means of accounting for the high concentrations of Ge in the alloy, instead of approximating the concentration by dopant levels. C_I^* and C_V^* values for $\text{Si}_{1-x}\text{Ge}_x$ are thought to be different than those for Si. The increasing availability of data for dopant diffusion in $\text{Si}_{1-x}\text{Ge}_x$ might allow f_I and f_V values to be extracted based on $\text{Si}_{1-x}\text{Ge}_x$ values instead of Si values.

APPENDIX A EXAMPLES OF FLOOPS PROGRAMS

Fermi Model: Inert Ambient

```
dopant add name=Germanium
pdbSetDouble Si Ge I D0 { [Arrhenius 1.37e5 5.08]}
pdbSetDouble Si Ge I Dp 0
pdbSetDouble Si Ge V D0 0
pdbSetDouble Si Ge V Dp 0
pdbSetSwitch Si Ge DiffModel Fermi
```

```
line x loc = 0.0 tag = surf spac=0.003
line x loc = 0.05 tag = cap spac=0.003
line x loc = 0.10 tag = sige spac=0.005
line x loc = 0.20 tag = buffer spac=0.003
line x loc = 0.25 tag = back spac=1
```

```
region silicon xlo = surf xhi = back
```

```
init
```

```
profile name=Germanium infile=1819AsGrown2.98
```

```
sel z=log10(Germanium)
plot.1d label=Initial
```

```
diffuse time=1532 temp=900
sel z=log10(Germanium)
plot.1d label=Final !cle
```

```
profile name=target infile=1819.900.1532.f
```

```
sel z=log10(target)
```

```
plot.1d label=Experimental !cle
```


FERMI MODEL: OXIDIZING AMBIENT

```
dopant add name=Germanium
pdbSetDouble Si Ge I D0 { [Arrhenius 1.37e5 5.2] }
pdbSetDouble Si Ge I Dp 0
pdbSetDouble Si Ge V D0 0
pdbSetDouble Si Ge V Dp 0
pdbSetSwitch Si Ge DiffModel Fermi
```

```
line x loc = 0.0 tag = surf spac=0.003
line x loc = 0.05 tag = cap spac=0.003
line x loc = 0.10 tag = sige spac=0.005
line x loc = 0.20 tag = buffer spac=0.003
line x loc = 0.25 tag = back spac=1
```

```
region silicon xlo = surf xhi = back
```

```
init
```

```
profile name=Germanium infile=1819AsGrown2.98
```

```
sel z=log10(Germanium)
plot.1d label=Initial
```

```
diffuse time=1532 temp=900 dry
sel z=log10(Germanium)
plot.1d label=Final !cle
```

```
profile name=target infile=1819.900.1532f.Ox
```

```
sel z=log10(target)
plot.1d label=Experimental !cle
```

PAIR MODEL-OXIDIZING AMBIENT

```
dopant add name=Germanium
pdbSetDouble Si Ge I D0 $Ivalue
pdbSetDouble Si Ge I Dp 0
pdbSetDouble Si Ge V D0 $Vvalue
pdbSetDouble Si Ge V Dp 0
pdbSetSwitch Si Ge DiffModel Pair
```

```
line x loc = 0.0 tag = surf spac=0.003
line x loc = 0.05 tag = cap spac=0.003
line x loc = 0.10 tag = sige spac=0.005
line x loc = 0.20 tag = buffer spac=0.003
line x loc = 0.25 tag = back spac=1
```

```
region silicon xlo = surf xhi = back
```

```
init quiet
```

```
profile name=Germanium infile=1819AsGrown2.98
SetTemp 900
InitDefect 900
InitDopantPairs 900
```

```
sel z=log10(Germanium)
plot.1d label=Initial
```

```
diffuse time=1532 temp=900 init=1e-12 !adapt dry
sel z=log10(Germanium)
plot.1d label=Final !cle
```

```
profile name=target infile=1819.900.1532f.Ox
```

```
sel z=log10(target)
plot.1d label=Experimental !cle
```

PAIR MODEL-NITRIDING AMBIENT

```

pdbSetDouble Nitride_Silicon V injection 3.25e14
pdbSetBoolean Nitride_Silicon V time.inj 1
pdbSetBoolean Nitride_Silicon V recomb 1
pdbSetDouble Nitride_Silicon V Ksurf 100
pdbSetDouble Nitride_Silicon V Ksurf2 0.0

```

```

dopant add name=Germanium
pdbSetDouble Si Germanium I D0 $Ivalue
pdbSetDouble Si Germanium I Dp 0
pdbSetDouble Si Germanium V D0 $Vvalue
pdbSetDouble Si Germanium V Dp 0
pdbSetSwitch Si Germanium DiffModel Pair
pdbSetSwitch Si I DiffModel Numeric
pdbSetSwitch Si V DiffModel Numeric

```

```

line x loc = -0.1 tag = nit
line x loc = 0.0 tag = surf spac=0.003
line x loc = 0.05 tag = cap spac=0.003
line x loc = 0.10 tag = sige spac=0.005
line x loc = 0.20 tag = buffer spac=0.003
line x loc = 0.25 tag = back spac=1

```

```

region silicon xlo = surf xhi = back
region nitride xlo = nit xhi = surf

```

```

init quiet

```

```

profile name=Germanium infile=1AsGrown
SetTemp 950
InitDefect 950
InitDopantPairs 950

```

```

sel z=log10(Germanium)
plot.1d label=Initial

```

```

diffuse time=3 temp=950 init=1e-12 !adapt
sel z=log10(Germanium)

```

plot.1d label=Final !cle

profile name=target infile=1.950.180A

sel z=log10(target)

plot.1d label=Experimental !cle

APPENDIX B

GLOSSARY

acceptor- a negatively charged dopant that accepts an electron from the semiconductor lattice when introduced.

ambient- atmospheric environment in which thermal processing occurs.

band gap- the difference in energy between the valence and conduction band edges in a semiconductor.

base- part of a junction transistor.

base transit time- the time it takes a carrier to diffuse across the base from the emitter to the collector.

BJT- Bipolar Junction Transistor; a semiconductor transistor with two p-n junctions in series made out of one semiconductor material.

buffer- a semiconductor layer situated between the substrate and the thin epitaxial layers, intended to act as a barrier to diffusion and dislocation formation.

cap- a final semiconductor layer grown on top of epitaxial layers intended to prevent out-diffusion and other behaviors in a heterostructure.

carrier- mobile negatively or positively charged species in a semiconductor.

coherent- pseudomorphic, epitaxial layer thickness less than critical thickness.

conduction band- a band of allowed energy levels corresponding to unbonded electrons free to travel throughout the crystal.

critical thickness- the thickness at which dislocations begin to form in an epilayer lattice mismatched to its substrate.

current gain- a parameter used to judge HBT performance; the ratio of the collector current to the base current.

cutoff frequencies- the frequency at which the magnitude of the current gain is equal to 1.

dislocation- a deviation in the periodicity of a lattice arising from a line of points.

donor- a positively charged dopant that donates an electron to the semiconductor lattice when introduced.

dopant- an electrically active element selectively introduced into a semiconductor lattice.

effective diffusivity- measured diffusivity of an imperfect crystal (i.e. including effects from impurities, dislocations, point defects).

ellipsometry- optical analysis technique which uses polarized light to measure the thickness of thin dielectric films.

emissivity- the measure of the amount of thermal radiation emitted from a body (semiconductor wafer) .

epitaxy- a technique to grow a thin crystalline layer on a crystalline substrate so that the layer bears a certain crystallographic relationship to the underlying substrate.

epitaxial layer- a thin crystalline layer on a crystalline substrate that bears a certain crystallographic relationship to the underlying substrate.

Fermi level- a reference energy for the probability of occupation of a set of energy levels in a crystal.

FLOOPS- FLorida Object Oriented Process Simulator; a software program based on continuum and atomic diffusion theory which predicts the diffusion behavior of dopant in semiconductors.

graded- a gradual compositional transition within a semiconductor layer.

HBT- Heterojunction Bipolar Transistor; a semiconductor transistor consisting of two p-n junctions in series where the emitter and base are made of two semiconductors with different energy gaps.

heterojunction- the boundary between two layers of distinct semiconductor materials.

heterostructures- semiconductor structures consisting of more than one type of semiconductor material.

incoherent- epitaxial layer thickness greater than critical thickness.

interface- the boundary between two semiconductor layers.

intrinsic- undoped.

isomorphous- a crystalline compound phase that is capable of forming a complete series of solid solutions across the entire composition range.

lattice constant/parameter- the length of a crystallographic axis of a unit cell.

lattice mismatch- a heterostructure with semiconductor materials which have different lattice parameters.

metastable- semiconductor crystal condition between equilibrium theory and experimental measurement which depends on growth conditions and material parameters.

misfit dislocation- an extra plane of atoms inserted between existing lattice planes.

mobility- ease of movement of the carrier by the applied electric field.

MODFET- Modulation Doped Field Effect Transistor; a semiconductor transistor composed of source, channel and drain regions.

monochromator- an instrument which selects and transmits a narrow band of wavelengths from a source of radiation.

monolayer- one atomic layer.

monovacancy- an vacancy unassociated with another vacancy or dopant atom.

periodicity- the repeat distance of the alternating layers in a superlattice.

photodetector- a semiconductor device that absorbs photons to generate electronic carriers.

photonics- a division of semiconductor device physics in which energies from photons and electrons are exchanged.

point defect- a deviation in the periodicity of a lattice arising from a single point. Examples are an interstitial, vacancy and substitutional.

pseudomorphic- when the thickness of a lattice-mismatched epitaxial layer which is below critical thickness.

pyrometer- instrument which deduces a wafer's temperature from the intensity of the thermal radiation it emits.

quantum well- a potential energy well created by junctions in conduction and valence bands in which carriers are confined.

RBS- Rutherford Backscattering Spectrometry; an analytical technique based on backscattering of ions or projectiles incident on a semiconductor sample.

satellite peaks- peaks which occur in x-ray diffraction as a result of the periodicity of superlattice layers.

SIMS- Secondary Ion Mass Spectrometry; an analytical technique which uses accelerated ions to produce depth versus concentration profiles of semiconductor elements.

substrate- the original semiconductor material on which epitaxial layers are grown or deposited.

superlattice- a series of alternating epitaxial layers of two mismatched materials, each layer having a thickness below the critical thickness.

TEM- Transmission Electron Microscopy; an analytical technique in which electrons are accelerated and focused through a lens onto a sample such that transmitted electrons form either a diffraction pattern or a magnified image.

threading dislocation- a line dislocation which traverses from the substrate through the epitaxial layers to the surface.

trap- an energy level introduced through imperfections in a lattice which impede normal motion of carriers.

valence band- a band of allowed energy levels corresponding to unbonded holes free to travel throughout the crystal.

LIST OF REFERENCES

- Bar84 Barbuscia, D., Inter. Electron. Dev. Meeting 84, 757 (1984).
- Bar90 Baribeau, J.M., Pascual, R., & Saimoto, S., Appl. Phys. Lett. **57**, 1502 (1990).
- Bar78 Bartels, W.J., & Nijman, W., J. Crystal Growth **44**, 518 (1978).
- Bau96 Bauer, G., & Richter, W., eds., Optical Characterization of Epitaxial Semiconductor Layers, (Springer-Verlag, Berlin, 1996).
- Bea85 Bean, J.C., Fiory, A.T., Hull, R. & Lynch, T.R., Proc. of the 1st Inter. Symp. on Si MBE 85-7, 385 (1985).
- Ben87 Benninghoven, A., Rudenauer, F.G., & Werner H.W., Secondary Ion Mass Spectrometry: Basic Concepts, Instrumental Aspects, Applications, and Trends, (J. Wiley and Sons, New York, 1987).
- Blo93 Blöchl, P.E., Smargiassi, E., Car, R., Laks, D.B., Andreoni, W., & Pantelides, S.T., Phys. Rev. Lett. **70**, 2435 (1993).
- Bor88 Borg, R.J., & Dienes, G.J., An Introduction to Solid State Diffusion, (Academic Press, San Diego, 1988).
- Bou86 Bouchetout, A.L., Tabet, N., & Monty, C., Mat. Sci. Forum **10-12**, 127 (1986).
- Bou96 Boucaud, P., Wu, L., Guedj, C., Julien, F.H., Sajnes, I., Campidelli, Y., & Garchery, L., J. Appl. Phys. **80**, 1414 (1996).
- Cra75 Crank, J., The Mathematics of Diffusion, (Oxford University Press, Oxford, England, 1975).
- Cow96 Cownern, N.E.B., Kersten, W.J., de Kruif, R.C.M., van Berkum, J.G.M., de Boer, W.B., Gravesteijn, D.J., & Bulle-Liewma, C.W.T., Proc. of the Electrochem. Soc. **96-4**, 195 (1996).
- Cul78 Cullity, B.D., Elements of X-ray Diffraction, (Addison-Wesley, Reading, MA, 1978).

- Dea65 Deal, B.E., & Grove, A.S., J. Appl. Phys. **36**, 3770 (1965).
- deB97 de Berranger, E., Bodnar, S., Chantre, A., Kirtsch, J., Monroy, A., Granier A., Laurens, M., Regolini, J.L., & Mouis, M., Thin Solid Films **294**, 250 (1997).
- Del97 Deleu, J., Brijs, B., & Vandervorst, W., Proc. of the 11th Inter. Conf. on Secondary Ion Mass Spectrometry (SIMS XI) **11**, 359 (1997).
- Dor84 Dorner, P., Gust, W., Predel, B., & Roll, U., Phil. Mag. A **49**, 557 (1984).
- Dun86 Dunham, S.T., & Plummer, J.D., J. Appl. Phys. **59**, 2551 (1986).
- Eng97 Engel, C., Baumgartner, P., Holzmann, M., Nützel, J.F., & Abstreiter, G., Thin Solid Films **294**, 347 (1997).
- Fah89a Fahey, P.M., Griffin P.B., & Plummer, J.D., Rev. Mod. Phys. **61**, 289 (1989).
- Fah89b Fahey, P., Iyer, S.S., & Scilla, G.J., Appl. Phys. Lett. **54**, 843 (1989).
- Fai75a Fair, R.B. & Pappas, P.N., J. Electrochem. Soc. **122**, 1241 (1975).
- Fai75b Fair, R.B. & Tsai, J.C.C., J. Electrochem. Soc. **122**, 1689 (1975).
- Fai77 Fair, R.B. & Tsai, J.C.C., J. Electrochem. Soc. **124**, 1107 (1977).
- Fan96 Fang, W.T.C., Ph.D. Thesis, Stanford University, 1996.
- Fra91 Frank, W., Defect and Diffusion Forum **75**, 121 (1991).
- Fuj92 Fujita, K., Fukatsu, S., Shiraki, Y., Yaguchi, H., & Ito, R., Appl. Phys. Lett. **61**, 210 (1992).
- Gha95 Ghani, T., Hoyt, J.L., McCarthy, A.M., & Gibbons, J.F., J. Electronic Mater. **24**, 999 (1995).
- Gil95 Gilmer, G.H., Diaz de la Rubia, T., Stock, D.M., & Jaraiz, M., Nucl. Instr. and Meth. in Phys. Res. B **102**, 247 (1995).
- Gon94 Gonon, N., Gagnaire, A., Barbier, D. & Glachant, A., J. Appl. Phys. **76**, 5242 (1994).

- Gos93 Gossman, H.-J., Vredenberg, A.M., Rafferty, C.S., Luftman, H.S., Unterwald, F.C., Jacobson, D.C., Boone, T., & Poate, J.M., J. Appl. Phys. **74**, 3150 (1993).
- Gru97 Gruhle, A., & Schuppen, A., Thin Solid Films **294**, 246 (1997).
- Had95 Haddara, Y.M., Lee, C.C., Hu, J.C., Deal, M.D., & Bravman, J.C., Materials Research Soc. Bulletin **20**, 41 (1995).
- Han93 Hansen, S.E., & Deal, M.D., SUPREM IV.GS User's Manual, (Stanford University, Stanford, CA, 1993).
- Hay82 Hayafuji, Y., & Kajiwarara, K., J. Electrochem Soc. **129**, 2102 (1982).
- Het79 Hettich, G., Mehrer, H., & Maier, K., Defects and Radiation Effects in Semiconductors 1978 **46**, 500 (1979).
- Heu96 Heuting, R., Slotboom, J., Pruijmboom, A., de Boer, W., Timmering, C., & Cowern, N.E.B., IEEE Trans. on Electron Dev. **43**, 1518 (1996).
- Hol89 Hollander, B., Mantl, S., Stritzker, B., Jorke, H., & Kasper, E., J. Mater. Res. **4**, 163 (1989).
- Hol92 Hollander, B., Butz, R., & Mantl, S., Phys. Rev. B **46**, 6975 (1992).
- Hou91 Houghton, D., J. Appl. Phys. **70**, 2140 (1991).
- Hoy88 Hoyt, J. L., Williams, K.E., & Gibbons, J.F., U.S. Patent No. 4 787 551 (1988).
- Hu74 Hu, S.M., J. Appl. Phys. **45**, 1567 (1974).
- Hu92 Hu, S.M., J. Electrochem. Soc. **139**, 2066 (1992).
- Hu94 Hu, S.M., Mater. Sci. and Eng. R **R13**, 105 (1994).
- Iye89 Iyer, S.S. & LeGoues, F.K., J. Appl. Phys. **65**, 4693 (1989).
- Jai94 Jain, S.C., Germanium-Silicon Strained Layers and Heterostructures, (Academic Press, New York, 1994).
- Jai93 Jain, U., Jain, S.C., Nijs, J., Willis, J.R., Bullough, R., Mertens, R., & Van Overstraeten, R., Solid-State Electron. **36**, 331 (1993).

- Kas95 Kasper, E., Ed., Properties of Strained and Relaxed Silicon Germanium, (INSPEC, London, 1995).
- Kho90 Khoo, G.S. & Ong, C.K., J. Phys. Chem. Solids **51**, 1177 (1990).
- Kri95 Krishanmoorthy, V., PhD Thesis, University of Florida, 1995.
- Kru97 Kruger, D., Iltgen, K., Heinemann, B., Kurps, R., & Benninghoven, A., Proc. of the 4th Inter. Workshop on Measurement, Characterization and Modeling of Ultra-shallow Doping Profiles in Semiconductors **4**, 9.1 (1997).
- Kuo95 Kuo, P., Hoyt, J.L., Gibbons, J.F., Turner, J.E., & Lefforge, D., Appl. Phys. Lett. **67**, 706 (1995).
- Kuz98 Kuznetsov, A. Y., Cardenas, J., Svensson, B.G., Nylandsted Larsen, A., & Lundsgaard Hansen, J., Materials Research Society Proceedings, 1998.
- Lan85 Lang, D.V., People, R., Bean, J.C., & Sargent, A.M., Appl. Phys. Lett. **47**, 1333 (1985).
- Law96 Law, M.E., FLOOPS User's Manual, (University of Florida, Gainesville, FL, 1996).
- Lui96 Lui, X., Huang, D., Jiang, Z., & Wang, X., Phys. Rev. B **53**, 4699 (1996).
- May90 Mayer, J.W. & Lau, S.S., Electronic Materials Science: For Integrated Circuits in Si and GaAs, (Macmillan, New York, 1990).
- McV74 McVay, G.L. & DuCharme, A.R., Phys. Rev. B **9**, 627 (1974).
- Mit96 Mitha, S., Aziz, M.J., Schiferl, D., & Poker, D.B., Appl. Phys. Lett. **69**, 922 (1996).
- Mog96 Mogi, Y., Ph.D. Thesis, Cornell University, 1996.
- Mos85a Moslehi, M.M., & Saraswat, K.C., IEEE Trans. Electron Devices **ED-32**, 106 (1985).
- Mos85b Moslehi, M.M., Shatas, S.C., & Saraswat, K.C., Appl. Phys. Lett. **47**, 1353 (1985).
- Mur79 Murarka, S.P., Chang, C.C., & Adams, A.C., J. Electrochem. Soc. **126**, 996 (1979).

- New97 Newey, J.P., Robbins, D.J., & Wallis, D., Proc. of the 11th Inter. Conf. on Secondary Ion Mass Spectrometry (SIMS XI) 11, 979 (1997).
- Nyl97 Nylandsted Larsen, A., & Kringhoj, P., Physica Scripta T69, 92 (1997).
- Osa95 Osada, K., Zaitzu, Y., Matsumoto, S., Yoshida, M., Arai, E. & Abe, T., J. Electrochem. Soc. **142**, 202 (1995).
- Oda97 Oda, K., Ohue, E., Tanabe, M., Shimamoto, H., Onae, T., & Washio, K., Proc. of the IEEE Hong Kong Electron Devices Meeting 14, 791 (1997).
- Pac90 Packan, P.A. & Plummer, J.D., J. Appl. Phys. **68**, 4327 (1990).
- Pac91 Packan, P., Ph.D. Thesis, Stanford University, 1991.
- Pai95 Paine, A.D.N., Marooka, M., Willoughby, A.F.W., Bonar, J.M., Phillips, P., Dowsett, M.G., & Cooke, G., Materials Science Forum 196-201, 345 (1995).
- Pel91 Pellegrino, J., Qadri, S., Tseng, W., & Comas, J., Thin Solid Films 206, 40 (1991).
- Peo86 People, R., IEEE J. of Quantum Electronics QE-22, 1696 (1986).
- Pet91 Peters, L., Semicond. Inter. **14**, 56 (1991).
- Pre95 Presting, H., Mater. Res. Soc. Proc. **379**, 417 (1995).
- Pro90 Prokes, S.M. & Wang, K.L., Appl. Phys. Lett. **56**, 2628 (1990).
- Pru97a Prudon, G., Gautier, B., Berthelemy, S., Dupuy, J.C., Dubois, C., Schmitt, J., Delmas, J., & Vallard, J.P., Proc. of the 11th Inter. Conf. on Secondary Ion Mass Spectrometry (SIMS XI) 11, 339 (1997).
- Pru97b Prudon, G., Gautier, B., Dupuy, J.C., Dubois, C., Bonneau, M., Delmas, J., Vallard, J.P., Bremond, G., & Brenier, R., Thin Solid Films 294, 54 (1997).
- Qas98 Qasaimeh, O., Bhattacharya, P., & Croke, E.T., IEEE Photonics Tech. Lett. **10**, 807 (1998).

- Ret98 Rettig, R., Marschner, T., Stolz, W., & Tapler, L., J. Applied Phys. **84**, 237 (1998).
- Roo Roozeboom, F., Rapid Thermal Processing Science and Technology **2**, 349 (1993).
- Run98 Runyan, W.R., & Shaffner, T.J., Semiconductor Measurements and Instrumentation, (McGraw-Hill, New York, 1998).
- Sch90 Schröder, D.K., Semiconductor Material and Device Characterization, (John Wiley & Sons, New York, 1990).
- See68 Seeger, A. & Chik, K.P., Phys. Stat. Sol. **29**, 455 (1968).
- She89 Shewmon, P., Diffusion in Solids, (Minerals, Metals and Materials Society, Warrendale, PA, 1989).
- Sin88 Singh, R., J. Appl. Phys. **63**, R59 (1988).
- Sto85 Stolwijk, N.A., Frank, W., Holzl, J., Pearton, S.J., & Haller, E.E., J. Appl. Phys. **57**, 5211 (1985).
- Sun94 Sunamura, H., Fukatsu, S., Usami, N., & Shiraki, Y., Jpn. J. Appl. Phys. **33**, 2344 (1994).
- Tan81 Tan, T.Y. & Gösele, U., Appl. Phys. Lett. **39**, 86 (1981).
- Tem88 Temkin, H., Bean, J.C., Antreasyan, A., & Leibenguth, R., Appl. Phys. Lett. **52**, 1089 (1988).
- Tim97 Timans, P.J., Solid State Tech. **40**, 63 (1997).
- Tuc74 Tuck, B., Introduction to Diffusion in Semiconductors, (Peter Peregrinus, Stevenage, England, 1974).
- Van90 Van Ijzendoorn, L.J., Van De Walle, G.F.A., Van Gorkum, A.A., Theunissen, A.M.L., Van de Heuvel, R.A., & Barrett, J.H., Nucl. Instr. and Meth. in Phys. Res. B **50**, 127 (1990).
- Wer85 Werner, M., Mehrer, H., & Hochheimer, H.D., Phys. Rev. B **32**, 3930 (1985).
- Wil96 Williams, D.B. & Carter, C.B., Transmission Electron Microscopy, (Plenum Press, New York, 1996).

- Zau94 Zaumseil, P., Jagdhold, U., & Kruger, D., J. Appl. Phys. **76**, 2191 (1994).
- Zhu95 Zhu, J., Yang, L.H., Mailhiet, C., Diaz de la Rubia, T., & Gilmer, G.H., Nucl. Instr. and Meth. B **102**, 29 (1995).
- Zhu97 Zhu, Y., Yang, Q., & Wang, Q., IEEE J. Quantum Electronics **33**, 761 (1997).

BIOGRAPHICAL SKETCH

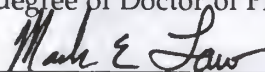
Michelle D. Griglione received her Bachelor of Science degree from Stanford University in 1991. She entered the Chemical Engineering doctoral program at the University of Florida in 1992. She spent her first two years working on the Robot Operated Materials Processing System (ROMPS) in collaboration with NASA/Goddard Space Flight Center, culminating in a shuttle flight experiment in September 1994. In 1996, she began her work in SiGe.

I certify that I have read this study and that in my opinion it conforms to acceptable standards of scholarly presentation and is fully adequate, in scope and quality, as a dissertation for the degree of Doctor of Philosophy.



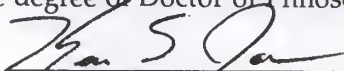
Timothy J. Anderson, Chairman
Professor of Chemical
Engineering

I certify that I have read this study and that in my opinion it conforms to acceptable standards of scholarly presentation and is fully adequate, in scope and quality, as a dissertation for the degree of Doctor of Philosophy.



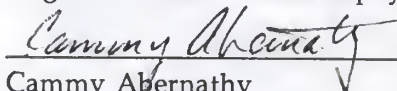
Mark E. Law
Professor of Electrical and
Computer Engineering

I certify that I have read this study and that in my opinion it conforms to acceptable standards of scholarly presentation and is fully adequate, in scope and quality, as a dissertation for the degree of Doctor of Philosophy.



Kevin S. Jones
Professor of Materials Science
and Engineering

I certify that I have read this study and that in my opinion it conforms to acceptable standards of scholarly presentation and is fully adequate, in scope and quality, as a dissertation for the degree of Doctor of Philosophy.



Cammy Abernathy
Professor of Materials Science
and Engineering

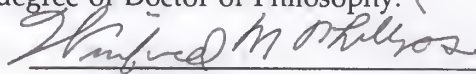
I certify that I have read this study and that in my opinion it conforms to acceptable standards of scholarly presentation and is fully adequate, in scope and quality, as a dissertation for the degree of Doctor of Philosophy.



Richard B. Dickinson
Assistant Professor of Chemical
Engineering

This dissertation was submitted to the Graduate Faculty of the College of Engineering and to the Graduate School and was accepted as partial fulfillment of the requirements for the degree of Doctor of Philosophy. \

May 1999

A handwritten signature in dark ink, appearing to read "Winfred M. Phillips", is written over a horizontal line.

Winfred M. Phillips
Dean, College of Engineering

M.J. Ohanian
Dean, Graduate School

LD
1780
1999
.G857

UNIVERSITY OF FLORIDA



3 1262 08554 4368